1-1-2010

Synthetic Levers Enabling Control Of Phase, Size And Morphology In Transition Metal Phosphide Nanoparticles (fe, Ni)

Elayaraja Muthuswamy
Wayne State University

Recommended Citation

SYNTHETIC LEVERS ENABLING CONTROL OF PHASE, SIZE, AND MORPHOLOGY IN TRANSITION METAL PHOSPHIDE NANOPARTICLES (FE, NI)

by

ELAYARAJA MUTHUSWAMY

DISSERTATION

Submitted to the Graduate School

of Wayne State University,

Detroit, Michigan

in partial fulfillment of the requirements

for the degree of

DOCTOR OF PHILOSOPHY

2011

MAJOR: CHEMISTRY

Approved by:

_____

Advisor   Date

_____

_____

_____

DEDICATION

To my dear friend Balaji Soundararajan

ACKNOWLEDGEMENTS

It has been a wonderful and pleasant experience working in the Brock laboratory and I have enjoyed every moment of this opportunity given to me by my advisor Prof. Stephanie L. Brock. For the tremendous support and good advice I have received in the past 5 years, I consider myself very fortunate to have carried out my dissertation work under her guidance. She has been extremely helpful to me ever since I applied to the graduate school at Wayne State University. She was patient with me during an unproductive first year and her caring advice and encouragement helped me gain confidence and achieve better outputs in the following years. I want to especially thank her for the training I received to improve my oral presentation and writing skills and also for the opportunities to present my work at various conferences. In addition, I would like to thank her for all the happy celebrations (birthday cakes and potlucks) in the lab. Words won't suffice to thank her enough and so in one word I would like to say "NANDRI" in my mother tongue (Thank you).

I would also like to sincerely thank the members of my dissertation committee Prof. Charles H. Winter, Prof. Andrew Feig and Prof. Gavin Lawes for their valuable time and suggestions. Their positive and critical comments during the exams have been extremely helpful to put this dissertation work in a better shape.

I was associated with Dr. Lawes's research group for studying the magnetic characteristics of nanoscale iron phosphides. I am very thankful to Prof. Gavin Lawes for his help during our collaborative work. He was always available for discussions and his inputs were extremely valuable. I would also like to thank him for writing me letters of

recommendation and sending them in a timely manner. Besides, I enjoyed collaborating with his group, as the members (Dr. Ambesh Dixit and Dr. Parashu Ram Kharel) were affable, approachable, and always ready to help me in whatever way possible.

In another collaborative project related to the use of mesoporous silica nanoparticles for drug delivery applications, I worked with Dr. David Oupicky's research group from the pharmacy school (WSU). I would like to acknowledge Dr. Oupicky for his thoughtful suggestions, assistance and for his letters of support. Working on a bio-application related project helped me learn and expand my repertoire in nanoparticle synthesis and characterization. Thanks a lot to Dr. Shantaraj Bhattarai and Amit Wani for all their valuable inputs and discussions.

I am also very grateful to Dr. Yi Liu, who was our manager of the electron microscopy facility. He was a very kind, patient and knowledgeable person and was always willing to help. I would also like to thank him for giving me the responsibility to take care of the lab during his absence, which also helped me to learn about maintenance of the microscopes. Also, thanks to Dr. Mei Zhi (Mike) our new manager for his help during the last six months.

Thanks to Dr. Mary Jane Heeg for her assistance with the powder X-ray diffraction (PXRD) measurements. This dissertation mostly comprises of the data collected from the PXRD facility and without her assistance it would not have been possible for me to complete this work in time.

The staff at science stores was of great support in acquiring chemicals and other supplies related to this dissertation research. They are a group of nice, friendly and

iv

helpful people and I would like to thank all of them including Liz, Greg, Bonnie, Jason, Joe and Lorraine for their service.

The office and technical staff in Chemistry Department have all been kind and very helpful at various times during the last 5 years. Thanks to Sharon Kelly, Melissa Barton, Mary Wood, Diane Klimas, Erin Bachert, Debbie McCreless and Bernie Meisik. Thank you Nestor for your time and tech support. Dave Daenzer from CIF also provided timely help with repairs for glass equipments.

My heart felt thanks to Dr. Palaniappan Arumugam who took care of me during the first semester and for constantly directing me in the right path. Dr. Kristy Gregg was my mentor in the lab. I am grateful for the training I received from her and I find that her teachings are extremely helpful till this date. Thanks to Dr. Kennedy Kalebaila for providing me valuable tips in the lab and also assisting with literature seminar preparation. I would also like to appreciate Dr. Keerthisinghe Senevirathne for the friendly discussions and for sharing his experience with the phosphide nanoparticle synthesis. I thoroughly enjoyed the interactions with Dr. Hongtao Yu and Valentina Ganzha-Hazen. I want to thank Dr. Indika Arachchige for his help during the job search and also for being an inspiration. I spent a lot of time with Dr. Qinghong Yao during course work, teaching and in the lab. She is a kind person and was very helpful to me all through the graduate study.

Irina Pala has been a good friend of mine during the last three years. She has always been there for me and helped me in a number of ways. I also had a great time with all of the current group members: Shreyashi Ganguly, Layan Savithra, Yanhua Zhang, Lasantha Perera, Asha Bandara and John Randolph. I enjoyed working together with

v

Michal Brichacek and Antonio Castañeda. Thank you very much to all of you for being great lab mates and I will miss the conversations during the coffee breaks at our own StarBROCKs coffee club and the fun filled parties. I wish all the current group members the very best in their research. Thanks also to members of the Verani group and the Crich group for all their help.

Besides, it is a pleasure to take this opportunity to thank my friends at Wayne State University: Venkat, Chandru, Ravi, Tickoo, Aman, Roger, Chinesh, Vivek, Wilson, Mike, Frank, Radek, Ajith, Satish, Venkatesh, Selvakumar, Dajena, Sanuja, Fatima, Saritha Selvakumar, Deeptha Venkat and all other members from the Chemistry Cricket Club. The cricket matches were played with great intensity and it helped to stay fresh and active in the lab.

I am grateful to Dr. H. N. Vasan and Prof. S. Umapathy at IISc (Bangalore, India), for motivating me to do Ph.D.

I would like to thank my parents for all their sacrifices to provide me a good education. I have been staying away from them since 1991 but their constant encouragements through letters and phone calls have given me the strength. Lastly and most importantly, I want to thank Rama Shanmugam for her love and affection, emotional support and for encouraging me to do my best. I also wish to thank her parents and sister for their support.

TABLE OF CONTENTS

LIST OF TABLES

LIST OF FIGURES

xi

LIST OF SCHEMES

CHAPTER 1

INTRODUCTION

Materials with one of their dimensions in the range 1-100 nm are commonly referred to as nanomaterials and exhibit properties intermediate to those of bulk solids and atomic/molecular systems. Nanoparticles are of interest because their properties are often entirely different and sometimes superior to those of their bulk counterparts, and they vary with changes in size, shape and morphology. Their unique behavior has resulted in a new branch of multidisciplinary science, nanoscience and nanotechnology, to come into existence. Although research efforts related to nanoscience and nanotechnology have seen an enormous growth in the last two decades, the art of making nanoparticles has been known to human civilizations as early as the 4th century.[1] It should also be noted that the first nanoparticles synthesized in a chemical laboratory date back to 1857 when Sir Michael Faraday prepared ruby colored gold nanoparticles.[2]

The synthesis of nanomaterials is a key step in uncovering the size and shape dependant properties of nanomaterials and their use for technological advancement. Thus, it is essential to develop synthetic methods that can result in better control of the physical attributes of nanomaterials. Over the past decade, the Brock laboratory has been a pioneer in the preparation and study of the properties of nanoscale transition metal pnictide nanoparticles that are relevant for catalytic and magnetic applications.[3-4]

This dissertation research is focused on the development of a synthetic strategy to control phase in the iron phosphide system, thus resulting in the preparation of phase-pure nanoparticle samples of FeP and Fe_2P. This approach was also extended to the

nickel phosphide system, and as a consequence, formation of phase pure Ni_2P and $Ni_{12}P_5$ nanoparticles has been achieved.

In addition, reaction conditions were used as synthetic levers to obtain the two different Ni-P phases in various sizes and different morphologies (hollow *vs.* solid), and the ability to topotactically convert $Ni_{12}P_5$ to Ni_2P was demonstrated. Finally, the reactivity of oxide nanoparticles is demonstrated by carrying out transformation reactions to phosphides and sulfides and the results clearly indicate that oxidation of metal nanoparticles should not be a concern for reactivity.

1.1 Nanoparticles

The physical and chemical properties of nanoparticles can be attributed in part to the structural changes that take place at the atomic level upon reduction in size to the nano regime, specifically the increased ratio of atoms present on the surface to the total number of atoms. The increased surface to volume ratio can lead to enhanced catalytic properties due to exposure of more active sites.[5]

The electronic structure of nanoparticles is also expected to be different from a bulk solid. The broad energy bands present in bulk solids are broken down into discrete energy levels upon size reduction, as the infinite crystal size assumption is no longer valid.[6] The generic band energy diagram of a main group semiconducting nanoparticle is shown in Figure 1.1. The energy gap between the highest occupied molecular orbital (HOMO) and the lowest unoccupied molecular orbital (LUMO) is tunable in the nanoscale size regime, thus resulting in size-dependant emission properties for semiconductor nanoparticles (quantum dots).[7] The light emitting properties arising from

quantum dots can be employed for applications related to photovoltaics,[8-9] biological labeling[10] and sensing.[7, 11]

In general, the size of nanoparticles is also comparable to the length scales that govern various physical phenomena.[12] Thus, when light in the UV-vis-near IR region impinges on an interface between a non-magnetic metal and a dielectric, a collective oscillation of conduction electrons results. This phenomenon is called surface plasmon resonance (SPR) and the emission properties of noble metal nanoparticles are determined by localized SPR.[13] These properties are being exploited for use in analytical devices and for applications related to diagnosis and therapeutics.[14]

For ferromagnetic materials, when the size of a nanoparticle is reduced to less than that of a magnetic domain, superparamagnetic properties set in (see section 1.3).[15] In addition, the magnetic coercivity (the energy needed to flip spins to their opposite direction) is tunable with respect to size and shape. The derived magnetic properties can be potentially used in the development of devices for high density data-storage,[16] site-specific drug release,[17-18] magnetic refrigeration,[19] and contrast agents for MRI.[20]
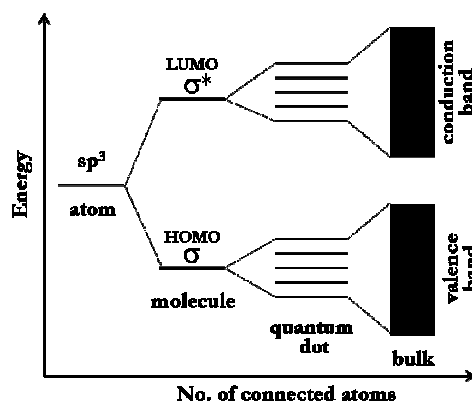
Figure 1.1. Description of the electronic energy levels for systems composed of varying numbers of atoms (adapted from Schmid).[6]

Thus, the reduction in size of matter to the nanoscale provides an opportunity to tailor properties appropriate to the needs of specific applications. These novel properties associated with nanomaterials have resulted in the devotion of considerable funds and personnel to nanoscience for development of new technologies.

1.2 Solution-Phase Synthesis of Nanoparticles

A variety of solution based chemical methods such as solvothermal synthesis, sonochemical synthesis, microwave synthesis, micellar synthesis and synthesis using coordinating solvents has been utilized for the preparation of nanoparticles. The efficiency of a synthetic method for a particular preparation can be gauged by the quality of the nanoparticles produced in terms of phase-purity and control over the physical attributes such as size, shape and morphology. This dissertation research involved the decomposition of organometallic reagents in mixtures of high boiling solvents/coordinating ligands and subsequent reaction of the generated metallic species with phosphines to generate phosphides of transition metals.

The use of coordinating ligands is a powerful means to control the growth of nanocrystals. Coordinating groups are normally bulky ligands or consist of long alkyl chains with the binding group at one end. The binding of the ligands to the metal atoms on the surface of nanoparticles is similar to the binding of ligands in coordination chemistry.[21] Alkyl amines, alkyl phosphines and alkyl phosphine oxides are some of the commonly used coordinating ligands. They bind to growing nuclei of the nanoparticles in a dynamic fashion, thereby resulting in a decrease of the growth kinetics. Additionally, the binding strengths of specific ligands vary with different facets of a nanocrystal. This difference in binding strengths has been utilized to promote the formation of 1-D

nanostructures, because the nanocrystal growth along certain crystal faces is inhibited due to tighter binding of ligands.[22] In general, because of steric stabilization, ligands with shorter alkyl chain lengths promote formation of larger nanoparticles, and vice versa.[23-24]

One of the most successful nanoparticle preparation methods in terms of quality and monodispersity achieved is the decomposition of organometallic precursors in hot coordinating solvents (120-360 °C).[21] Controlling nucleation and growth, the two most important steps in the formation of nanocrystals, is the key to achieve a tight size distribution. The formation of highly monodisperse nanocrystals can be explained by La Mer's model of nucleation and growth, as shown in Figure 1.2.[21, 25] Injection of precursors into a hot solvent system results in immediate decomposition of precursors resulting in the supersaturation of monomers, which then leads to nucleation. The supersaturation is partially relieved in the nucleation step, which is then followed by a rapid growth of the nuclei through the addition of the rest of the solution-phase monomers. New nuclei do not form when the concentration of monomers falls below the threshold limit. When the monomer concentrations are sufficiently depleted, the growth of nanoparticles proceeds by a phenomenon called Ostwald ripening, wherein smaller nanoparticles (with higher surface energy) dissolve in solution and result in further growth of the larger nanoparticles. In an alternate method, supersaturation and nucleation can also be triggered by slow heating of precursors to the reaction temperature. Once supersaturation is relieved by a nucleation burst, the temperature can be brought down to avoid further nucleation, leading to addition of monomers to already formed nuclei.[21, 25] In general, the size and size distribution are also affected by the growth temperature and reaction time. Higher growth temperatures favor the formation of larger nanoparticles as

the rate of addition of monomers to existing particles is enhanced. Likewise, Ostwald ripening occurs more readily at higher temperatures and also at long reaction times (i.e. after the monomers is consumed) leading to larger particle size.
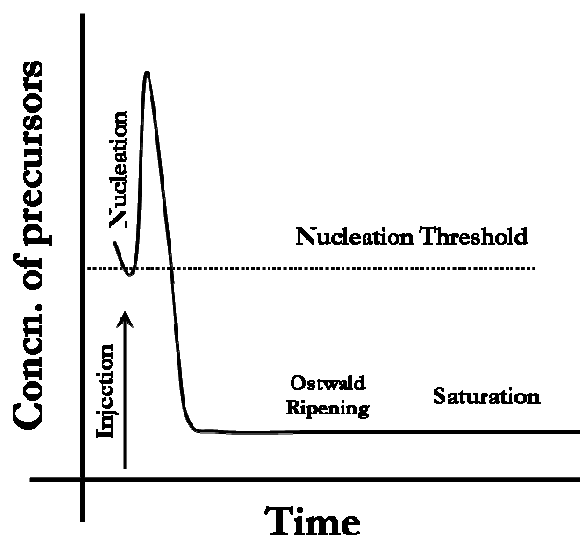
Figure 1.2. Scheme illustrating La Mer's model for the stages of nucleation and growth for monodisperse colloidal nanocrystals (adapted from Klimov).[26]

The strategies discussed here do not always result in the formation of monodisperse nanoparticles, as the growth of the nanocrystal depends on the material involved and the reactivity of the monomeric species. When polydisperse samples are produced, size-selective precipitation methods can be employed to reduce the polydispersity of the sample. Size-selective precipitation involves the addition of an anti-solvent in small quantities in order to precipitate out the larger particles, a phenomenon driven by their stronger Van der Waals interactions.[27] This is then followed by subsequent addition of anti-solvent to precipitate out consecutively smaller fractions.

1.3 Magnetism

Magnetism is exhibited by all materials and their magnetic behavior is dependent on the orientation of their magnetic moments. If unpaired electrons are present, the electron spins can orient themselves in several ways, resulting in different kinds of magnetism, as depicted in Figure 1.3. The traditional classification of materials is based on their response (magnetic susceptibility) to an external magnetic field. Magnetic susceptibility (χ) is defined as the ratio between magnetization (M) and the applied field (H).
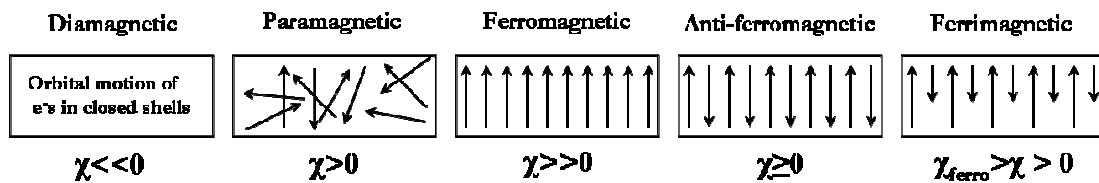
Figure 1.3. Illustration of magnetic moment alignment in different types of magnetism.

1.3.1 Diamagnetism

Materials that consist only of paired electrons are classified as diamagnetic. The susceptibility values for diamagnetic materials are very small and negative ($\chi \sim -10^{-5}$) as their magnetic response weakly opposes the external magnetic field.[28] Diamagnetism is not affected by temperature and common examples of diamagnets include mercury, diamond and superconductors. A typical response of a diamagnetic material to the application of an external magnetic field is given in Figure 1.4. The response is linear, reversible and has a negative slope. All materials with paired electrons exhibit

diamagnetic behavior, but the magnetic effects arising from the presence of unpaired electrons will eclipse the diamagnetic effects.
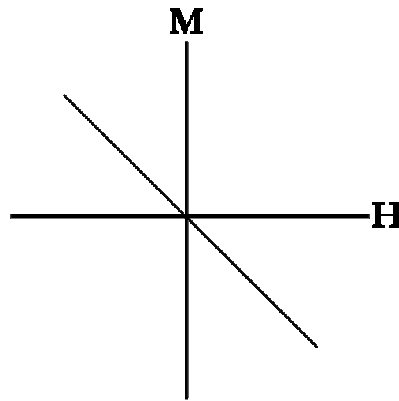
Figure 1.4. Typical magnetization *vs.* applied field curve for a diamagnetic material.

1.3.2 Paramagnetism

When magnetic moments are oriented randomly they give rise to paramagnetism. Upon the application of an external magnetic field, the moments align parallel with the field direction. The susceptibility for paramagnets is small and positive and typically ranges from 10^{-3} – 10^{-5}.[28] Common examples include platinum, aluminum and manganese. A typical magnetization *vs.* applied field curve for paramagnets is given in Figure 1.5 and shows that the magnetization increases linearly with increasing applied field. Paramagnetism is affected by changes in temperature and the temperature dependence of their susceptibility can be explained by the Curie law given in Equation 1.1, where C is the Curie constant. The plot of inverse susceptibility against temperature gives a straight line passing through the origin with a positive slope. This linear response is indicative of the fact that the individual moments respond independently to an applied external magnetic field.

$$\chi = \left(\frac{C}{T}\right)$$
Equation 1.1
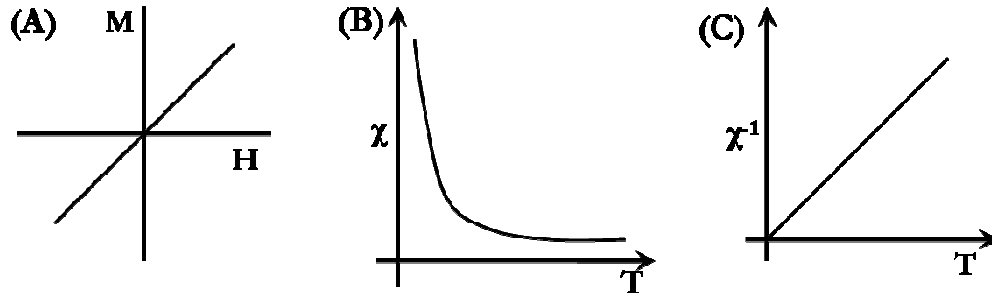
Figure 1.5. Graphs illustrating typical behavior of paramagnetic materials. (A) Magnetization *vs.* applied field (B) Magnetic susceptibility *vs.* temperature and (C) Inverse susceptibility *vs.* temperature.

1.3.3 Antiferromagnetism

Antiferromagnetism arises when neighboring magnetic moments that are equal in magnitude align opposite to each other resulting in cancellation of magnetic moments. Despite apparent cancellation, a very small value for susceptibility is observed with these materials, usually on the order of $0\text{-}10^{-2}$. Like paramagnetic materials, the magnetization of antiferromagnetic materials varies linearly with increasing applied field and their susceptibility is temperature dependent. Typical graphs depicting anti-ferromagnetic behavior are given in Figure 1.6. Common antiferromagnets include chromium, nickel (II) oxide and iron manganese (FeMn) alloy. The temperature above which antiferromagnets behave similarly to paramagnets is called the Nèel temperature (T_N). Because the Curie law does not take into account magnetic moment interactions between atoms, the law was modified (Equation 1.2) to form the Curie-Weiss law, where C is the

Curie constant (material specific), T is temperature and T_θ is Weiss constant (x-intercept), which indicates the strength of the magnetic interactions. In a plot of inverse susceptibility *vs.* temperature (Figure 1.6.C) a negative sign for T_θ indicates antiferromagnetic interactions.

$$\chi = \left(\frac{C}{T \pm T_\theta} \right)$$

Equation 1.2
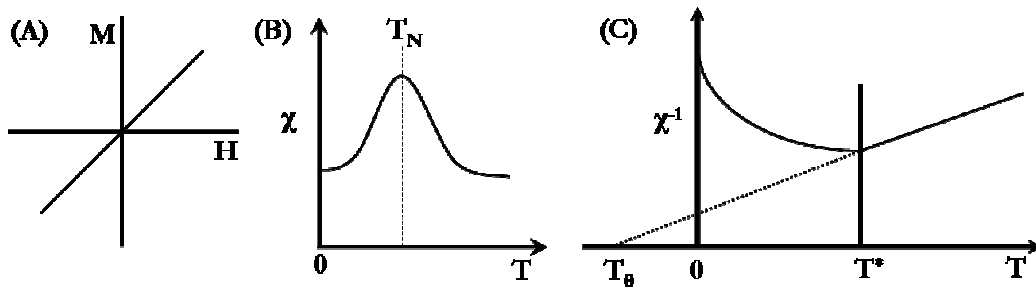
Figure 1.6. Graphs depicting typical behavior of an antiferromagnetic material. (A) Magnetization *vs.* applied field (B) Magnetic susceptibility *vs.* temperature and (C) Inverse magnetic susceptibility *vs.* temperature.

1.3.4 Ferromagnetism

Ferromagnetic materials are by far the most important class of magnetic materials as they are utilized in diverse practical applications such as in magnetic recording media, electromagnets, transformers and electromagnetic relays. Ferromagnetism results from parallel alignment of magnetic moments along the direction of the magnetic field. They are strongly attracted to magnets and have large positive susceptibilities ($\chi \gg 1$).[28] The magnetization is dependent on temperature and it behaves as a paramagnet above the

transition temperature, referred to as the as Curie temperature, denoted by T_c (Figure 1.7A). Above T_c, the parallel alignment of magnetic moments is disrupted and they orient randomly. In a plot of inverse susceptibility *vs*. temperature a positive sign for T_θ indicates ferromagnetic interactions (Figure 1.7B).

The magnetization *vs*. applied field experiment carried out below T_c results in a hysteresis curve which is typical of ferromagnets (Figure 1.7C). The term hysteresis was first introduced by Ewing and the suitability of ferromagnetic materials for applications is determined principally from characteristics shown by their hysteresis loops.[28] The initial magnetization curve generated when magnetization is measured as function of the applied field is called the virgin curve (VC). It steadily leads up to saturation magnetization, which is denoted by M_S. M_S is a characteristic property of a ferromagnetic material wherein all the moments are aligned with the direction of the field. When the field is steadily reduced to zero, a typical ferromagnet does not lose the magnetization completely and the residual magnetization is called the remnant magnetization (M_R). The M_R of the material can be reduced to zero by applying a field in the opposite direction, and the magnitude of the field required to do this is called the coercivity (H_C). When the field is further increased, saturation of magnetic moments in the opposite direction is achieved. The values for coercivity and saturation magnetization are also important for the choice of practical applications.[28] For example, materials chosen as electromagnets are expected to have low remanence and coercivity in order to ensure that they can be easily reduced to zero while materials chosen as permanent magnets are expected to possess high remanance and coercivity in order to retain the magnetization as much as possible. In general, coercivities are higher when ferromagnetic materials possess

anisotropy. The different kinds of anisotropies that can exist include shape anisotropy, magnetocrystalline anisotropy, stress anisotropy, exchange anisotropy and externally induced anisotropy.[15]
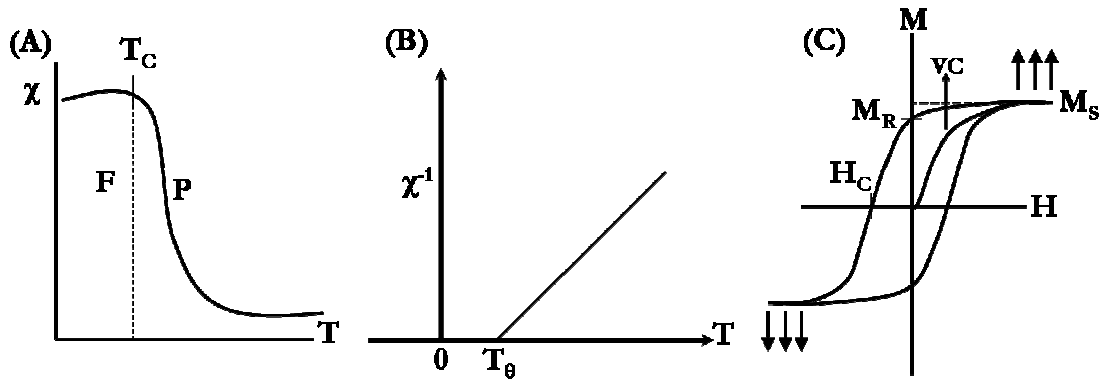
Figure 1.7. Typical response of a ferromagnet. (A) Magnetic susceptibility *vs.* temperature (B) Inverse susceptibility *vs.* temperature and (C) Magnetization *vs.* applied field resulting in a hysteresis plot.

Ferrimagnetism results in magnetic moment alignment similar to antiferromagnetism but the opposing moments are unequal in magnitude, thus giving rise to a net moment and behavior that is qualitatively similar to ferromagnets. This kind of magnetic moment ordering is observed in ionic oxides containing two opposing magnetic sub-lattices. A well known ferrimagnetic material is magnetite (Fe_3O_4), which exhibits all the hallmarks (hysteresis, Curie temperature, coercivity, remnant magnetization) of a typical ferromagnet but has a smaller moment.

1.4 Magnetic Behavior of Nanomaterials

When ferro or ferrimagnetic materials are prepared on the nanoscale, their size becomes comparable to the size of a magnetic domain and the mechanism by which the magnetic moments re-align in a magnetic field changes. A comparison of the mechanism of alignment of magnetic moments for bulk and nanoscale samples is given in Figure 1.8.
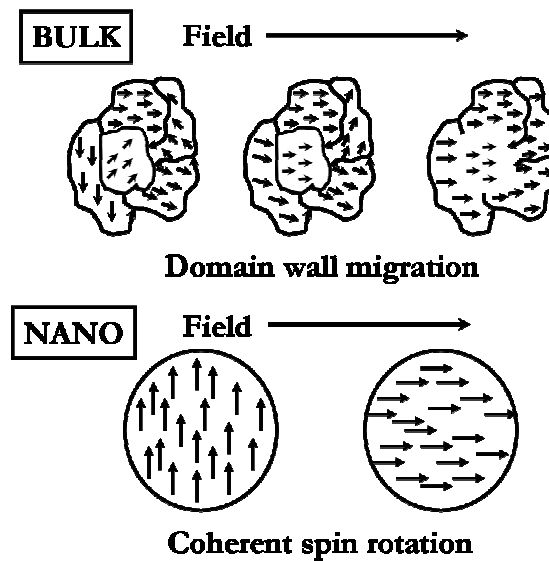
Figure 1.8. Comparison of the mechanism of magnetic moment alignment along the direction of the applied field for bulk and nanoscale ferro or ferrimagnetic samples.

In the case of bulk materials, magnetic domains are present in which all moments point along the same direction and act in cooperative manner. The domains are separated by domain walls that possess a characteristic width and energy associated with their formation. The reversal of magnetization occurs by the motion of these walls, which is called domain wall migration. In the case of nanoparticles, when the size falls below a

critical diameter, the formation of domain walls is not energetically favorable and thus each particle exists as a single domain. In this case, the reversal of magnetization occurs through the coherent rotation of all the moments in the domain, which requires higher energy and thus results in higher coercivity values for nanoparticles.[7, 15] However, with a further decrease in size, the magnetic moments can be affected by fluctuations in temperature, and at this point, the nanoparticles become superparamagnetic. In superparamagnetic nanoparticles, the moments respond easily to changes in magnetic field and hysteresis is no longer observed. Superparamagnetic nanoparticles still exhibit high saturation magnetization but do not exhibit remnant magnetization at zero external magnetic field.[15]
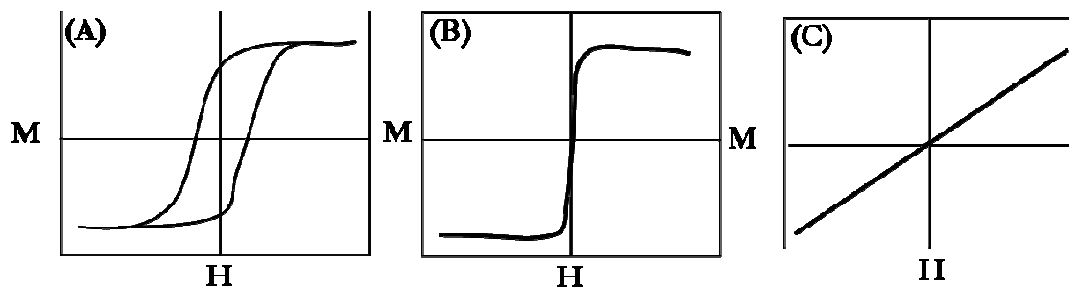
Figure 1.9. Comparison of the magnetization *vs.* applied field curves of (A) ferromagnetic (B) superparamagnetic and (C) paramagnetic materials.

Figure 1.9 compares the behavior of ferro (or ferri), superpara and paramagnetic materials in a magnetization *vs.* field experiment. The temperature above which the transition from ferromagnetic to superparamagnetic occurs is called the blocking temperature (T_b) and it is a function of the size of the nanoparticles and the timescale of the experiment.
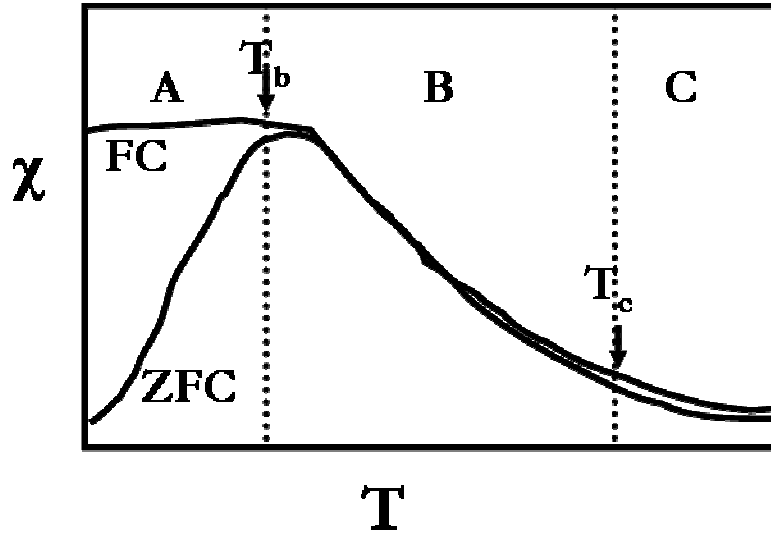
Figure 1.10. A typical ZFC/FC curve showing the blocking temperature (T_b) and Curie temperature (T_c). Region 'A' corresponds to the hysteretic region (Figure 1.9, plot A), region 'B' corresponds to the superparamagnetic region (Figure 1.9, plot B) and region 'C' to the regular paramagnetic region (Figure 1.9, plot C).

The T_b of superparamagnetic nanoparticles can be obtained by carrying out zero field cooled (ZFC) and field cooled (FC) magnetization *vs.* temperature experiments in a low field (on the order of 100 Oe) as shown in Figure 1.10. During the experiment, the sample is cooled down in the absence of a magnetic field. The moments are frozen at this point. The sample is then heated gradually in the presence of the low magnetic field. With increasing temperature, the moments start aligning towards the field as indicated by an increase in magnetization. The magnetization stops increasing at T_b, at which point the thermal energy is sufficient to cause the moments to orient randomly. Above T_b, the magnetization slowly drops down towards zero, indicating that the particles are in the superparamagnetic regime.[29] Above the T_c, the sample becomes a simple paramagnet. In

the field cooled protocol, the sample is now cooled in the presence of the low magnetic field. The magnetization increases until T_b and does not follow the path of the ZFC curve after T_b because the moments are frozen in their aligned state. T_b is usually determined from the peak of the ZFC curve.

1.5 Transition Metal Pnictides

As a class, transition metal pnictides have long been of interest for magnetic and catalytic applications.[30] They exist in a wide range of stoichiometries, and the properties depend sensitively on their physical and electronic structure. A selection of binary pnictides and their associated properties is given in Table 1.1.[30-35] These properties include ferromagnetism, catalytic activity, semiconductivity, superconductivity and thermoelectricity. In particular, the phosphides are receiving considerable interest for their hydrotreating catalytic properties in the processing of fuels. Indeed, Ni_2P is reported to be the most efficient hydrodesulfurization (HDS) catalyst, even outperforming the commercially used $Ni-Mo-S/Al_2O_3$ catalysts in terms of activity and resistance to poisoning.[31, 36-37] Despite a good understanding of the bulk properties of binary pnictides, little is known of their nanoscale properties, due in part to a lack of methodologies that enable size control on this scale. Hence, recent attention has turned to the synthesis of nanoscale forms of transition metal pnictides.

Qian and coworkers developed a solvothermal strategy to prepare a variety of transition metal pnictides on the nanoscale. Some of the reported phases include FeP,[38] Ni_2P,[39] Co_2P,[39] Cu_3P,[39] NiAs,[39] CoP,[40] CoAs,[41] FeAs,[42] and NiSb.[43] These reactions were carried out in a sealed vessel at pressures above atmospheric pressure and temperatures greater than the boiling point of the solvent. The syntheses typically resulted in

polydisperse samples and, in most cases, the properties have not been reported. Generally, the products formed as insoluble precipitates and the morphology of the samples was also not well controlled.

Table 1.1 Table indicating a selection of transition metal pnictides and their associated properties.[30-35]

Transition Metal Pnictide	Property
MnP	Ferromagnetic ($T_c = 292$ K)
MnAs	Ferromagnetic ($T_c = 315$ K)
MnSb	Ferromagnetic ($T_c = 587$ K)
MnBi	Ferromagnetic ($T_c = 628$ K) Magneto-optical Activity
Fe_3P	Ferromagnetic ($T_c = 716$K)
Fe_2P	Ferromagnetic ($T_c = 217$ K)
FeP	Anti-ferromagnetic ($T_N = 115$ K)
FeP_2	Semiconducting
Co_2P	Catalytic Activity
CoP	Catalytic Activity
CoP_3	Semiconducting
$CoSb_3$	Thermoelectric
$Ni_{12}P_5$	Catalytic Activity
Ni_2P	Catalytic Activity
NiP_2	Semiconducting
$NiSb_3$	Superconducting (4.06 K)
MoP	Catalytic Activity
Mo_3P	Superconducting (7.0 K)
Rh_2P	Catalytic Activity Superconducting (1.3 K)
RhP_2	Semiconducting
Pd_5P_2	Catalytic Activity
WP	Catalytic Activity
W_3P	Superconducting (2.26 K)

Lukehart and coworkers employed a range of molecular precursors containing phosphine ligands for the generation of transition metal pnictides in a silica xerogel matrix.[44-45] They prepared molecular precursors with both phosphine and alkoxysilyl functional groups, with the latter specifically designed for the complex to be introduced into a silica xerogel matrix using sol-gel chemistry. Thermal treatment of the as-prepared xerogels under reducing conditions resulted in the formation of pnictides. They were able to prepare a range of crystalline pnictides including Fe_2P, RuP, Co_2P, Rh_2P, Ni_2P, Pd_5P_2, and PtP_2 using this strategy. The pnictides were observed to be polydisperse nanoparticles, and in addition, they were trapped in the silica xerogel matrix making them unsuitable for further manipulations.

Our lab was one of the first to report the formation of dispersible transition metal pnictide nanoparticles with good control of polydisperisty.[46-47] For the synthesis of FeP nanoparticles, iron (III) acetylacetonate was treated with highly reactive tris-trimethylsilyl phosphine ($P(SiMe_3)_3$) at temperatures in the range 240-320 °C using tri-octylphosphine oxide (TOPO) as solvent and dodecylamine (DDA), myristic acid (MA) and hexylphosphonic acid (HPA) as coordinating ligands. The reactions resulted in phase-pure spherical nanoparticles of FeP with an average size of 4.65 ± 0.74 nm.[46] Magnetic susceptibility measurements indicated antiferromagnetic interactions in the as-prepared sample and a suppression of the low temperature metamagnetic behavior. This synthesis was then successfully extended to the preparation of MnP nanoparticles. Manganese carbonyl ($Mn_2(CO)_{10}$) was treated with $P(SiMe_3)_3$ at temperatures >220 °C to generate highly crystalline spherical nanoparticles of MnP.[47] TOP was also observed to

act as a P-source in this reaction, indicating that it is not necessary to use highly reactive and pyrophoric phosphines such as $P(SiMe_3)_3$. The nanoparticles prepared from TOP were highly crystalline and the synthesis was found to be successful for the generation of FeP and CoP as well, indicating its general applicability.[47]

The use of alkylphosphines in phosphide nanoparticle synthesis gained popularity and a lot of other research groups started utilizing them as safe, cost effective alternatives to silylated phosphines. Hyeon and coworkers reported the formation of Fe_2P nanorods by the reaction of iron pentacarbonyl ($Fe(CO)_5$) with TOP at 300 °C in a solvent surfactant system composed of octylether and oleylamine.[48] Injection of a Fe-TOP mixture into the hot solvent/surfactant system using a syringe pump ensured a steady and continuous supply of the precursors. The synthesis resulted in the formation of short Fe_2P nanorods with an average dimension of 3 nm x 12 nm. When the injection was carried out a second time after an interval of 30 minutes, the synthesis resulted in longer nanorods with an average dimension of 5 nm x 43 nm. They also observed that the dimension of the nanorods can be varied as a function of the injection rates, with slower injection rates favoring longer nanorods. The Fe_2P nanorods were observed to grow in [002] direction, attributed to its intrinsic hexagonal crystal structure. Unusual magnetic properties were observed for Fe_2P nanorods which exhibited T_b's higher than the reported T_c of 217 K.[49] This anomaly was attributed to the possible presence of ferromagnetic impurities such as Fe or Fe_3P, which are characterized by higher T_c's than Fe_2P.

In addition to Fe_2P, Hyeon and coworkers also developed a generalized synthesis method for the preparation of some other first row transition metal phosphide nanorods.[50] The synthetic strategy was similar to injection route described above except for small

changes in reaction conditions and the precursors. They reported nanorods of MnP (8 nm x 16 nm; 11 nm x 15 nm), Co_2P (2.5 nm x 20 nm), FeP (12 nm x 500 nm; 7 nm x 600 nm) and Ni_2P (4 nm x 9 nm).

The synthesis of the more P-rich phase FeP involved injection of the iron-phosphine complex into TOPO maintained at 360 °C.[50] FeP formation was originally attributed to the more P-rich environment generated by the presence of TOPO and the higher reaction temperature. However, the raise in temperature from 300 °C (Fe_2P nanorods)[48] to 360 °C (FeP nanorods)[50] must have been the sole factor as the possibility of TOPO playing the role of a phosphorus precursor was dismissed in later reports.[51] Magnetic susceptibility measurements revealed ferromagnetic properties for FeP, which are contradictory to its characteristic antiferromagnetic nature and our prior data on FeP nanoparticles.[46] Examination of the published PXRD pattern of FeP clearly revealed the presence of small amounts of Fe_2P, suggesting the ferromagnetism observed by Hyeon and coworkers is attributable to impurity.[50] Indeed, Liu and coworkers reported the formation of FeP nanorods and nanowires with a very similar synthetic strategy using a solvent system composed of TOPO and TOP in 1:1 weight ratio and the magnetic susceptibility measurements indicated antiferromagnetic interactions for FeP, consistent with expectation and our prior studies.[46, 52]

The MnP, Co_2P and Ni_2P nanorods prepared by Hyeon and coworkers used $Mn_2(CO)_{10}$, $Co(acac)_2$, and $Ni(acac)_2$ as precursors, respectively. Magnetic susceptibility measurements carried out on MnP nanorods indicated superparamagnetic properties with a blocking temperature of 265 K at 100 Oe, and coercivities of 5,000 Oe at 15 K. However, the introduction of shape anisotropy was not observed to introduce any

changes in the coercivity of the sample. Although, Co_2P and Ni_2P are expected to be Pauli paramagnetic in bulk form, the nanorods of Co_2P and Ni_2P prepared by Hyeon and coworkers exhibited Curie-Weiss behavior with strong magnetic interactions.[50] Overall, while some of the samples reported by Hyeon and coworkers were revealed to be impure, the introduction of precursors via syringe pump to produce nanorods with better reproducibility was novel and its applicability to a variety of metals was promising.

Schaak and coworkers have also reported a general methodology for the preparation of a variety of metal phosphide nanoparticles.[53-54] The Schaak method involves the preparation of metal nanoparticles and their subsequent reaction with TOP to generate the corresponding metal phosphide nanoparticles with hollow morphologies. In addition to metal nanoparticles, they also reported the conversion of bulk powders, foils, wires and thin films into corresponding phosphides, indicating the versatility of TOP as phosphorus precursor.[53] Around the same time, Chiang and coworkers reported the formation of Ni_2P nanoparticles via metal nanoparticle conversion with TOP and also observed hollow morphologies.[55] The void structures are attributed to the nanoscale Kirkendall effect, in which differences in diffusion rates between the metal atoms (outward, fast) and the phosphorus atoms (inward, slow) during the phosphidation results in depletion of matter in the particle interior.[56] A series of papers have been subsequently published by various research groups on the synthesis of hollow nanostructures of metal phosphides, which might be interesting for applications related to catalysis due to their high surface area.[51, 57] In particular, the work on nickel phosphides by Tracy and coworkers demonstrated that control of morphology between hollow and solid nanostructures can be achieved by controlling the P:Ni precursor ratio. However all the

samples reported by Tracy and coworkers were characterized to be mixtures of Ni_2P and $Ni_{12}P_5$ (i.e., not phase-pure).[51]

It can be observed that there has been a considerable interest in developing methods for synthesizing nanoscale nickel phosphides, largely focused on Ni_2P[50-51, 54-55, 58] due to its superior catalytic property. Thus, a variety of other approaches have been reported for the preparation of nanoscale Ni_2P which includes decomposition of single source precursors,[59] high temperature reduction of supported phosphates,[60-61] reaction of supported Ni and NiO particles with PH_3,[62] chemical vapor deposition,[63] solvothermal synthesis[64] and microwave synthesis.[65]

1.6 Thesis Statement

The promise of improved properties has led to an emphasis on the preparation of transition metal phosphides on the nanoscale.[3-4] Thus, over the last decade, a variety of approaches has been reported for the preparation of transition metal phosphide nanoparticles and nanostructures, including solvothermal reactions,[38-40, 66] organometallic decomposition in the presence of phosphiding sources,[46, 50, 52] decomposition of single source precursors,[67] high temperature hydrogen reduction of nanoscale phosphates[68] and sonochemical synthesis.[69] Most of the synthesis methods reported in the literature are empirical studies applicable to the formation of one particular phase. In addition, one of the main difficulties encountered with published syntheses is the parallel formation of other phases as minor products.[67] One of the major goals of our research group is to evaluate the size and shape dependent properties of transition metal phosphides of relevance to catalytic and magnetic applications. To do this, reproducible syntheses that

enable simultaneous control of size and shape and composition need to be developed for transition metal phosphides, which have not yet been demonstrated.

In the dissertation research, we aim to address the issue of phase purity in the transition metal phosphide system by carrying out a detailed investigation of the reaction parameters in order to uncover the key factors that control the formation of various phases. The general methodology reported by Schaak and coworkers[53] is employed to carry out the systematic studies. Among the transition metal phosphides, iron phosphides and their ternary phases have been targeted for their magnetic characteristics, which include ferromagnetism, magneto-resistance and magneto-caloric effects.[19, 66] They exist in a wide range of stoichiometries including Fe_3P, Fe_2P, FeP, FeP_2 and FeP_4. Fe_3P and Fe_2P are ferromagnetic,[3] FeP is metamagnetic[3] and FeP_2[70] and FeP_4[71] are diamagnetic semiconductors. There are conflicting reports on the magnetic properties in nanoscale iron phosphides, likely due to the presence of minute quantities of ferromagnetic impurities in the sample.[48, 50, 52, 72] A systematic evaluation of the synthetic parameters is expected to resolve these outstanding issues. In the dissertation research, the role of temperature, concentration and time on formation of phase-pure Fe_2P and FeP is determined.

Similar to iron phosphides, nickel phosphides also exist in a range of stoichiometries.[73] Among them, Ni_2P supported on silica is reported be an excellent catalyst for the process of hydrodesulfurization when compared to the commercially available sulfided Mo catalysts, as well as other transition metal phosphides.[60-61] However, the phosphate reduction strategy employed for catalyst generation is not favorable for tuning the size and shape of the nanocatalyst. The solution-phase metal

phosphidation approach (Schaak method) is expected to enable better control of these parameters, enabling the roles of active site density and crystallite faces on catalytic activity to be probed.[53-54] In the dissertation research, the fundamental knowledge gained from the study of phase in the Fe-P system is applied to the Ni-P system and additional synthetic levers that enable control of particle size and morphology are uncovered. Morphology conserved transformations were also carried out with the Ni-P system, resulting in the preparation of solid and hollow Ni_2P nanoparticles from corresponding $Ni_{12}P_5$ samples.

Schaak and coworkers reported that oxidation of metal nanoparticles is a key issue that might hamper the conversion to phosphide phases.[53] In the dissertation work, the activity of oxide phases to TOP is probed and it is shown that oxidation is not an impediment to phosphide formation. Indeed even completely oxidized nanoparticles can be transformed into the respective phosphide and sulfide phases by reaction with TOP and sulfur, respectively.

The following chapters will discuss in detail the research projects carried out for this dissertation. Chapter 2 includes description of the experimental methods and the characterization techniques utilized for the preparation and characterization of the as-prepared materials. Chapter 3 discusses in detail the development of the synthetic strategy to control phase on the nanoscale for the iron phosphide system. Chapter 4 describes the successful application of the above mentioned strategy to the nickel phosphide system and the utilization of synthetic levers to control size and morphology for Ni_2P and $Ni_{12}P_5$ nanoparticles. Chapter 5 discusses the unexpected reactivity of oxide nanoparticles and their transformability to the respective phosphides and sulfides. Finally,

Chapter 6 involves a general discussion of the findings of this dissertation and also the future prospects.

CHAPTER 2

EXPERIMENTAL AND MATERIALS CHARACTERIZATION TECHNIQUES

Transition metal phosphides syntheses were carried out by arrested precipitation reactions under an inert atmosphere (Ar). The structural and physical properties of the resultant nanoparticles were studied by a variety of material characterization methods including Powder X-Ray Diffraction (PXRD), Transmission Electron Microscopy (TEM), Energy Dispersive Spectroscopy (EDS), surface area and porosimetry analysis and magnetic susceptibility measurements. This chapter includes a description of the chemicals and general experimental methods used for the preparation of the transition metal phosphide nanoparticles and a detailed discussion of the techniques used to characterize the materials.

2.1 Materials

Iron pentacarbonyl (99.999% metal basis), 1-octadecene (90% tech. grade), sulfur flakes (99.99+%), and nickel oxide nanopowder were purchased from Sigma Aldrich. Oleylamine (C_{18} content 80-90%), octadecylamine (90% tech.), iron (III) acetylacetonate (99%), and cobalt (II) acetylacetonate (99%) were purchased from ACROS Organics. Octyl ether was purchased from TCI America. Nickel (II) acetylacetonate (95%) and bulk nickel oxide powder were ordered from Alfa Aesar. Tri-octyl phosphine (min 97%) was purchased from STREM Chemicals. Manganese (II) acetylacetonate was purchased from AVOCADO Research Chemical Ltd., chloroform (99%) and pyridine (99%) were purchased from Fisher Chemicals. Ethanol (200 proof) was purchased from Decon Labs Inc.

2.2 Experimental Techniques

2.2.1 Glove Box – Inert Atmosphere

A glove box is an essential part of a research laboratory handling air and moisture sensitive chemicals. It consists of a tightly sealed steel box with a plastic window on one side for making observations, one or more pairs of rubber gloves attached to the plastic window, antechambers (big and/or small) with purge and evacuation valves, a source of inert gas (e.g., an Argon cylinder) and a vacuum pump. In some cases, a small refrigerator is available inside the glove box to store chemicals that are unstable at ambient conditions. A photohelic pressure gauge attached to the glove box monitors the pressure inside the box. Positive pressure is always maintained to avoid air getting in via pinhole leaks. Materials are taken in and out of the glove box through the antechambers. Continuous circulation of the inert gas through the catalyst chamber containing molecular sieves and an oxygen getter is performed in order to maintain the box in usable condition. The catalysts in the catalyst chamber are periodically regenerated by heating under a mixture of N_2 and H_2 flow. In the dissertation research, reactions were set up in a VAC Atmospheres glove box equipped with two antechambers and a refrigerator.

2.2.2 Schlenk Line Techniques

A Schlenk line is a glass apparatus consisting of two manifolds for carrying out reactions in a fume hood under an inert atmosphere. One of the manifolds is attached to a vacuum pump via a cold trap and the other is attached to an inert gas source. The manifold has several ports with two way stopcocks that are connected to the sidearm of the Schlenk flasks by flexible tubing while the air sensitive reaction is carried out. A flask containing chemicals is attached to one of the ports and is degassed through the

evacuation manifold. The pump is protected from moisture and other chemicals by using a liquid nitrogen cold trap. Gases purged through the flask and gaseous products formed inside the flask during a reaction escape through an oil bubbler.

2.3 Characterization Techniques

The characteristics of nanomaterials determined in this dissertation research include crystallinity, phase, nanoparticle size, morphology, elemental composition, surface area, pore size and magnetic properties.

2.3.1 Powder X-Ray Diffraction (PXRD)

Powder X-Ray Diffraction provides information about the crystallinity and phase of a material.[74] Each and every crystalline material diffracts uniquely, and thus provides a diffraction pattern that serve as a "fingerprint" for that specific material. The X-ray wavelengths are similar to the inter-atomic spacing in crystals, and thus the atoms in a crystal act as scattering centers resulting in diffraction.[75]

X-rays are produced inside an X-ray tube when high energy electrons collide with a metal target. The three main components of an X-ray tube (Figure 2.1) are (a) a source of electrons (b) a high accelerating voltage and (c) a metal target. A tungsten filament (cathode) generates electrons when it is heated by a filament current of about 100-150 mA. The electrons are directed across the X-ray tube at high velocities to the metal target (anode) by a high accelerating voltage on the order of 30,000 – 50,000 volts. Collision of high energy electrons with the metal target (commonly Cu) generates X-rays, and they pass out of the tube through highly transparent windows made of beryllium. The kinetic energy associated with the high velocity electrons is converted into heat in the target and therefore it is water cooled to prevent melting. The efficiency of X-ray tubes is increased

when the metal target is rotated constantly, thus exposing a fresh target metal to the incident electrons continuously.[74]
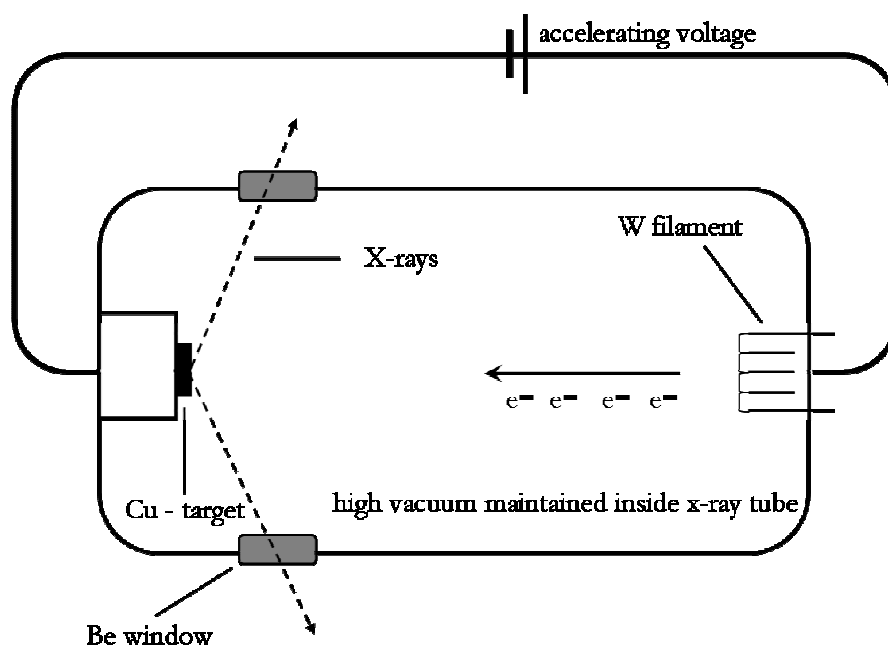
Figure 2.1. Scheme depicting generation of X-rays from a X-ray tube (adapted from Cullity).[74]

X-ray radiation generated inside an X-ray tube can be classified into two different components: (i) white radiation, which encompasses a broad spectrum of wavelengths and (ii) one or more monochromatic radiations. White radiation is caused when the high velocity electrons hit a road block in the form a metal target, resulting in loss of energy, a part of which is converted into electromagnetic radiation. The monochromatic X-rays that are commonly used in all diffraction experiments are generated by a different process that involves ionization of the target metal atoms (Figure 2.2).[75] When the accelerated electrons strike the metal target, they ionize some of the Cu 1s (K shell) electrons. An electron from the outer orbitals (2p or 3p) falls down to the vacant orbital and the

transition, which has a fixed energy, results in emission of characteristic X-rays. The 2p → 1s transition is called the Kα transition (1.5418 Å) and it is more intense than the 3p → 1s transition, known as the Kβ (1.3922 Å), because it occurs with greater frequency.[74-75] A monochromator is used as a filter to ensure a selected wavelength is used for the diffraction experiments.
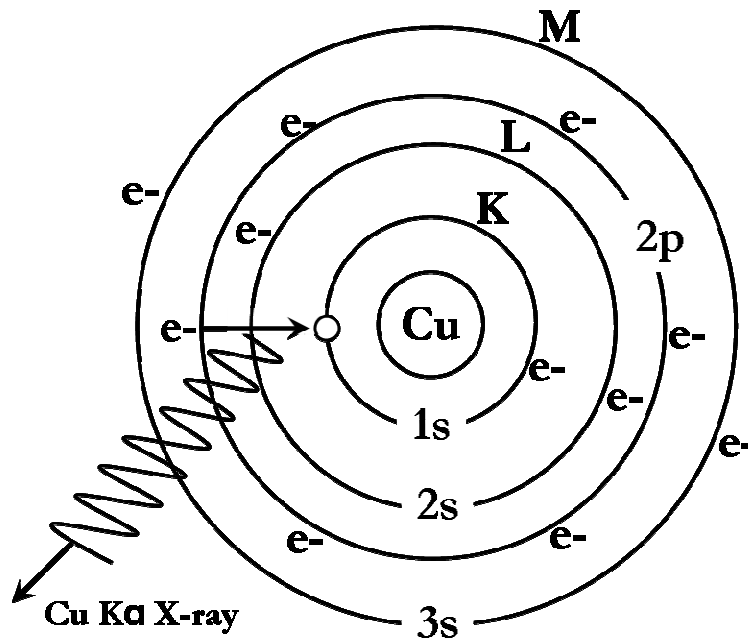
Figure 2.2 Illustration of generation of a Cu Kα X-ray from a Cu atom resulting from the ionization of a 1s electron and subsequent drop of a 2p electron into the vacancy (adapted from West).[75]

Crystals consist of regularly repeating structures that act as optical gratings. When X-rays hit a sample, some of them are reflected at angles equal to the angle of incidence by planes on the surface, while some pass through and are reflected by the inner planes. The reflected X-rays reinforce each other (constructive interference) if they are in phase or cancel out (destructive interference) if not in phase, as shown in Figure 2.3.[75] Consider

two X-ray beams A and B hitting a sample. X-ray beam A gets diffracted as A' by an atom on the surface plane while B passes through the surface plane and is diffracted as B' by an atom in the interior plane. The additional distance travelled by X-ray beam B-B' is defined as XYZ. By applying trigonometry, the distance XYZ can also defined as given in Equation 2.1, where d is the spacing between successive planes in a crystal.

$$2d\sin\theta = XYZ \qquad (2.1)$$

Bragg's law states that there will be constructive interference between the two beams A-A' and B-B' if the distance XYZ equals an integer of the wavelength of the X-ray beam, $XYZ = n\lambda$.[74] The law is thus commonly represented as in Equation 2.2.

$$2d\sin\theta = n\lambda \qquad (2.2)$$

The law imposes a strict condition on the angles that can satisfy the above equation. Destructive interference is bound to happen, even if the incident angle is off by a few-tenths of a degree.

While carrying out a PXRD experiment, it is assumed that the powder sample has crystallites arranged in all possible orientations. The diffracted X-rays are recorded by a detector and the commonly used detectors are movable scintillation detectors or static charge-coupled devices (CCD). The signals detected by the counters are then manipulated into in a one-dimensional plot where X-ray intensities are plotted against 2θ. Constructive interference results in a peak in the plot and the position and intensity of the peak depend on the geometry of the unit crystal and the atoms involved in scattering.[75-76]

The PXRD patterns of nanoparticles have some differences relative to bulk materials. The small crystallite sizes in nanoparticles comprise only a few lattice planes, resulting in incomplete cancellation of scattering occurring at angles that do not satisfy

Bragg's law. Thus the peaks observed for nanoparticles are broader in comparison to corresponding bulk samples.[75-76] The broadening of the peak is inversely proportional to the crystallite size and is defined by the Scherrer formula given in Equation 2.3, where t is the size of the crystallites, λ is the wavelength used for that diffraction experiment, B is the full width at half maximum of the peak and θ is the angle at which the diffraction occurs.

$$t = \frac{0.9\lambda}{B\cos\theta} \tag{2.3}$$
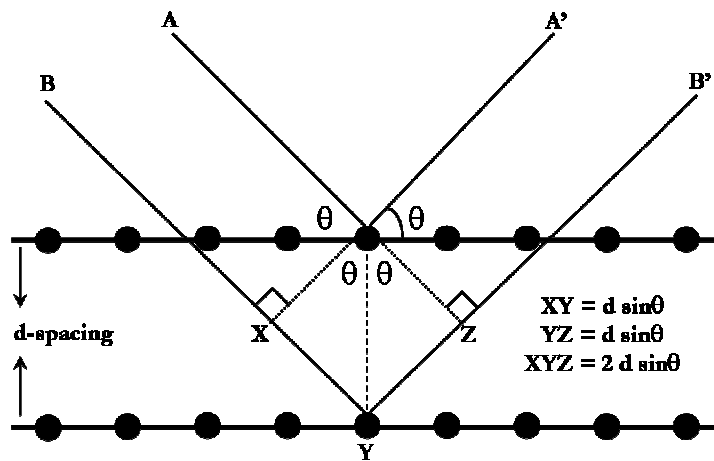
Figure 2.3 Illustration of the diffraction of X-rays by lattice planes in a crystal (Bragg's law, adapted from West).[75]

The growth direction of anisotropic samples such as nanorods and nanowires can sometimes be inferred from the diffraction pattern. More lattice planes are available for diffraction along the growth direction than perpendicular to the growth. Thus, peaks corresponding to reflections that are repeated along the growth direction will appear sharper in the diffraction pattern than reflections with contributions from other directions.

The instrument used for conducting experiments in the dissertation research is a Rigaku RU200B rotating anode 12kW diffractometer using CuKα (1.5418 Å) radiation generated at 40 kV and 150 mA. The instrument has a secondary beam graphite monochromator and a scintillation counter detector with a sodium iodide crystal. Experiments were conducted in the 2θ range 20-82 degrees with a step size of 0.03 degrees. The scan rates were typically 0.6 degrees per minute but in some cases where more resolution was essential, a slower scan rate of 0.3 degrees per minute was used. For analysis, the free flowing dry nanoparticles were deposited on a low background quartz (0001) holder coated with a very thin layer of vacuum grease.

2.3.2 Transmission Electron Microscopy (TEM)

The limited image resolution obtained from light microscopes led to the development of transmission electron microscopes. Louis de Broglie in 1925 first explained the theory that electrons have a wave nature characterized by wavelengths substantially smaller than visible light. Later, Knoll and Ruska proposed the idea of electron microscopes in 1932 and the significance of their proposal can be gauged from the fact that the first commercial electron microscope was developed within the next 4 years.[77] Electrons are preferred over light for imaging for a variety of reasons. They have extremely small wavelengths that can be varied based on the operating voltages. In addition, they can be directed easily, as they are charged particles, and are sensitive, because they are scattered very strongly due to their interaction with both the nucleus and electrons of the scattering atoms.[77]

Modern electron microscopes are versatile tools for materials characterization that can help visualize and identify chemical compositions for particles in the sub-nanometer

to micrometer range. With respect to nanotechnology, electron microscopy is an essential characterization tool because it provides vital information on nanoparticle size, shape, and morphology. High resolution transmission electron microscopy (HRTEM) enables lattice fringes to be imaged and the derived information on lattice planes can help in the identification of crystal structure and crystal growth direction for nanorods and nanowires. In addition to imaging, TEM can help in crystal structure identification through electron diffraction. Similar to a PXRD pattern, the obtained electron diffraction pattern can serve as a fingerprint for a specific material.

In addition to transmission and diffraction, a variety of other events take place when high energy electrons hit the TEM specimen. These secondary processes and their related applications are described in Figure 2.4 and Table 2.1. The capability of detecting these secondary events depends on the addition of accessories to the basic TEM. Some of the common accessories for the TEM include detectors for carrying out energy dispersive spectroscopy (EDS), which provides information on the chemical composition of a sample, electron energy loss spectroscopy (EELS), which is better suited for identifying chemical composition of materials containing light elements and scanning transmission electron microscopy (STEM), which, when coupled with EDS, gives an elemental map along a chosen line of the sample.
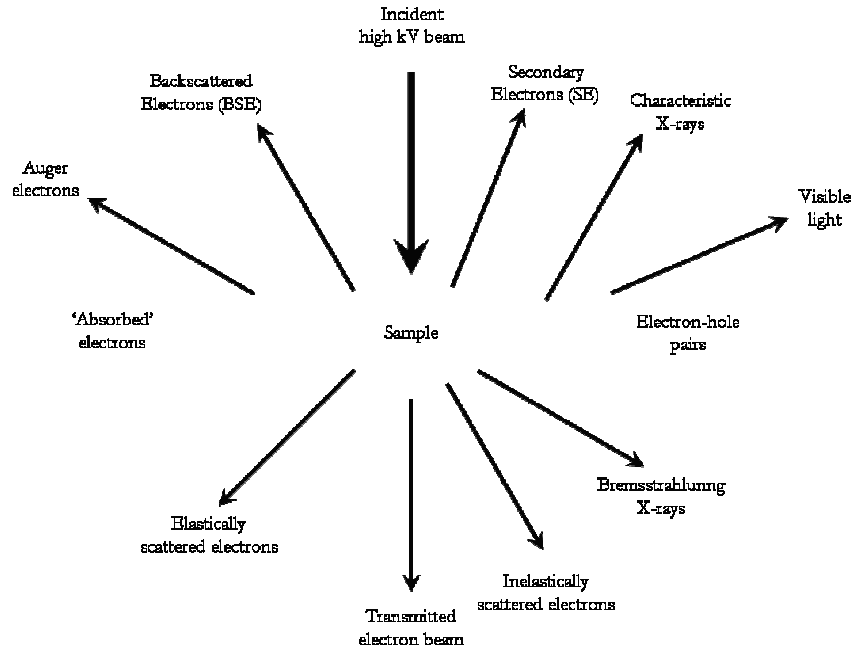
Figure 2.4 Electronic excitations resulting from the interaction of a high energy electron beam on a sample (adapted from Williams).[77]

Table 2.1 Description of the different kinds of radiation generated when a high energy electron interacts with a sample and the corresponding characterization technique

Type of Signal	Application(s)
Auger electrons	Auger Electron Spectroscopy
Backscattered electrons	Scanning Electron Microscopy
Secondary electrons	Scanning Electron Microscopy
Characteristic X-rays	Energy Dispersive Spectroscopy
Inelastically scattered electrons	Transmission Electron Microscopy/ Electron Diffraction
Direct beam	Transmission Electron Microscopy
Elastically scattered electrons	Transmission Electron Microscopy/Electron Diffraction/Scanning Transmission Electron Microscopy/Electron Energy Loss Spectroscopy

A general scheme of a transmission electron microscope is given in Figure 2.5. A reliable source of electrons is essential in order to have good illumination. A tungsten filament or a lanthanum hexaboride crystal is used as an electron source. The sources can be made to emit electrons either thermionically or by the application of an electric field. In a thermionic emission, as the name suggests, electrons are generated when the source (LaB_6) is heated, and a monochromatic electron beam is not produced.[77] There is a limit on the temperature up to which the source can be heated, as higher temperatures might result in evaporation and oxidation, thus resulting in a shortened life time. On the other hand, electrons generated by the field emission method (tungsten filament) are monochromatic.

The TEM is operated under high voltages between 100 kV to 400 kV with the wavelength of the electrons generated depending on the operating voltage, as shown in Equation 2.4, where m_0 is the electron mass, h is Planck's constant, eV is kinetic energy (defined in electron volts) and λ is wavelength. The kinetic energy (eV) of the electrons is determined by the operating voltage (V). The inverse relationship between the wavelength and energy of the electrons is reflected in equation 2.4. This equation must be modified to approximate the wavelength of electrons if the operating voltage is increased beyond 100 kV, as relativistic effects cannot be ignored at electron velocities greater than half the speed of light.[77]

$$\lambda = \frac{h}{\left(2m_0 eV\right)^{1/2}} \tag{2.4}$$
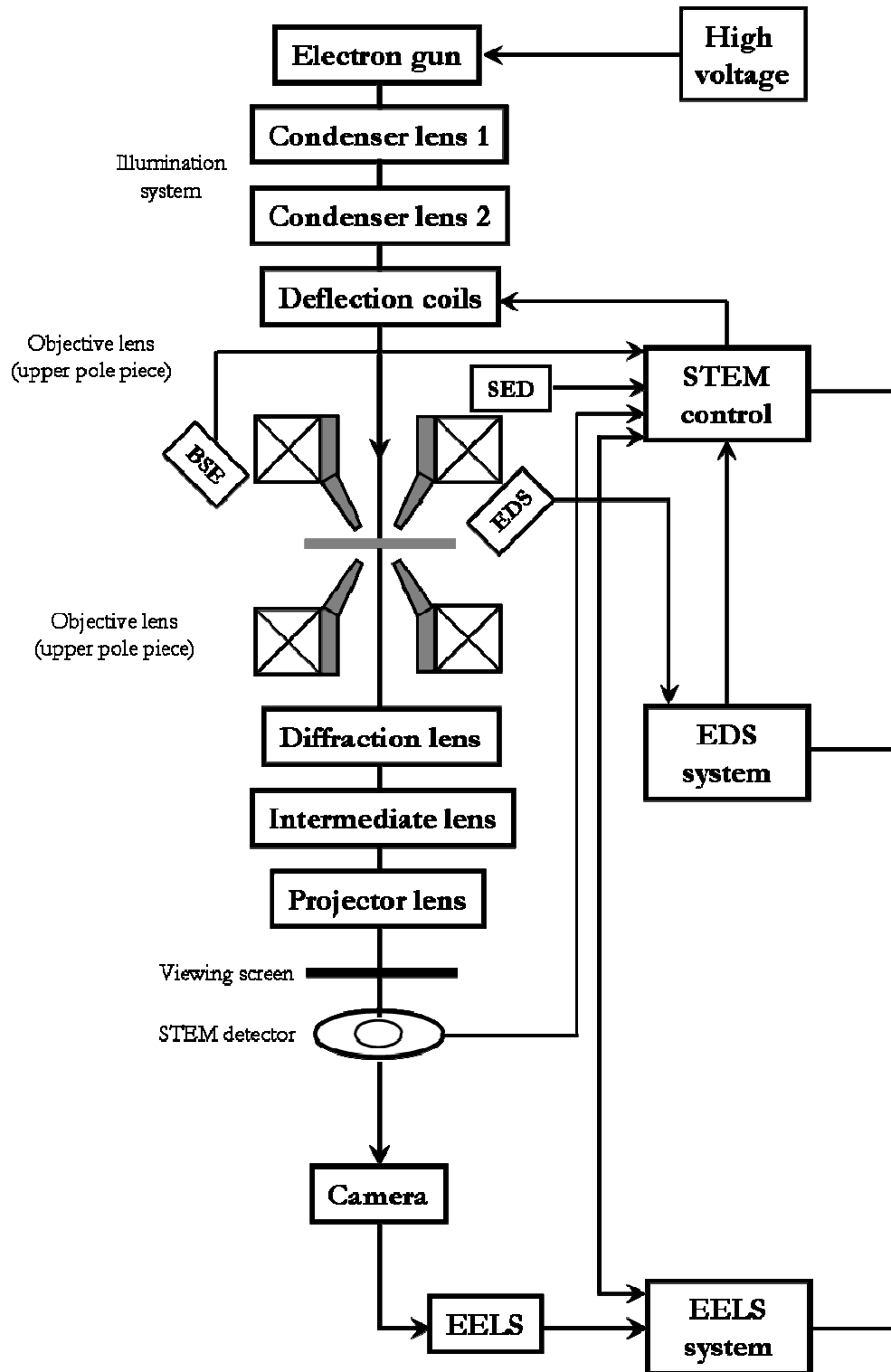
Figure 2.5 Block diagram of a typical TEM with STEM capability (adapted from Fultz).[78]

In a simple imaging mode, both the transmitted and diffracted electrons are used for imaging purposes (Figure 2.6).[77-78] The sample under observation is expected to be uniformly thin, electron transparent and stable under the electron beam. The nanoparticles are supported on grids usually made of copper and coated with a thin carbon film. The contrast of the image depends both on the atomic number (Z) of the elements constituting the sample and also the thickness of the sample. The transmitted and diffracted electrons pass through a series of electromagnetic lenses. The objective lens is the most important lens in a microscope as it helps to construct the image and diffraction patterns, which are further magnified by other lenses (intermediate and projector). The image of the sample can be viewed on a fluorescent screen, or captured by a camera system connected to a computer and stored in digital format.
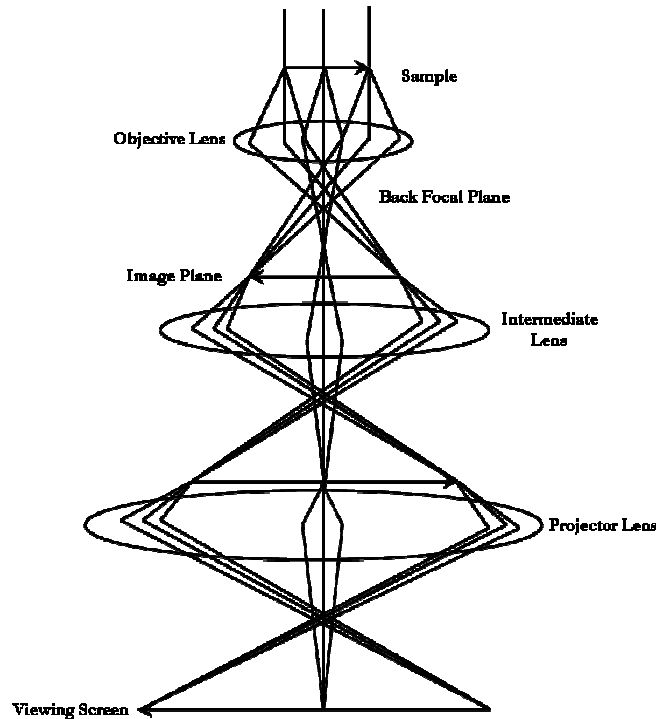
Figure 2.6 Ray paths in a simple imaging mode wherein both transmitted and diffracted electrons are used for imaging purposes (adapted from Fultz).[78]

The quality of the images can be improved by blocking certain parts of the electron beam utilizing the objective aperture to obtain images in bright field and dark field modes. In a bright field imaging mode (Figure 2.7A) the transmitted (undiffracted) electrons are used for imaging and the image forms as a result of the weakening of the transmitted electron beam after interaction with the sample. The sample appears as dark regions and the contrast of the image depends on the electron density and the thickness of the sample. In dark field imaging mode, the transmitted electron beam is blocked using the objective aperture and a part of the diffracted electron beam is used for imaging as shown in Figure 2.7B.[78] The sample (crystalline) is illuminated in a dark field image and the empty area (amorphous) around the specimen is dark. Useful information on defects or faults present in the sample can be obtained from a dark field image as it involves use of the electrons that are diffracted by the sample.
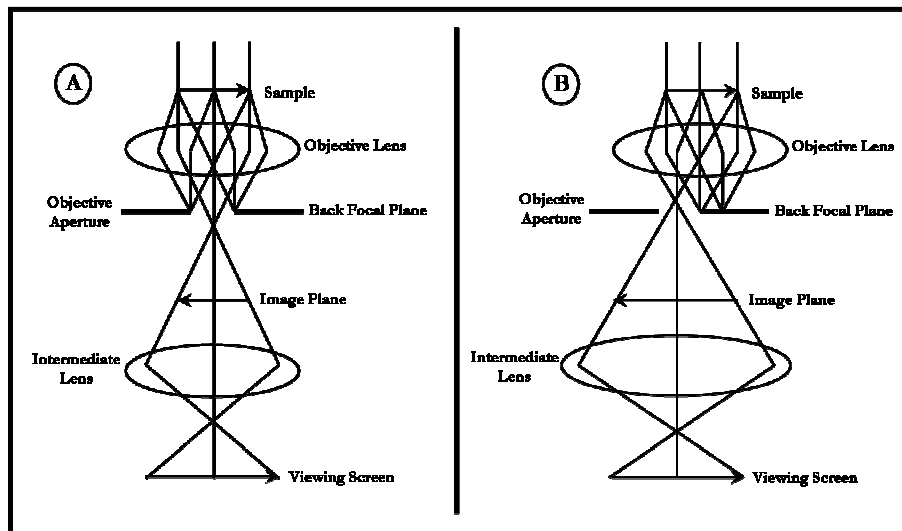
Figure 2.7 (A) Bright field imaging mode wherein only transmitted electrons are used (B) Dark field imaging mode wherein only a section of diffracted electrons are used (adapted from Fultz).[78]

Selected Area Electron Diffraction (SAED) is another technique used in the TEM to obtain information on the crystal structure and its growth direction. A second aperture called the intermediate aperture is positioned in the image plane of the objective lens and is used to restrict the diffraction pattern to a selected area of the specimen (Figure 2.8).[78] During an experiment, the sample is examined in imaging mode first and a region of interest is selected. The microscope is then switched to diffraction mode to observe the SAED pattern. The image consists of rings and spots for polycrystalline and single crystalline samples, respectively. The diameter of the rings, or the distance between two spots directly across the center of the imaginary ring, corresponds to the d-spacing of a specific lattice.
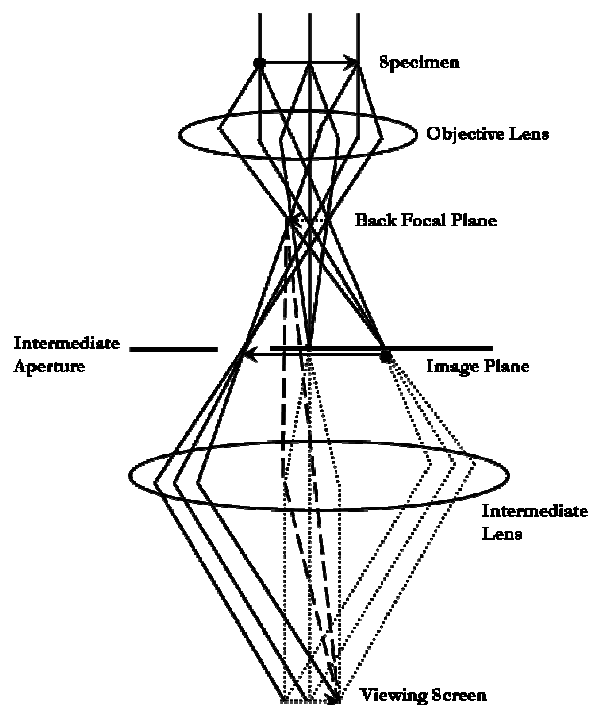
Figure 2.8 Ray diagram depicting the selected area diffraction mode (adapted from Fultz).[78]

In this dissertation research, low and high resolution TEM images were recorded using a JEOL 2010 HR transmission electron microscope operated at 200 kV. Samples for TEM were prepared by placing a drop of a dispersion of as-prepared nanoparticles prepared in chloroform onto a 200 mesh Cu grid coated with a carbon film.

2.3.3 Energy Dispersive Spectroscopy (EDS)

Chemical analysis via Energy Dispersive Spectroscopy can be carried out in electron microscopes due to the availability of the high energy electron beam. As shown in Figure 2.2, the impact of the electron beam on the sample results in the generation of characteristic X-rays. This technique relies on the fact that each atom has its unique atomic structure, and thus the X-rays generated will have characteristic wavelengths.

The generated X-rays can be detected by the EDS accessory attached to the TEM, which comprises a solid state detector system cooled under liquid nitrogen. X-ray photons generated from different elements present in the sample pass through a thin window that isolates the specimen chamber and the detector system and hits the detector. The detector is normally a silicon crystal with a diffused layer of lithium on top of it. Electron-hole pairs are generated in the detector, which are then converted into a charge pulse. A charge-to-voltage converter then converts the charge pulses into voltage pulses. The voltage signal is further amplified by amplifiers and then is sent to the computer where plots of intensity versus voltage are obtained. While generally useful for semi-quantitative analysis, it is not possible to detect light elements (atomic number ≤ 4) with EDS as the low energy X-rays generated from these elements are absorbed by the Be windows of the detectors.

The EDS accessory used in the dissertation research was an EDAX, Inc., detection unit attached to the TEM. EDAX Genesis software version 1.0 was used for analyzing the X-ray intensities to obtain percentage compositions of the elements present in the sample.

2.3.4 Surface Area Analyses

The property of porous solids to attract gases and vapors surrounding them is called adsorption. The uptake of gases by solid surfaces and pores was described as early as 1777 for freshly calcined charcoal, and is found to increase when the solid is cooled down. Monitoring the adsorption phenomenon provides a wealth of information on the surface area and pore structure of the solid under investigation.[79]

Adsorption can be classified into two categories. Physisorption is driven by van der Waals forces of attraction between the gas (adsorbate) and the solid (adsorbent). This process is reversible and non-destructive, due to the nature of the weak forces involved, and therefore leaves the surface of the solid intact. In contrast, chemisorption is driven by the formation of a chemical bond between the adsorbate and adsorbent, and as a result, the electronic structure of the solid at the interface is changed. The nature of the bond can either be covalent or ionic, depending on the species involved in the adsorption process.

When conducting a surface analysis experiment in a gas sorption system, a known quantity of the sample is taken in a glass tube and is subjected to desorption. The desorption is performed by heating the sample under high vacuum or under a gas flow (usually nitrogen) in order to remove common contaminants from the surface and pores of the solid, such as water vapor or small organic molecules. An appropriate desorption temperature is chosen based on the characteristics of the sample, so that the material

under investigation does not undergo a physical or chemical change. After completion of the desorption step, the sample is cooled down to room temperature and the mass of the sample is recorded. The sample tube is now transferred to the analysis unit where it is cooled down to liquid nitrogen temperature (77.2 K). Adsorbate molecules, usually an inert gas such as N_2 or He in the case of physisorption, are then introduced into the sample tube in small quantities. As the molecules are physisorbed, the change in pressure of the gas is recorded. After a certain time, the change in gas pressure is negligible, indicating that the sample surface is saturated. The quantity of gas adsorbed can thus be calculated by application of gas laws given the volume of the sample tube and the mass of the sample.[79]

The quantity of the gas adsorbed by a solid sample is proportional to a number of factors including the sample mass (m), temperature (T) at which the experiment is conducted, the pressure of the gas (P), and the nature of both the adsorbate and the adsorbent. At constant temperature, the amount of gas adsorbed can be calculated as a function of the relative pressure (P/P_0) if the remaining parameters are fixed, where P is the equilibrium pressure and P_0 is the saturation pressure.

An isotherm is obtained when the relative pressure (x-axis) is plotted against volume of gas adsorbed (y-axis). Both adsorption and desorption isotherms are recorded during a surface analysis experiment. The shape of the isotherm provides insight into the nature of the adsorption and desorption processes. A typical gas sorption isotherm consists of several distinguishable regions (Figure 2.9)
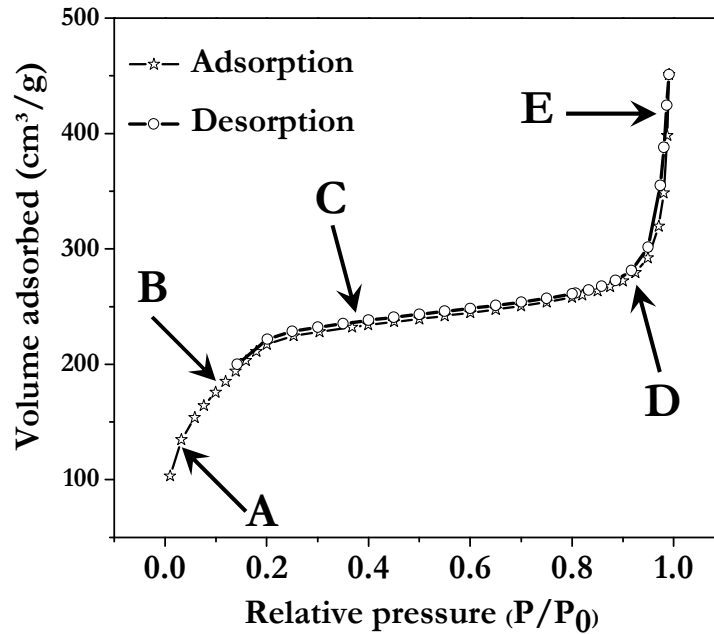
Figure 2.9 Adsorption (red stars) and desorption (blue circles) of a porous solid exhibiting the different steps of a gas adsorption experiment. A-micropore filling, B-monolayer formation, C-multilayer adsorption, D-onset of pore filling and E-capillary condensation.

When adsorbate is introduced into the sample tube at relatively low pressure, the micropores (< 2 nm) are filled first. With further increase in the pressure, adsorbate molecules form a monolayer coverage on the sample surface. After complete monolayer coverage is achieved, multilayer adsorption takes place, leading to filling of mesopores (2-50 nm) and macropores (< 50 nm). At relatively high pressures, capillary condensation occurs, where gas molecules condense into a liquid.

Figure 2.10 shows the different types of isotherms classified based on their shape. Type I, is characteristic of materials having extremely small pores. Type II and IV are indicative of either a nonporous material or an adsorbent containing relatively large

pores. Type III and Type V isotherms result when the adsorbate molecules have greater affinity for each other than the solid surface. Type VI is a rare isotherm that is indicative of a nonporous solid with a very smooth surface. For porous materials, hysteresis loops are observed in the isotherms due to differences in the rate at which the pores are filled and emptied.[79] It should also be noted that an absence of a loop is not conclusive evidence of nonporosity as conical, wedge shaped, and closed-end pore geometries can also yield isotherms without hysteresis.[80]
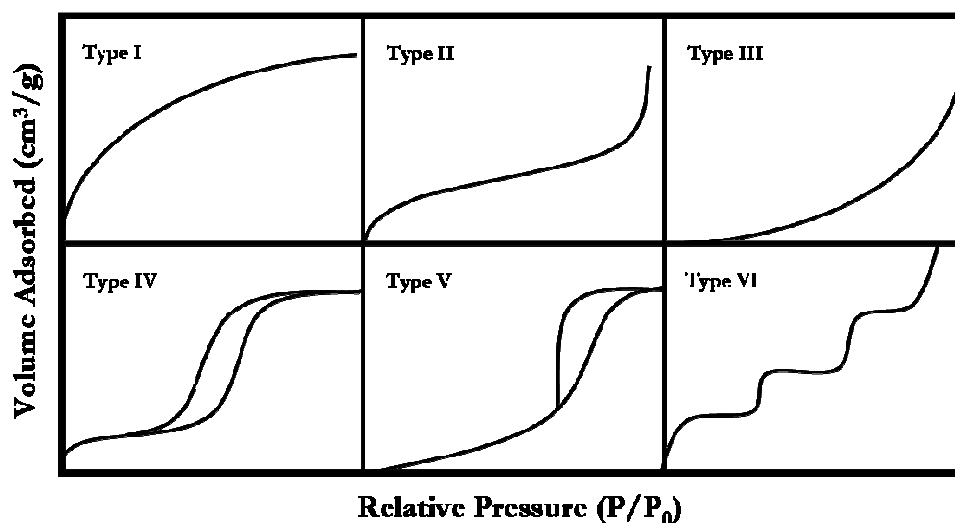
Figure 2.10 Six basic types of adsorption isotherms (adapted from Webb).[80]

The surface areas and pore size distributions are obtained by the application of theoretical models to the adsorption/desorption isotherms. The model developed by Langmuir is more suited to the chemisorption phenomena as it is based on the assumption that only one molecular layer is formed on the surface of an adsorbent.[79] The BET theory developed later by Brunauer, Emmett and Teller incorporates the multilayer adsorption of

adsorbate molecules. BET utilizes the adsorption region (P/P_0 = 0.02 to 0.20) of the adsorption isotherm to compute surface area using Equation 2.5

$$\frac{P}{V_a(P_0 - P)} = \frac{1}{V_m C} + \frac{C-1}{V_m C}\left(\frac{P}{P_0}\right) \tag{2.5}$$

where V_a is the volume of the gas adsorbed at a given relative pressure (P/P_0), V_m is the volume of the gas required for monolayer coverage and C is a constant. The values for V_m and C can be obtained from a plot of $P/(V_a(P_0\text{-}P))$ *vs.* P/P_0. The plot yields a straight line and the values for V_m and C can be obtained from the slope and intercept.[80]

Pore volumes, average pore size and pore size distributions are obtained by application of the BJH model developed by Barrett, Joyner and Halenda in 1951, which uses the Kelvin equation (Equation 2.6)

$$\ln\left(\frac{P*}{P_0}\right) = \left(\frac{2\gamma v \cos\theta}{RT r_m}\right) \tag{2.6}$$

where, $P*$ is the critical condensation pressure, γ is the liquid surface tension, v is the molar volume of the condensed adsorptive, θ is the contact angle between the solid and condensed phase, r_m is the mean radius of curvature of the liquid meniscus, R is the ideal gas constant and T is the absolute temperature. The theory is commonly used to model cylindrical pores and it collects information mainly from the region where pore filling and emptying take place in the adsorption/desorption isotherm.[80] As the pressure gradually decreases during desorption, the adsorbate is removed from the pores. The removal of adsorbate in each step directly corresponds to the volume of pores emptied. Since BJH assumes that all pores are cylindrical, the pore lengths (l) can be computed by substituting the values of obtained pore radius and adsorbed pore volumes in the general

equation used to compute cylinder volumes ($\pi r^2 l$). Cumulative pore volumes are calculated by adding the pore volumes calculated in each step of the isotherm.

In the dissertation research, adsorption and desorption isotherms were obtained using N_2 as the adsorbate in a Micromeritics ASAP 2010 porosimeter. Surface areas were computed using the BET model and pore sizes and their distribution were determined using the BJH model.

2.3.5 Superconducting Quantum Interference Device (SQUID) DC Magnetometry

A magnetometer is a device that measures the magnetization of a given material. There are a variety of magnetometers and among them the Superconducting Quantum Interference Device (SQUID) magnetometers are the most sensitive detectors of magnetic flux.[81] A general schematic of a SQUID magnetometer is given in Figure 2.11. The SQUID magnetometer combines the physical phenomena of flux quantization and Josephson tunneling.[81] The DC SQUID (Figure 2.12) consists of two Josephson junctions, consisting of two superconductors separated by a thin insulator, connected in parallel on a superconducting loop. The SQUID records the change in current, which is directly proportional to the change in magnetic flux associated with the sample under investigation. The sensitivity of SQUID is of the order 10^{-9} emu, which allows detection of very small changes in magnetic moments.

Most SQUIDS are made of low T_c superconductor Niobium and are operated at liquid ^{4}He temperatures (4.2 K).[82] Typically, magnetic fields produced in the instrument can be varied between 0.01 - 5 Tesla. Measurements can also be carried out as a function of temperature and a typical range is 5 K to 350 K. For carrying out an experiment on air sensitive materials, a known quantity (10-50 mg) of the sample is taken in a small

capillary tube closed at one end. It is tightly packed and is sealed either under vacuum or argon. The capillary tube containing the sample is then placed in a plastic straw and is centered inside the superconducting coils using software control. Magnetic flux is a function of the applied magnetic field and the change in effective cross-sectional area. Moving the sample inside the magnetometer results in a change in the cross-sectional area of the sample exposed to the magnetic field, resulting in a change in the magnetic flux as given by Equation 2.7, where $\Delta\varphi$ is the change in magnetic flux, B is the applied magnetic field, ΔA is the change cross-sectional area and θ is the angle between sample cross-sectional area and the magnetic field. In our measurements, since the sample is placed parallel to the magnetic field, the θ becomes zero and $\cos\theta$ equals unity. The change in cross-sectional area induces a change in the current flowing through the superconducting coils, which is then converted into magnetic flux.

$$\Delta\phi = B\Delta A\cos\theta \tag{2.7}$$
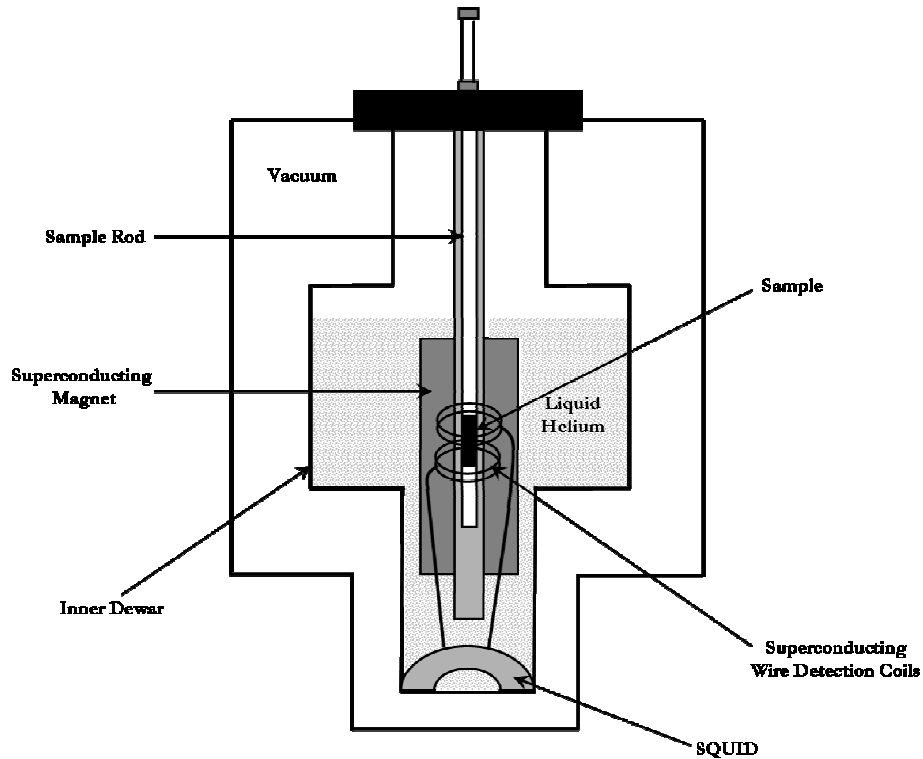
Figure 2.11 General schematic of a SQUID magnetometer (adapted from the manual of

Magnetic Property Measurement System (MPMS) 5S from Quantum Design).
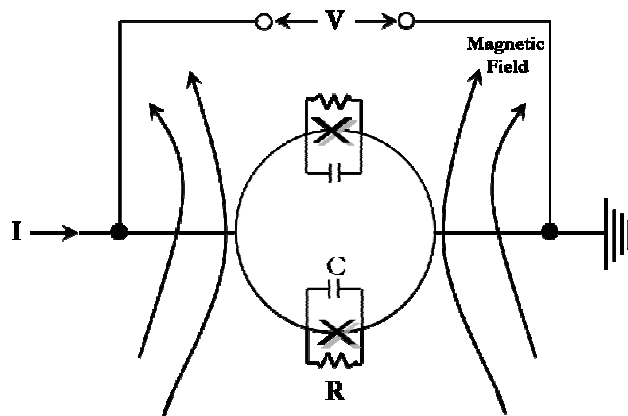
Figure 2.12 General schematic of a SQUID. A superconducting ring is connected to two

Josephson junctions. In this figure, I represents current, C is a capacitor, R is resistor and

V is voltage that is monitored (adapted from Clarke).[82]

For the dissertation research, magnetic susceptibility measurements were carried out using an MPMS-5S SQUID magnetometer from Quantum Design with a sensitivity of 10^{-7} to 10^{-6} emu. Samples for magnetic susceptibility were prepared by sealing the powder sample in a quartz tube under vacuum. The temperature-dependent dc magnetization measurements were measured using a zero-field cooled (ZFC) protocol from 20 to 350 K in a magnetic field of 100 Oe or 2 T. A similar measurement was carried out over the same temperature range and magnetic field using a field-cooled (FC) protocol. Arrott plots, a series of M^2 versus H/M lines, were generated from *M vs. H* curves collected at several temperatures (200-235 K) near the expected Curie temperature. For NiO nanoparticles, M *vs.* H curves were collected in a Quantum Design Physical Property Measurement System (PPMS) at 300 K between -5 kOe and 5 kOe.

CHAPTER 3

CONTROL OF PHASE IN IRON PHOSPHIDE NANOPARTICLES PREPARED BY METAL NANOPARTICLE TRANSFORMATION

3.1 Introduction

As mentioned in Chapter 1, iron phosphides exist in a wide range of stoichiometries including Fe_3P, Fe_2P, FeP, FeP_2 and FeP_4, and the properties depend sensitively on their physical and electronic structure.[3, 71, 83-84] Accordingly, a significant effort has been applied towards the synthesis of iron phosphides on the nano-scale. Yet, the factors that determine the specific phases generated have not been well documented and the purity of some of the phases reported are debatable. Thus, there is a need to understand the factors that control phase in the synthesis of nanoscale iron phosphides, and to exploit them to establish their intrinsic properties. Schaak and coworkers transformed a variety of transition metal nanoparticles into their respective phosphide phases utilizing tri-octyl phosphine (TOP) as a reactive source of phosphorus.[53] This metal nanoparticle conversion method is adapted here to study the formation and stabilization of different phases of Fe-P.

This chapter discusses in detail the role played by different reaction parameters such as heating time, temperature and concentration of precursors (Fe and P) in determining the phase of the final product. The detailed evaluation resulted in a set of optimal conditions for the preparation of phase-pure samples of Fe_2P and FeP, and the intrinsic properties of these distinct phases were characterized by magnetic susceptibility measurements.

3.2 Experimental Section

All chemicals used for the syntheses described in this chapter are listed in Section 2.1.

3.2.1 Synthesis of Fe nanoparticles and subsequent transformation to phosphide

The synthesis of iron phosphides consists of two steps and is outlined in Scheme 3.1. The first step involves the preparation of monodisperse Fe nanoparticles by following a published method by Sun and coworkers.[85] In the second step, the Fe nanoparticles are converted into phosphides by reaction with TOP. Fe nanoparticles are synthesized by injecting 0.2-1.0 mL of $Fe(CO)_5$ into a degassed system of 20.0 mL octadecene (solvent) and 0.3 mL oleylamine (stabilizing ligand) at 200 °C. The system is aged at 200 °C for 20 minutes. Conversion of Fe nanoparticles is initiated by injecting TOP (2.5-26.5 mL) into the Fe nanoparticles system at 200 °C followed by aging at temperatures of 350, 370 or 385 °C for periods ranging from 1 h to 72 h (PATH A). In some cases, conversion was initiated by cannulating the Fe nanoparticles at 200 °C into TOP maintained at temperatures > 300 °C (PATH B). Isolation of the final products was carried out, after returning the system to room temperature, by addition of excess ethanol (20-50 mL), followed by centrifugation. The isolated nanoparticles were then sonicated for about 5-10 minutes with small quantities of chloroform (1-3 mL) to create a dispersion, followed by addition of an anti-solvent (ethanol) and centrifugation. This process was carried out 2-3 times followed by drying under vacuum to yield a free-flowing powder of Fe_xP nanoparticles.
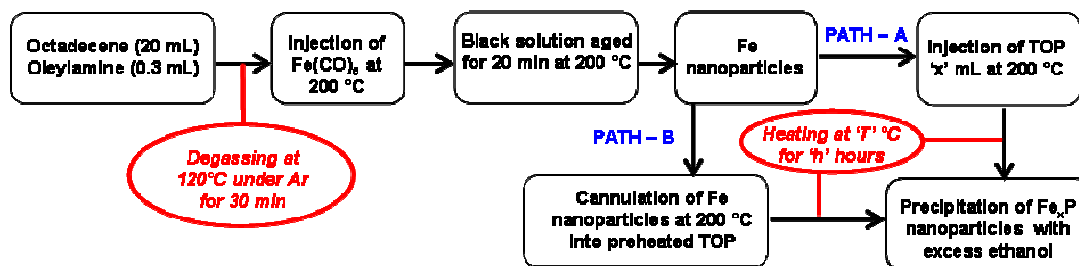
Scheme 3.1 Fe nanoparticle synthesis and subsequent conversion to Fe$_x$P nanoparticles. Reproduced with permission from reference[86]. Copyright 2009 American Chemical Society.

3.2.2 Magnetic susceptibility measurements on iron phosphide nanoparticles

The temperature dependent dc magnetization measurements were measured using a zero-field cooled (ZFC) protocol from 20 K to 350 K in a magnetic field of 100 Oe. The measurement is then repeated over the same temperature range and magnetic field using a field-cooled (FC) protocol. FC measurements were also carried out on FeP samples under an applied field of 2 Tesla in the temperature range 20 K to 350 K. Arrott plots, a series of M^2 *vs.* H/M lines, were generated from M *vs.* H curves collected at several temperatures (200-300 K) near the estimated T_c.

3.3 Results and Discussion

3.3.1 Synthesis and characterization of Fe nanoparticles

Spherical Fe nanoparticles were synthesized by injecting a known quantity of Fe(CO)$_5$ into a degassed mixture of octadecene and oleylamine maintained at 200 °C. Within a few minutes, the system changed from colorless to black, indicating the formation of Fe nanoparticles. TEM analyses of aliquots taken from the reaction system after 20 minutes indicated formation of spherical nanoparticles with a core-shell structure

(Figure 3.1a). The shell can be attributed to the surface oxidation of reactive Fe nanoparticles during isolation.[87] A size distribution plot (Figure 3.1b) for these nanoparticles indicates that they are nearly monodisperse with an average size of 15.0 ± 0.7 nm (core plus shell). In line with the literature reports, the PXRD pattern of the Fe nanoparticles is featureless, indicating that they are amorphous (Figure 3.1c).[85] The isolated nanoparticles are attracted to the magnetic stir bar, consistent with formation of a magnetic phase (Fe or Fe oxide).
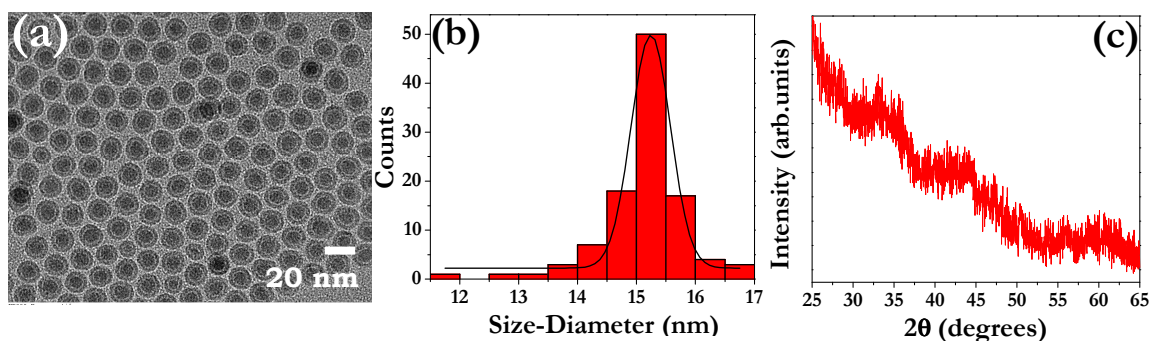
Figure 3.1 Characterization of Fe nanoparticles: (a) TEM image, (b) Size distribution histogram and (c) PXRD pattern. Reproduced with permission from reference[86]. Copyright 2009 American Chemical Society.

3.3.2 Conversion of Fe nanoparticles into iron phosphides

In-situ conversion of the Fe nanoparticles (aged for 20 minutes) into phosphide phases was initiated by either injection of TOP into the Fe nanoparticle system at 200 °C followed by raising the temperature to 350-385 ℃ for time intervals of one hour to several days (Scheme 3.1, PATH-A) or by cannulation of the Fe nanoparticles at 200 °C into preheated TOP maintained at 350-370 °C (Scheme 3.1, PATH-B). A series of

reactions were conducted in which reaction temperature, reaction time, and Fe and P precursor amounts were independently varied in order to discern the key parameters governing phase formation and transformation within the Fe_xP nanoparticle system and the optimal conditions to prepare phase-pure samples.

3.3.2.1 Effect of time at 350 °C: Reaction Series I

As a phosphorus source, TOP is relatively inert, requiring high temperature for activation (presumably by P-C bond cleavage) and producing lower yields of active phosphorus relative to $P(SiMe_3)_3$ (activation by P-Si bond cleavage and employed as a stoichiometric reagent).[46] Accordingly, we hypothesized that the amount of active phosphorus available to react with Fe nanoparticles could be manipulated by adjusting the temperature and the reaction duration. In order to test this hypothesis, we started the conversion reactions at 350 °C using PATH-A and varied the heating time from 1 h to 24 h. The PXRD patterns for the final products are given in Figure 3.2. The PXRD pattern of the 1 h sample indicated formation of a poorly crystalline material with broad peaks that can be indexed largely to Fe_2P. The samples made at longer heating times were characterized to be a mixture of both Fe_2P and FeP, with the former being the major product at short reaction times and the relative amount of the latter going up with increasing reaction time. The specific quantities of Fe_2P and FeP were not determined because we found that even small variations in reaction setup (using a different mantle or temperature probe) result in different relative quantities of the two species. Nevertheless, the trends observed in this investigation are completely reproducible.
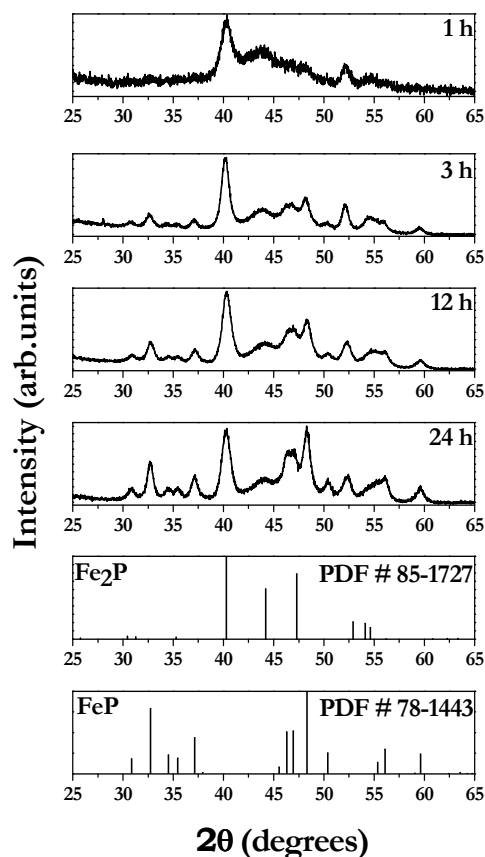
Figure 3.2 PXRD patterns of the final products from PATH-A (Scheme 3.1) as a function of heating time at 350 °C, compared to reference patterns for FeP and Fe$_2$P. Reproduced with permission from reference[86]. Copyright 2009 American Chemical Society.

With respect to morphology, products of the 1 h reaction were found to consist mostly of rods (Figure 3.3a) whereas the samples heated for longer times were found to be a mixture of both rods and spherical particles (Figure 3.3b). The change in morphology of the particles may be attributed to the gradual change of the reaction product from the Fe-rich product to a P-rich product. Orthorhombic FeP prepared on the nanoscale has been reported as either spherical particles[46] or rods[50, 52] and hexagonal Fe$_2$P

is reported to favor formation of nanorods with preferential growth along the [001] axis.[48, 50, 67] Hollow structures are observed in the spherical particles as well as the rods, similar to the hollow structures reported by Schaak and coworkers[53-54] and Chiang and coworkers for Ni_2P, produced by metal nanoparticle conversion.[55] The formation of hollow structures is attributed to the nanoscale Kirkendall effect[56] occurring due to the difference in the diffusion rates of Fe ions outward and P ions inward. At short times (1 h), the products are strongly attracted to a stir bar. This suggests that iron conversion is incomplete, based on the fact that neither Fe_2P nor FeP are expected to be magnetic at room temperature. In contrast, particles isolated after 3 h or longer were no longer magnetic, suggesting the iron had completely reacted.
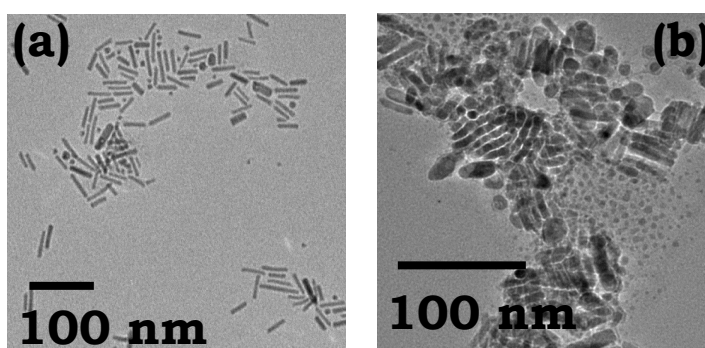
Figure 3.3 TEM images of Fe_xP nanoparticles prepared at 350 °C (PATH-A, Scheme 3.1) with different reaction times. (a) 1 h and (b) 24 h. Reproduced with permission from reference[86]. Copyright 2009 American Chemical Society.

3.3.2.2 Effect of precursor concentration: Reaction series II and III

The role of precursor concentrations, in determining the phase and phase-purity of the final product was explored next. During the conversion, the amount of TOP was varied from 2.5 mL to 26.5 mL (5.6 mmol to 59.4 mmol) was varied, while heating for 24

h at 350 °C. PXRD data suggested a mixture of phases with varying compositions of Fe_2P/FeP (Figure 3.4a). At low concentrations of TOP (5.6 mmol) the Fe-rich product (Fe_2P) was favored, whereas FeP formation was favored when more TOP was used in the reaction, suggesting a higher concentration of "available" phosphorus can drive conversion of Fe and/or Fe_2P to FeP. However, even for very large TOP amounts, Fe_2P remains a significant byproduct.

The concentration of Fe precursor ($Fe(CO)_5$) was also varied, keeping all other reaction parameters constant, with the expectation that increasing the available iron would favor the Fe-rich product (Fe_2P). The PXRD patterns of the final products are given in Figure 3.4b. For 0.4 mL (3 mmol) $Fe(CO)_5$ or lower, the final product was indexed to both FeP and Fe_2P phases, whereas the samples made with higher amounts of $Fe(CO)_5$ (0.8 mL, 6 mmol and 1.0 mL, 7.6 mmol) could be uniquely indexed to the Fe_2P phase. Increasing the precursor molar ratio of Fe:P from 0.067 to 0.34 results in a higher concentration of Fe nanoparticles and thereby promotes formation of the Fe-rich product (Fe_2P) while simultaneously eliminating the phosphorus rich product (FeP).
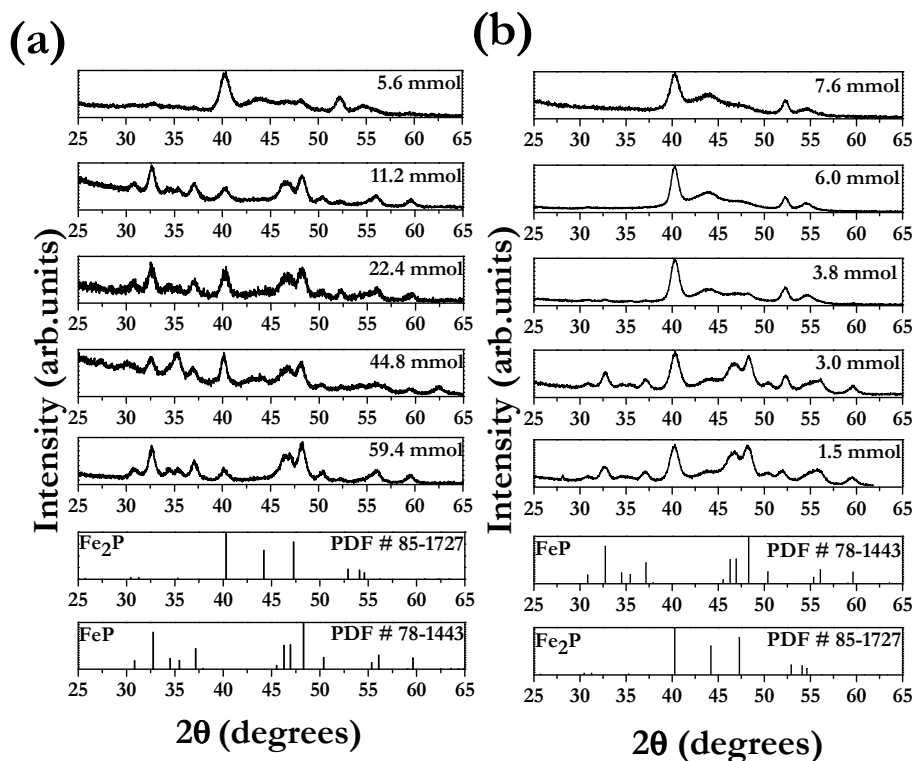
Figure 3.4. (a) Reaction Series II: PXRD patterns of the products from PATH-A
(Scheme 3.1) as a function of TOP quantity; reactions were carried out at 350 °C for 24 h
with 0.35 mL (2.7 mmol) $Fe(CO)_5$. (b) Reaction Series III: PXRD patterns of the products
from PATH-A (Scheme 3.1) as a function of $Fe(CO)_5$ quantity; reactions were carried out
at 350 °C for 6 h with 10 mL (22.4 mmol) TOP. Reproduced with permission from
reference[86]. Copyright 2009 American Chemical Society.

3.3.2.3 Optimal conditions for the generation of phase-pure nanoscale Fe₂P

Despite appearing phase-pure in the PXRD pattern, the 6 h Fe_2P samples prepared
with ≥ 0.8 mL $Fe(CO)_5$ were found to respond to a magnetic stir-bar at room temperature,
suggesting the possible presence of unconverted Fe nanoparticles in the final product. To
enable complete conversion to the iron-rich phosphide phase (Fe_2P), reactions were

carried out for a longer duration (24 h) with an intermediate amount of $Fe(CO)_5$ (0.7 mL, 5.3 mmol) and 5 mL (11.2 mmol) TOP. The PXRD pattern (Figure 3.5a) of the sample again matches well with the reference pattern for Fe_2P but the sample is not attracted to the stir bar, suggesting conversion is complete in this case. TEM images (Figure 3.5b) of the final product indicated that the sample consisted mainly of rods of varying lengths (40 nm to 110 nm) with an average width of 8 nm. A small number of near spherical particles was also observed.
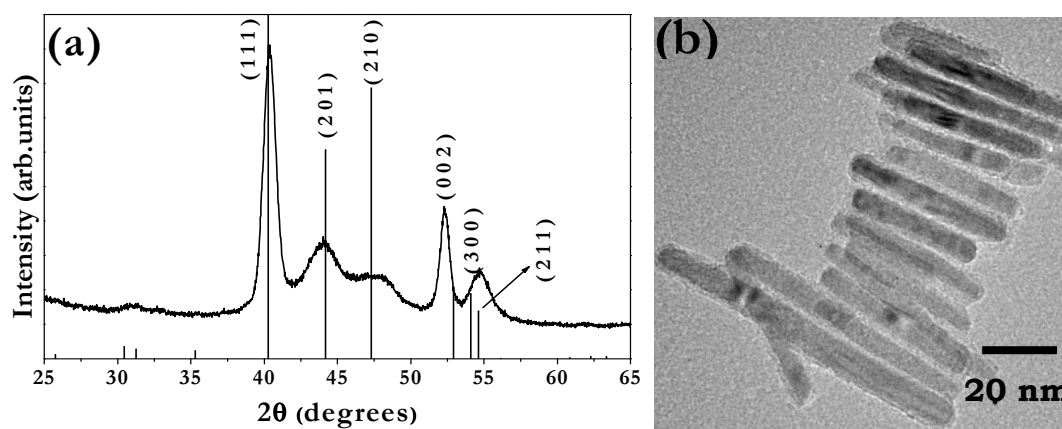
Figure 3.5 (a) PXRD pattern of Fe_2P nanorods indexed to their reference pattern and (b) TEM image confirming the formation of rod structures. Reproduced with permission from reference[86]. Copyright 2009 American Chemical Society.

3.3.2.4 Magnetic properties of Fe_2P nanorods

The magnetization (M) as a function of temperature (T) for Fe_2P nanorods was measured using ZFC and FC measurement protocols at an applied field of 100 Oe and is shown in Figure 3.6a. Both curves show a sharp rise in susceptibility below 250 K, consistent with the onset of ferromagnetic order. To determine the exact T_c of the Fe_2P sample, M *vs*. H curves were collected at temperatures around the expected the T_c (200-

265K) and plotted as M^2 *vs.* H/M (Arrott plots, Figure 3.6b). For a second order phase transition, such as the magnetic ordering transition observed here, these Arrott plots yield a set of parallel lines with the curve corresponding to $T=T_c$ passing through the origin.[88] The collected data indicates that the 215 K and 220 K measurements pass on either side of the origin, suggesting T_c for the nanorods occurs between these two values. The observation agrees with the transition temperature for bulk Fe_2P (217 K) reported by Fujii and coworkers.[49]
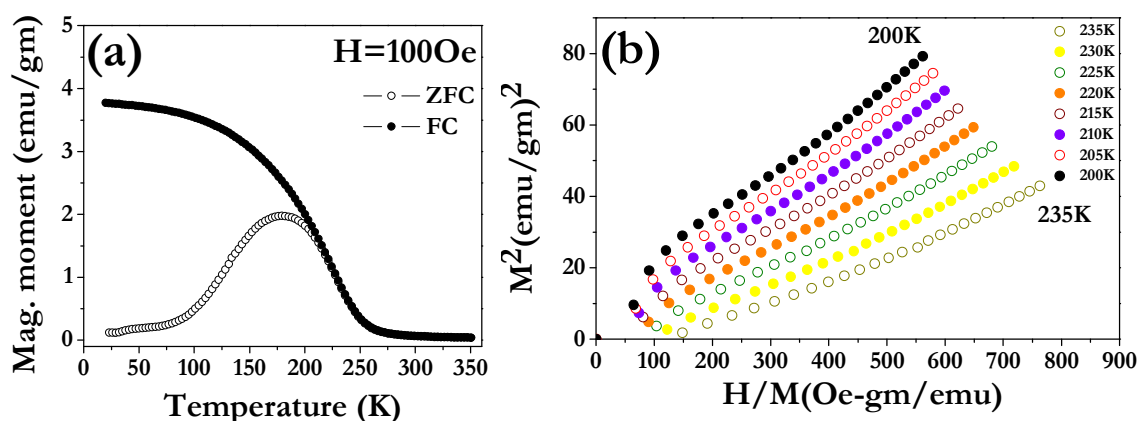
Figure 3.6 (a) Magnetization *vs.* temperature data of Fe_2P nanorods and (b) Arrott plot measurements to determine T_c. Reproduced with permission from reference[86]. Copyright 2009 American Chemical Society.

ZFC/FC measurements were carried out to assess the superparamagnetic behavior, characteristic of nanoscale ferromagnets. The superparamagnetic transition, or T_b, refers to the temperature at which the thermal energy dominates the magnetic energy and is expected to be lower than the corresponding T_c. For a nanoparticle system, T_b typically increases with increased magnetic volume and magnetocrystalline anisotropy.

The ZFC measurement (Figure 3.6a) carried out on the Fe_2P nanorods in Figure 3.5, exhibits a peak around 179 K, which is consistent with the expected behavior of a nanoscale ferromagnet. These results indicate that previous studies on nanoscale Fe_2P reporting T_b values[48, 66] greater than T_c and/or where hysteresis loops[67] are observed at temperatures above T_c could be due to contamination by metallic or oxidized iron species, or possibly Fe_3P (T_c= 716 K). The unreliability of PXRD for purity assessment in cases where ferromagnetic impurities are likely, is emphasized by this study.[89] In the present case, the attraction of the material to a stir-bar at room temperature suggests the presence of common Fe-based impurities and provides an easy check for these secondary phases. This is particularly valuable for the phosphides, because the presence of TOP as a capping ligand precludes using chemical analysis for evaluation of phase-pure samples as all materials appear to be phosphorus-rich.[58]

3.3.2.5 Effect of temperature on the final product: Reaction series IV and V

To be able to make the phosphorus rich product (FeP), a larger quantity of reactive phosphorus is needed. According to the hypothesis previously stated, this could be achieved by increasing the temperature, enabling complete conversion of Fe nanoparticles to FeP nanoparticles without Fe_2P impurities. A series of reactions, similar in conditions to reaction series I, were carried out at 370 °C (reaction series IV) and 385 °C (reaction series V) and the products were analyzed by PXRD (Figure 3.7). The results were similar to those observed in reaction series I, i.e., longer heating times reduced, but failed to completely eliminate, Fe_2P. However, increasing temperature did significantly decrease the amount of Fe_2P (Figure 3.8), as assessed from the intensity of the (111) reflection of Fe_2P (40.2^o 2θ). This is consistent with the hypothesis that more of the TOP

is activated, yielding a higher concentration of phosphorus available for conversion and resulting in the formation of phosphorus rich product (FeP) in higher quantities.
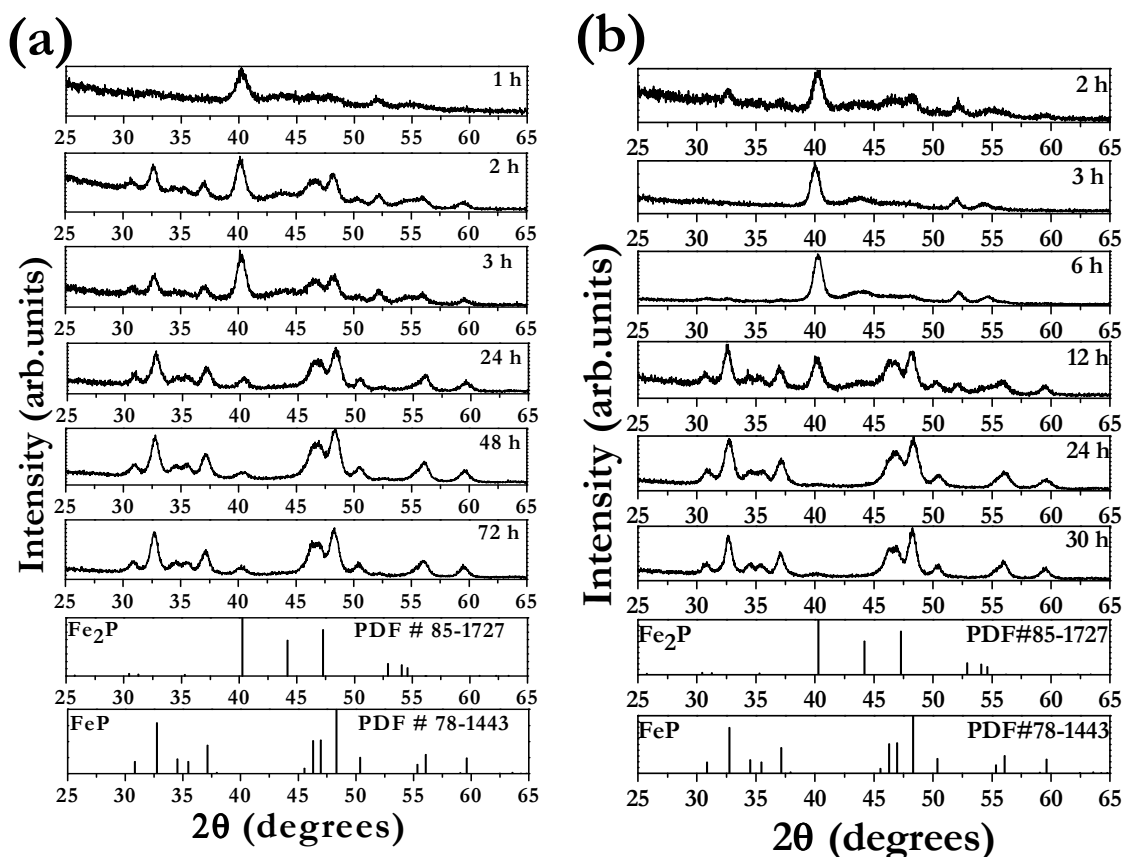
Figure 3.7 PXRD patterns of products as a function of heating time compared to the reference patterns of FeP and Fe$_2$P. (a) Reaction series IV carried out at 370 °C (PATH-A, Scheme 3.1) and (b) Reaction series V carried out at 385 °C (PATH-A, Scheme 3.1). Reproduced with permission from reference[86]. Copyright 2009 American Chemical Society.

In an attempt to drive the reaction to completion, a second injection of 10.0 mL TOP was carried out halfway through a 24 h reaction at 370 °C, but the PXRD pattern indicated the failure to eliminate Fe$_2$P impurities (Figure 3.9).
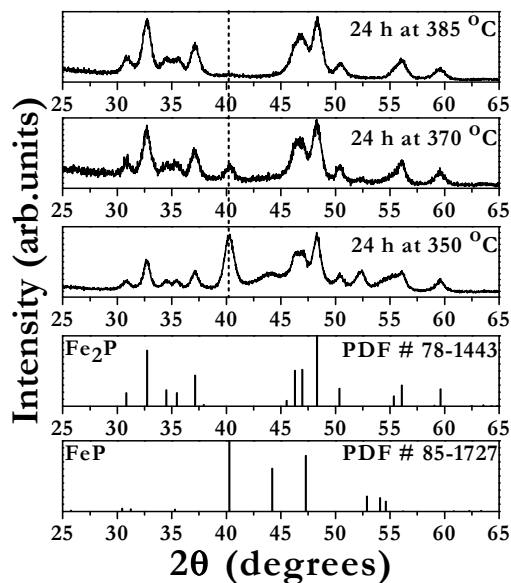
Figure 3.8 PXRD patterns depicting the effect of temperature on the distribution of FeP

and Fe_2P in the product produced by PATH-A (Scheme 3.1). The characteristic peak of

Fe_2P is marked with a dotted line. Reproduced with permission from reference[86].

Copyright 2009 American Chemical Society.
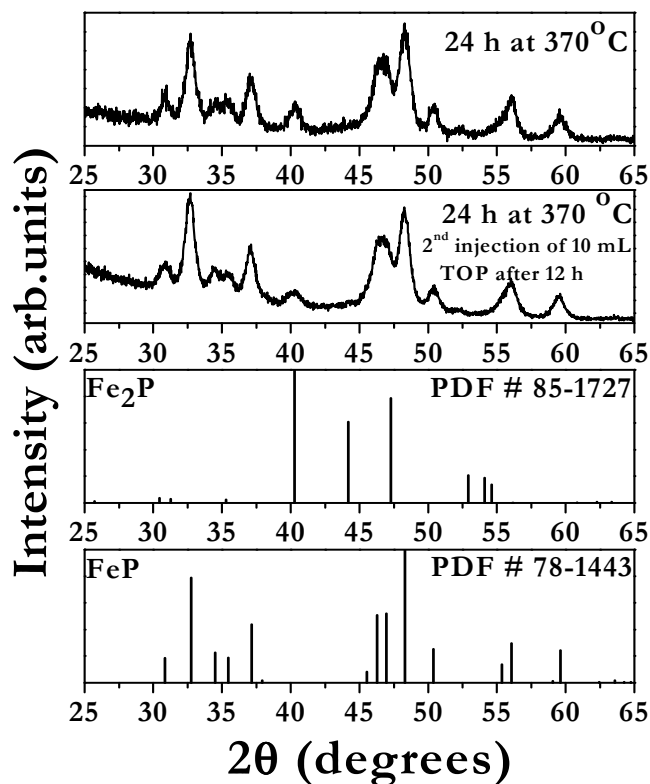
Figure 3.9 PXRD pattern depicting the effect of injection of additional TOP during a reaction carried out at 370 °C. Reproduced with permission from reference[86]. Copyright 2009 American Chemical Society.

3.3.2.6 Injection of Fe nanoparticles into preheated TOP: Reaction series VI

In all the reactions previously discussed, TOP at room temperature was injected into the Fe nanoparticle system at 200 °C and the temperature was ramped up to target. Although longer reaction times yielded FeP as the dominant product, phase-pure FeP remained elusive. Gradual availability of active phosphorus required for conversion in the synthesis might enable particle growth simultaneously with the transformation of intermediary Fe_2P to FeP. The larger the nanoparticle, the larger the kinetic barrier to

diffusion and therefore the transformation to FeP. Alternatively (or concomitantly) a protective layer of FeP may form on the outside of Fe_2P, preventing complete conversion. In an attempt to circumvent these potential effects, it was decided to introduce the iron nanoparticles at the reaction temperature, ensuring that the reaction was conducted entirely under conditions thermodynamically favorable for FeP formation. To achieve this, a variation in the synthesis scheme was introduced wherein Fe nanoparticles at 200 °C were cannulated into pre-heated TOP (Scheme 1, PATH-B). A series of reactions were carried out by this cannulation method at 350 °C and the isolated products were analyzed by PXRD and evaluated as a function of heating time. The PXRD patterns (Figure 3.10) clearly reveal the formation of a phase-pure product (FeP) within 24 h (i.e., Fe_2P was not detected). The PXRD patterns of the 1 h and 2 h samples have a clear peak at 40.2° (2θ), characteristic of Fe_2P, but patterns of the 3 h, 12 h and 24 h samples suggest residual Fe_2P might be absent.

Clear changes in particle morphology mirror the changes in the PXRD patterns, as shown in Figure 3.11. At very short times (1 h) after cannulation conversion to phosphides presumably takes place by a topotactic mechanism, resulting in near spherical particles and very short rods. Increased heating times result in rod formation (2 h) and further heating (3 h, 12 h) result in the shortening of the nanorods. In particular, the 3 h sample was found to consist of near spherical particles with an average size of 16.5 nm and rods whose length and width ranged from 40-80 nm and 12-18 nm, respectively. HRTEM reveals lattice fringes with spacing of 2.326 Å, corresponding to the (201) planes of FeP. Prolonged heating (24 h) resulted in the disappearance of the nanorods and the system was completely made up of near spherical particles. These all exhibited

spherical hollows, indicative of the Kirkendall effect. Despite prior reports of FeP nanorods in the literature,[50, 52] under the conditions employed here, the dominant morphology is clearly spherical. Based on these data, it appears that the transformation of spherical Fe nanoparticles to hollow spheres of FeP may occur *via* multiple pathways, including direct (topotactic) transformation as well as proceeding *via* Fe_2P as an intermediary phase that adopts an anisotropic morphology. As Fe_2P transforms to FeP, the Fe_2P rods become shorter, ultimately becoming spherical.
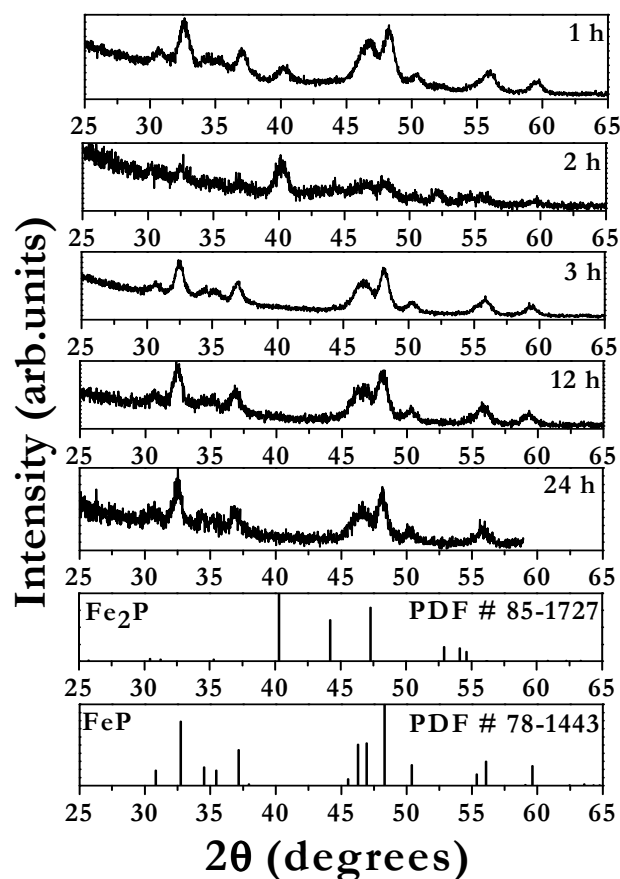
Figure 3.10 PXRD patterns of the products from PATH-B (Scheme 3.1) as a function of time at 350 °C. Reproduced with permission from reference[86]. Copyright 2009 American Chemical Society.
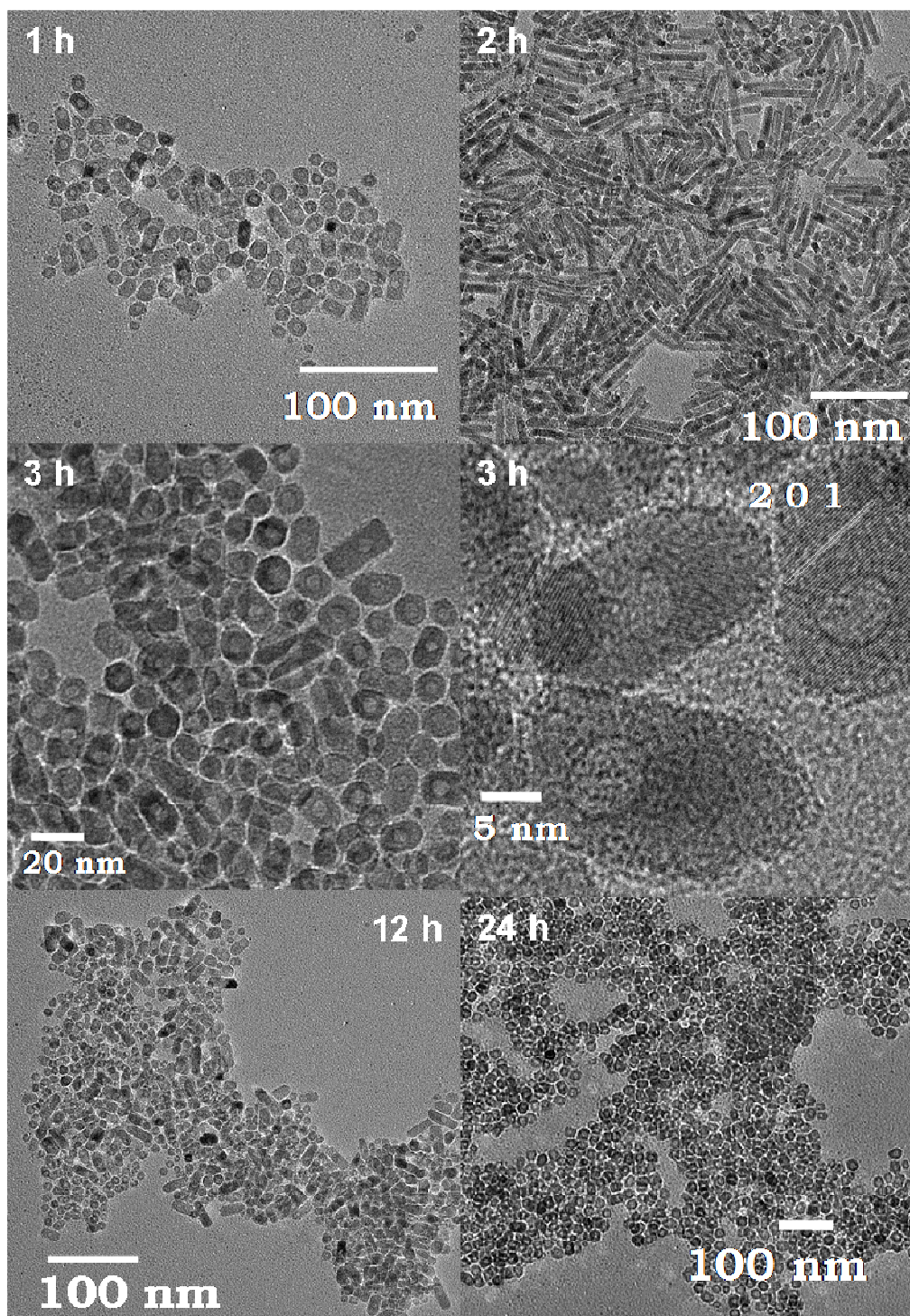
Figure 3.11 Effect of heating time (350 °C) on the morphology of the product generated

by PATH-B (Scheme 3.1). Reproduced with permission from reference[86]. Copyright

2009 American Chemical Society.

Even though, the PXRD data indicated phase-pure FeP formation, the presence of ferromagnetic impurities, possibly residual Fe_2P in 3 h and 12 h samples, was suggested by magnetic susceptibility results (Figure 3.12a, b). Both curves exhibit an increase in susceptibility below 250K and have estimated T_b values of 213 K (3 h) and 179 K (12 h). This ferromagnetic response is unexpected because FeP itself is a metamagnet with no net ferromagnetic moment and a Néel temperature (T_N) of 115 K. In order to clarify the nature of the putative impurity phase, the magnetizations were measured as a function of temperature at a higher field, 2 Tesla. This exceeds the saturation field for Fe_2P, which results in complete saturation of any ferromagnetic moments arising from this impurity phase. A plot of inverse susceptibility against temperature (Figures 3.12c, d) gives information about the nature of the interactions in the sample. The positive Weiss constant fit for both samples at high temperatures confirms the presence of ferromagnetic interactions in the nanoparticles. Based on the similarity of Figure 3.12a and 3.12b to Figure 3.6a, we think it is likely that the magnetic response is due to untransformed Fe_2P. Comparing the low temperature FC magnetizations in Figures 3.6a and 3.12a, we estimate that the possible Fe_2P impurity phase represents no more than 5% of the total mass, which may explain why it is difficult to observe in routine PXRD. Moreover, the blocking temperature of the 3 h sample (213 K) is higher than that of the 12 h sample (179 K) suggesting larger ferromagnetic particles in the former case. If the mechanism of conversion involves $Fe \rightarrow Fe_2P \rightarrow FeP$, the effective particle size of Fe_2P should decrease during conversion, resulting in a lower blocking temperature for the 12 h sample, as we have observed here.
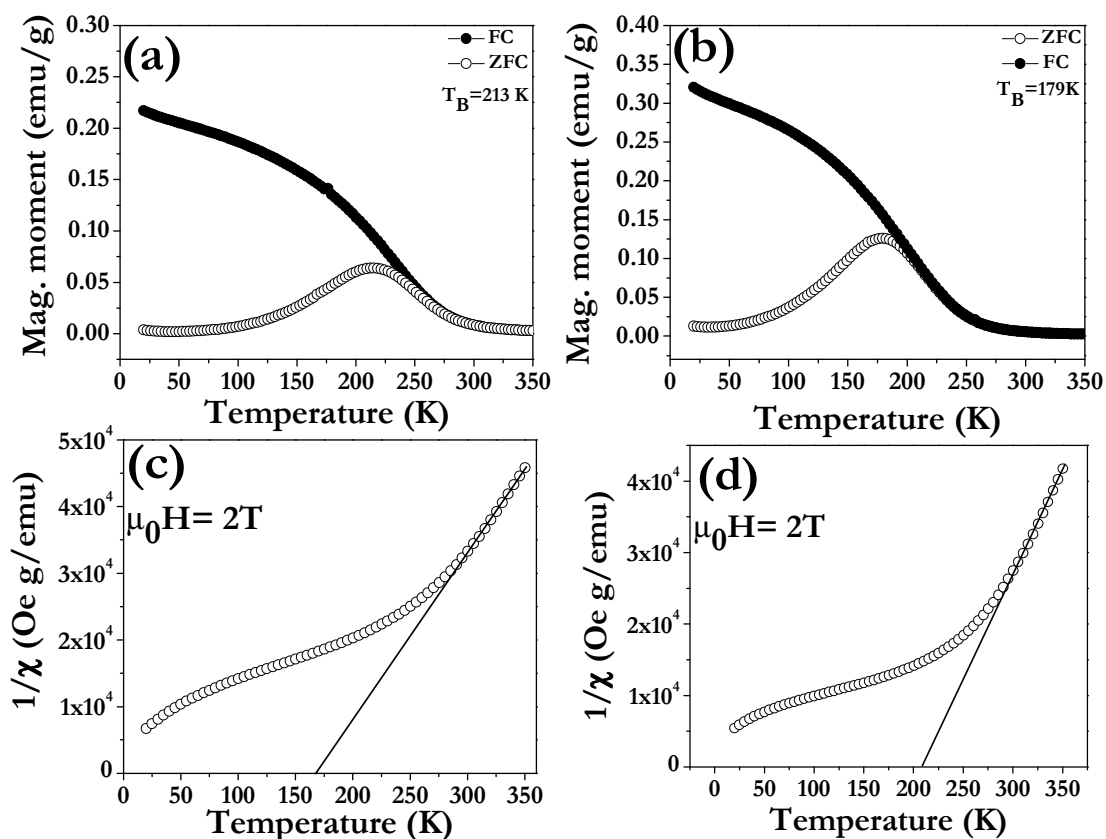
Figure 3.12 ZFC/FC curves of Fe$_x$P nanoparticles prepared by PATH-B (Scheme 3.1), measured at H = 100 Oe, for (a) 3 h sample (b) 12 h sample. Inverse susceptibility *vs.* temperature plots for (c) 3 h sample (d) 12 h sample indicating the presence of a ferromagnetic component. The straight line in (c) and (d) indicates the extrapolation of the high temperature inverse susceptibility used to estimate the Weiss interaction temperature. Reproduced with permission from reference[86]. Copyright 2009 American Chemical Society.

3.3.2.7 Generation of phase-pure FeP nanoparticles and magnetic properties

To ensure phase-pure samples for magnetic susceptibility analysis, the cannulation reaction (PATH-B, Scheme 3.1) was conducted for 24 h at a higher temperature, 370 °C. As shown in Figure 3.13a, the PXRD pattern reveals no discernible impurities, and the particles are uniformly spherical (14.9 ± 1.2 nm) with hollow structures according to TEM (Figure 3.13b, c). EDS data obtained on the FeP nanoparticles is also in line with expected values for FeP (Figure 3.13d). The slightly higher than expected value quantified for phosphorus is expected due to the presence of TOP on the particle surface.
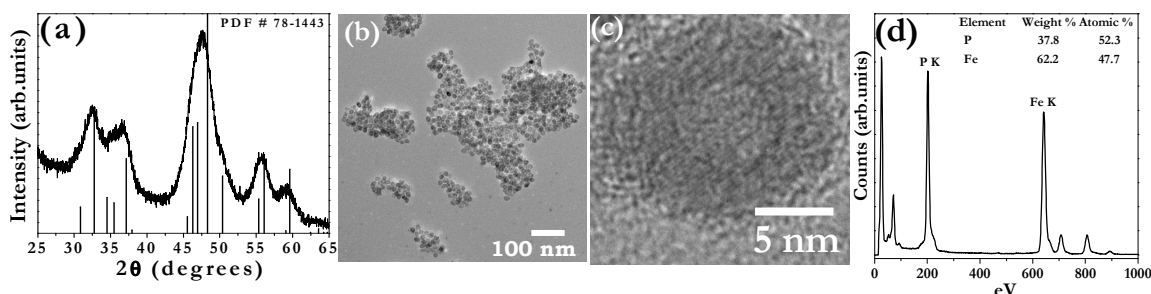
Figure 3.13 (a) PXRD pattern of a phase-pure FeP nanoparticle sample prepared by optimizing the synthetic conditions in PATH-B (Scheme 3.1) compared to the FeP reference pattern, (b) TEM image of the near spherical FeP nanoparticles, (c) HRTEM image indicating presence of hollow structure in FeP nanoparticles and (d) EDS data obtained on the FeP nanoparticles. Reproduced with permission from reference[86]. Copyright 2009 American Chemical Society.

Magnetic measurements conducted at 2T (Figure 3.14a) are consistent with a paramagnetic response from 350 to 125 K, with a larger rate of increase in the magnetization at temperatures below 125 K. While there is some curvature in the inverse

susceptibility plotted against temperature, a linear extrapolation of the high temperature portion of the $1/\chi$ vs T data (Figure 3.14b) yields a negative Weiss constant of -300 K, suggesting the presence of antiferromagnetic interactions. Although there is no clear magnetic anomaly in these data to indicate the onset of antiferromagnetic order in the FeP nanoparticles, the increase in magnetization above the paramagnetic contribution at low temperature can be attributed to an incomplete cancellation of the antiferromagnetic spins in these nanoparticles. The T_N for the system was estimated from the intersection of the two slopes extrapolated to the temperature axis (Figure 3.14b). Based on this analysis, the approximate value of T_N for the FeP nanoparticles was 120 K, which is close to the reported value for bulk FeP (115 K).[90] The absence of ferromagnetic contributions is consistent with earlier reports on 5 nm FeP nanoparticles[46] and FeP nanowires.[52] It can thus be concluded that the prior reports of ferromagnetism in FeP[50, 72] may reflect the presence of a secondary phase in these samples, such as Fe, iron oxides, or Fe_2P.

The magnetic data suggests that much stronger interactions are present in the 15 nm hollow nanoparticles presented here than the interaction observed for 5 nm solid spherical FeP nanoparticles reported previously from our laboratory. For the 5 nm spherical FeP nanoparticles, the deviation from linearity in the $1/\chi$ vs T plot was much weaker and occurs near 75 K, well below the reported bulk T_N. Additionally, the Weiss constant is much smaller (-20 K).[46] The difference is likely a function of the particle size. The helimagnetic structure of FeP has a repeat distance of nearly 3 nm and there may be a critical particle volume needed to achieve long-range order.
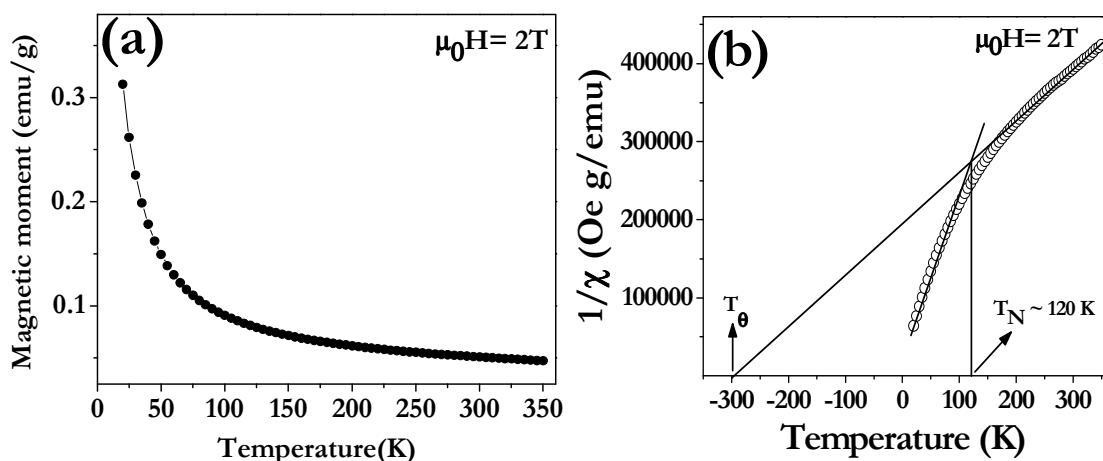
Figure 3.14 (a) Magnetization *vs.* temperature measurements of phase-pure FeP measured in a field of 2 Tesla and (b) The corresponding $1/\chi$ vs T plot. Reproduced with permission from reference[86]. Copyright 2009 American Chemical Society.

3.4 Conclusion

The selection of phase (FeP or Fe_2P) in the transformation of Fe nanoparticles to iron phosphides by high temperature treatment with TOP was found to be a sensitive function of heating time, temperature, reaction concentration, and even order of reagent addition. In all cases, Fe_2P formed at short reaction times and adopted a rod morphology, occasionally with hollows characteristic of the Kirkendall effect. Moreover, sufficiently high concentrations of Fe enable production of phase-pure Fe_2P. At suitably long times and high temperatures, Fe_2P transformed to FeP and adopted a spherical morphology (again with hollows); however, driving this reaction to completion was challenging, suggesting some kind of kinetic barrier. We speculate that FeP formation by conversion from Fe_2P was often incomplete due to decreased ion mobility from the core as the FeP shell thickness increases. This was alleviated by rapid reaction of iron and TOP at temperatures that thermodynamically favor FeP, perhaps due to some degree of topotactic

transformation of Fe to FeP in addition to the Fe_2P to FeP transformation. It should be noted that the transformations of Fe to Fe_2P or Fe_2P to FeP do not appear to be topotactic and are accompanied by a drastic change in morphology (sphere to rod, rod back to sphere). Importantly, when care was taken to prepare phase-pure FeP and Fe_2P, the magnetic properties observed are in line with expectations arising from the behavior of bulk phases. On the basis of this study, prior reports of unexpected magnetic behavior in FeP and Fe_2P nanoparticles[48, 50, 67, 72] can potentially be attributed to ferromagnetic impurities, which can be expected to dominate the response, even when present in small (not detectible by PXRD) quantities.

CHAPTER 4

NICKEL PHOSPHIDE NANOPARTICLES: SIMULTANEOUS CONTROL OF PHASE, SIZE AND MORPHOLOGY

4.1 Introduction

Similar to iron phosphides, nickel phosphides also exist in a wide range of stoichiometries.[73] In particular, Ni_2P has received a considerable interest for their hydrotreating catalytic properties in the processing of fuels.[31, 36-37] A variety of methods have been reported for the preparation on the nanoscale Ni_2P but many of the reported methods suffer from generation of competing phases and/or lack of size and morphology control, underscoring a significant need for synthetic levers that enable these characteristics to be controlled. Solution based strategies that involve reaction of salts or organometallic reagents with phosphines have a high potential to enable control of size and morphology (hollow *vs.* solid) in addition to phase – all relevant parameters for catalytic properties.[50, 54-55, 58] We expect that the concepts we have learned on controlling phase in the Fe-P system can be successfully extended to the Ni-P system to generate phase pure samples and enable access to different compositions.[86]

This chapter discusses in detail the identification of the synthetic levers that play an important role in controlling phase ($Ni_{12}P_5$ *vs.* Ni_2P), size and morphology (solid *vs.* hollow) in the nickel phosphide system. The investigation resulted in optimal conditions for the selective preparation of $Ni_{12}P_5$ and Ni_2P in a range of sizes (10-27 nm) either as dense spheres or hollow structures in addition to the capability to carry out transformations ($Ni_{12}P_5$ to Ni_2P) with conservation of morphology.

4.2 Experimental Section

All chemicals used for the syntheses related to this chapter on nickel phosphide nanoparticles are listed in Section 2.1 of Chapter 2.

4.2.1 Synthesis of Nickel Phosphide Nanoparticles

All reactions were carried out according to Scheme 4.1 under an argon atmosphere using standard Schlenk line techniques. Two different approaches were followed to prepare nickel phosphide nanoparticles: (i) a one-pot strategy involving both Ni and P precursors in the synthesis of precursor nanoparticles at 230 °C and subsequent conversion to phosphide phase at 300-350 °C; and (ii) a two-pot strategy where the precursor nanoparticles are isolated, then subsequently re-dispersed in octylether and oleylamine and reacted with TOP at 350 °C.
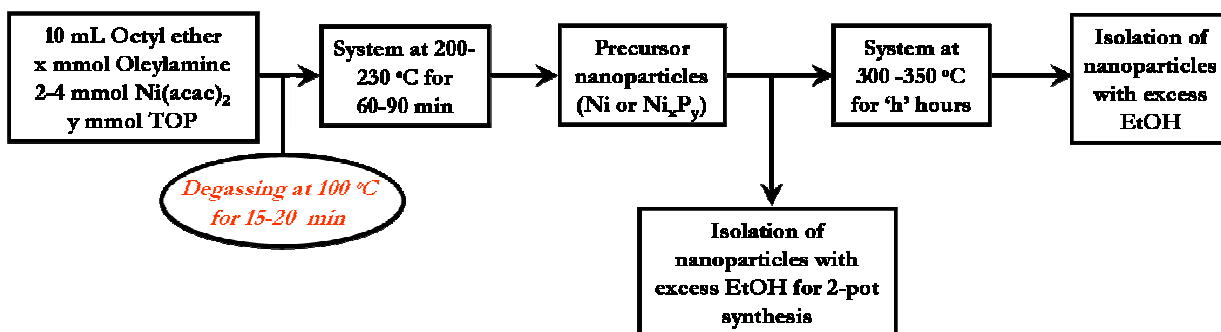
Scheme 4.1: Reaction pathway indicating the nanoscale preparation of Ni-P nanoparticles.

In a typical one-pot synthesis, both Ni and P precursors are combined along with 10.0 mL octyl ether (solvent) and 2.0-4.0 mL oleylamine (surfactant) and degassed at 100

°C under partial vacuum conditions. The system was raised to 230 °C under Ar, where it was maintained for about 60-90 minutes yielding a black solution. The system color changes to black from bluish green within a few minutes (10-15), indicating the formation of the precursor nanoparticles. In the next step, the system was raised to higher temperature to initiate the formation of a crystalline phosphide phase. The heating conditions (temperature and reaction time) were varied from 300-350 °C and 1-3 h, depending on the phase desired. The nanoparticles were isolated after returning the system to room temperature (RT). Isolation was achieved by centrifugation after addition of excess ethanol (20-30 mL). Isolated nanoparticles were then dispersed in a small quantity of chloroform (2-3 mL) with sonication and re-precipitated with excess ethanol. The process was repeated 2 times and the washed product was dried under vacuum to yield a free flowing powder. In some experiments, TOP was not combined with the nickel precursor but was injected into the precursor nanoparticle system just before raising the temperature to initiate the formation and crystallization of the phosphide phase. Reactions were also carried out in which the oleylamine:Ni ratio was varied from 3.0 to 22.0, by varying the oleylamine quantity and keeping other reaction parameters constant in order to determine the effect of oleylamine concentration on the phase of the final product.

In the two-pot strategy, precursor nanoparticles are synthesized as described above and are isolated after the reaction at 230 °C (Scheme 4.1). The isolation is carried out in a similar manner described previously for the one-pot synthesis of nickel phosphide nanoparticles. Subsequently, a known quantity (50-100 mg) of the isolated nanoparticles were combined with 10.0 mL octyl ether and 2.0 mL oleylamine. The

system was degassed under vacuum at 100 °C and was raised to 300 °C under argon. After 10-15 minutes at 300 °C, 10.0 mL TOP was injected into the system, followed by an increase in temperature to 300-350 °C, where it was maintained for 3-4 h. Isolation of the final product was carried out as detailed for the one-pot synthesis.

In the case of topotactic transformation reactions, a known quantity of hollow/solid $Ni_{12}P_5$ was combined with octyl ether (10.0 mL) and oleylamine (2.0 mL) and was raised to 300 °C under argon. After 15 minutes at 300 °C, 15.0 mL TOP was injected into the system and the reaction was carried out at 350 °C for 4 h. Isolation of the final product was carried out as described previously for the one-pot synthesis.

4.3 Results and Discussion

4.3.1 Phase Control (Ni_2P *vs.* $Ni_{12}P_5$)

Ni_2P[50, 54-55, 58] and $Ni_{12}P_5$[35, 51, 59, 91] are the most commonly observed phases in preparations of nanoscale nickel phosphides. A P:Ni precursor ratio of 1.12 (4 mmol $Ni(acac)_2$ and 2.0 mL TOP) with 3 equivalents of oleylamine relative to Ni and a reaction temperature of 300 °C for 1 h provided optimal conditions for generating phase-pure $Ni_{12}P_5$, as shown from the PXRD pattern in Figure 4.1a. In order to stabilize a more P-rich phase, keeping other conditions constant, the conversion reaction was carried out for a longer time (3 h) at a higher temperature (350 °C) with an increased P:Ni precursor ratio of 5.6 (2 mmol $Ni(acac)_2$ and 5.0 mL TOP). The final product as analyzed by PXRD was found to be a perfect match for the more P-rich phase, Ni_2P (Figure 4.1b). These observations highlight the successful extension of the phase control strategy, first developed by us for the Fe-P system (Chapter 3).[86]
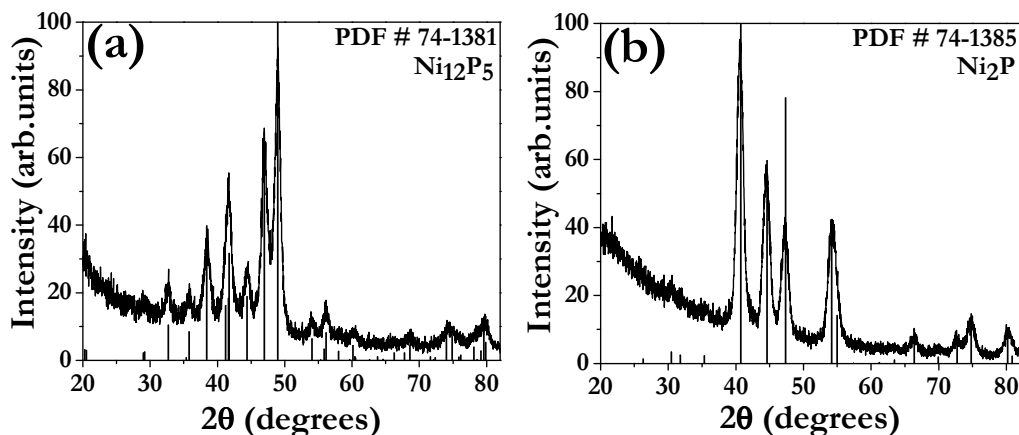
Figure 4.1. PXRD patterns of (a) $Ni_{12}P_5$ nanoparticles and (b) Ni_2P nanoparticles compared to their corresponding reference patterns.

TEM analyses of Ni_2P nanoparticles corresponding to the PXRD pattern in Figure 4.1b, revealed that the sample was completely composed of solid nanoparticles (Figure 4.2a). The particles were observed to have a spherical morphology with an average size of 10.2 ± 0.9 nm (Figure 4.2b). The P:Ni atomic percent composition obtained from the EDS data was slightly higher than the expected value for the Ni_2P phase (Figure 4.2c). The high content of P can be attributed to residual TOP ligands bound to the surface of the Ni_2P nanoparticles.[58]

In contrast, TEM of $Ni_{12}P_5$ nanoparticles corresponding to the PXRD pattern in Figure 4.1a under TEM indicated the formation of hollow nanostructures (Figure 4.3a). The average size of the nearly spherical hollow nanoparticles was calculated to be 26.8 ± 1.9 nm (Figure 4.3b). EDS data obtained on the as prepared nanoparticles was consistent with the expected value for the $Ni_{12}P_5$ phase (Figure 4.3c). To the best of our knowledge, this was the first observation of high quality, phase-pure hollow $Ni_{12}P_5$ nanoparticles.

The hollow structures were similar to the ones reported for Ni_2P by Chiang and coworkers[55] and Schaak and co-workers.[54] Hollow void formation is attributed to the well known nanoscale Kirkendall effect.[56] The void formation is caused due to the difference in diffusion rates of Ni ions (outward) and P ions (inward). During the transformation of a metal nanoparticle into an alloy, mass transfer occurs through vacancy exchange resulting in the formation of a void by coalescence of the vacancies present in the metal nanoparticle.[56] The phenomenon has been widely observed in the transformation of metal nanoparticles into their corresponding chalcogenides,[56] oxides[92] and phosphides.[51, 53-55]

These observations clearly indicate that careful choice of reaction conditions can not only enable control of the phase of the nanoparticles but their morphology as well. Moreover, the change in P:Ni precursor ratio also had an effect in the size of hollow $Ni_{12}P_5$ and solid Ni_2P nanoparticles. Increasing the P:Ni precursor ratio from 1.12 to 5.6 resulted in a decrease in average size of the nanoparticles from 26.8 ± 1.9 nm to 10.2 ± 0.9 nm. The decrease in size of nanoparticles with increasing TOP:oleylamine ratio in the system is consistent with previous observations made by Mèzailles and coworkers in their work on Ni nanoparticles and is attributed to the stabilization of the nanoparticle surface by TOP.[93]
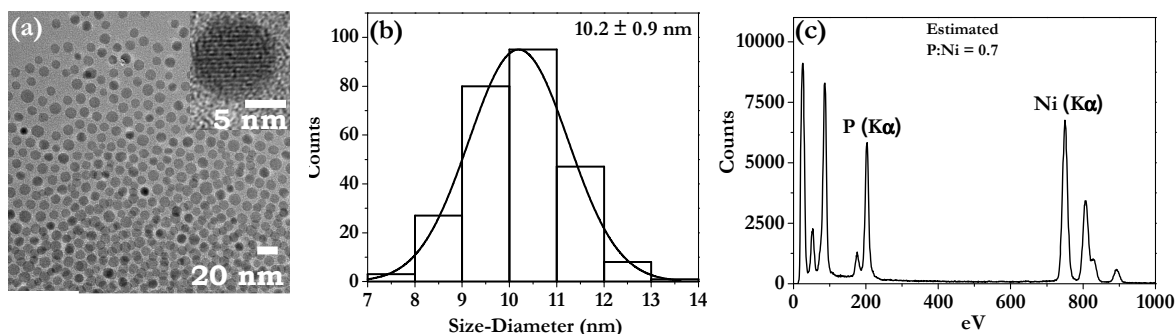
Figure 4.2. (a) TEM image of Ni_2P indicating solid structures (inset: HRTEM indicating lattice fringes and absence of hollow structure), (b) Histogram and (c) EDS pattern. Expected P:Ni ratio for Ni_2P is 0.5.
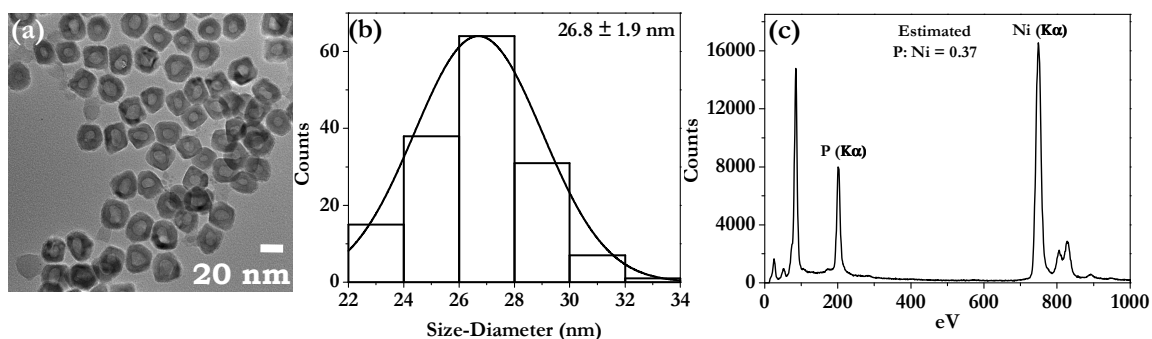
Figure 4.3. (a) TEM image of $Ni_{12}P_5$ indicating hollow structures, (b) Histogram and (c) EDS pattern. Expected P:Ni ratio for $Ni_{12}P_5$ is 0.42.

The variation in morphology between $Ni_{12}P_5$ and Ni_2P (hollow *vs.* solid) can be attributed to the choice of precursor ratios chosen to stabilize these two different phases. These observations fall in line with the recent report on morphology control in Ni_xP_y nanoparticles by Tracy and coworkers.[51] According to Tracy and co-workers, P:Ni ratios in the range of 1-3 result in the formation of hollow crystalline Ni_xP_y nanoparticles while ratios greater than 9.0 result in solid crystalline Ni_xP_y nanoparticles. Intermediate ratios

were observed to result in both morphologies. Tracy and coworkers observed that the P:Ni precursor ratios played a role in determining the nature of the species formed at the precursor stage (220 °C). Low P:Ni precursor ratios (1-3) resulted in the formation of crystalline Ni and high P:Ni precursor ratios (>9) resulted in the formation Ni-P alloy at the precursor stage (220 °C), which on subsequent heating was found to transform into crystalline Ni_xP_y with hollow and solid morphologies, respectively. However, their samples were characterized to be mixtures of both $Ni_{12}P_5$ and Ni_2P.

4.3.2 Effect of P:Ni Ratio on Precursor Crystallization and Composition

The hypothesis on hollow and solid Ni_xP_y nanoparticle formation postulated by Tracy and coworkers[51] was tested under our synthetic conditions. The nature of the precursor nanoparticles formed at 230 °C was investigated as a function of the P:Ni precursor ratio and the as-prepared nanoparticles were subsequently heated at 350 °C with excess TOP to evaluate the morphology of the final product (Section 4.3.3).

Precursor nanoparticles were prepared with varying P:Ni ratios in the range 0.28 to 5.6. The precursor nanoparticles were aged at 230 °C for 60-90 minutes and were isolated at RT by centrifugation with excess ethanol. The isolated precursor nanoparticles were characterized by PXRD, TEM and EDS. The PXRD pattern of precursor nanoparticles prepared with a ratio of 0.28 was observed to match with the reference pattern of fcc-Ni (Figure 4.4). All three peaks corresponding to cubic phase Ni were observed. In addition, the nanoparticles were observed to respond strongly to a magnetic stir bar, indicating the superparamagnetic nature of the as prepared Ni nanoparticles. A similar PXRD pattern was obtained for precursor nanoparticles prepared with P:Ni ratios of 0.56, 1.12 and 1.68 (Figure 4.4). The nanoparticles were again observed to respond

strongly to magnetic stir bar. TEM analyses of the precursor nanoparticles prepared with P:Ni ratios of 0.28 and 1.12 indicate that the particles are nearly spherical and monodisperse with an average size of 27.2 ± 2.4 nm and 21.1 ± 1.4 nm respectively (Figure 4.5 a, b). EDS data are also consistent with Ni formation with just a small signal for P attributed to the TOP ligands binding to the surface of Ni nanoparticles(Figure 4.5 a, b).[58]
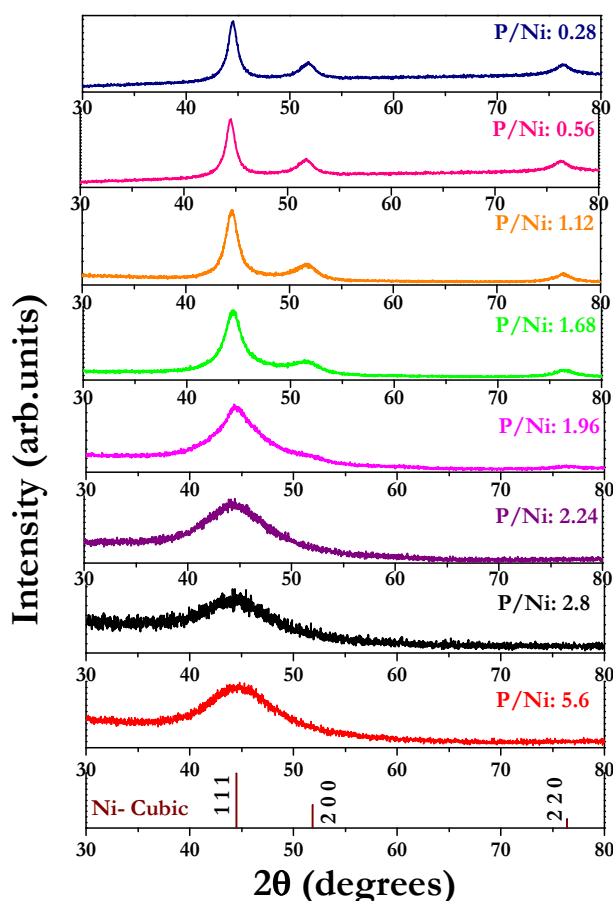
Figure 4.4. PXRD patterns of precursor nanoparticles prepared at 200-230 °C with varying P:Ni precursor ratios compared to the Ni reference pattern (PDF # 87-0712).

When the P:Ni ratio was increased to 2.24 or higher, the PXRD patterns of the precursor nanoparticles indicated that the product was less crystalline (Figure 4.4). A

broad peak around 44° (2θ) corresponding to the most intense peak of fcc-Ni phase was observed while the two other characteristic Ni peaks were absent, suggesting a lower crystallinity of the sample. The samples did not respond to a magnetic stir bar, indicating a transition from a magnetic to a non-magnetic phase. TEM images of the nanoparticles prepared with P:Ni precursor ratios of 2.8 and 5.6 reveal the formation of spherical nanoparticles with an average size of 10.4 ± 0.8 nm and 9.6 ± 1.1 nm, respectively (Figure 4.5c, d). P:Ni ratios obtained from EDS analysis for both nanoparticles were found to be comparatively higher than the crystalline Ni samples (Figure 4.5c, d). The high P content along with the broad feature in the PXRD pattern and unresponsiveness to an external magnet suggest the formation of an amorphous alloy of Ni-P. These results are qualitatively similar to those reported by Tracy and co-workers for P:Ni ratios >9, but we see the transition from crystalline Ni to amorphous Ni_xP_y at considerably smaller ratios of P:Ni under our synthetic conditions. The gradual decrease in the size of the nanoparticles with increasing P:Ni precursor ratio is consistent with our earlier observation (Section 4.3.1) and published work.[93] An intermediate P:Ni precursor ratio of 1.68 resulted in nanoparticles which exhibited all three peaks corresponding to a cubic-Ni phase in the PXRD pattern but the (111) reflection was found to be relatively broad in comparison to the (111) reflections of precursor nanoparticles prepared with lower P:Ni ratios. In addition, the sample was found to give a weak response to magnetic stir bar indicating that this composition is near the transition from magnetic Ni to non-magnetic Ni_xP_y nanoparticles. These data are summarized in Table 4.1.
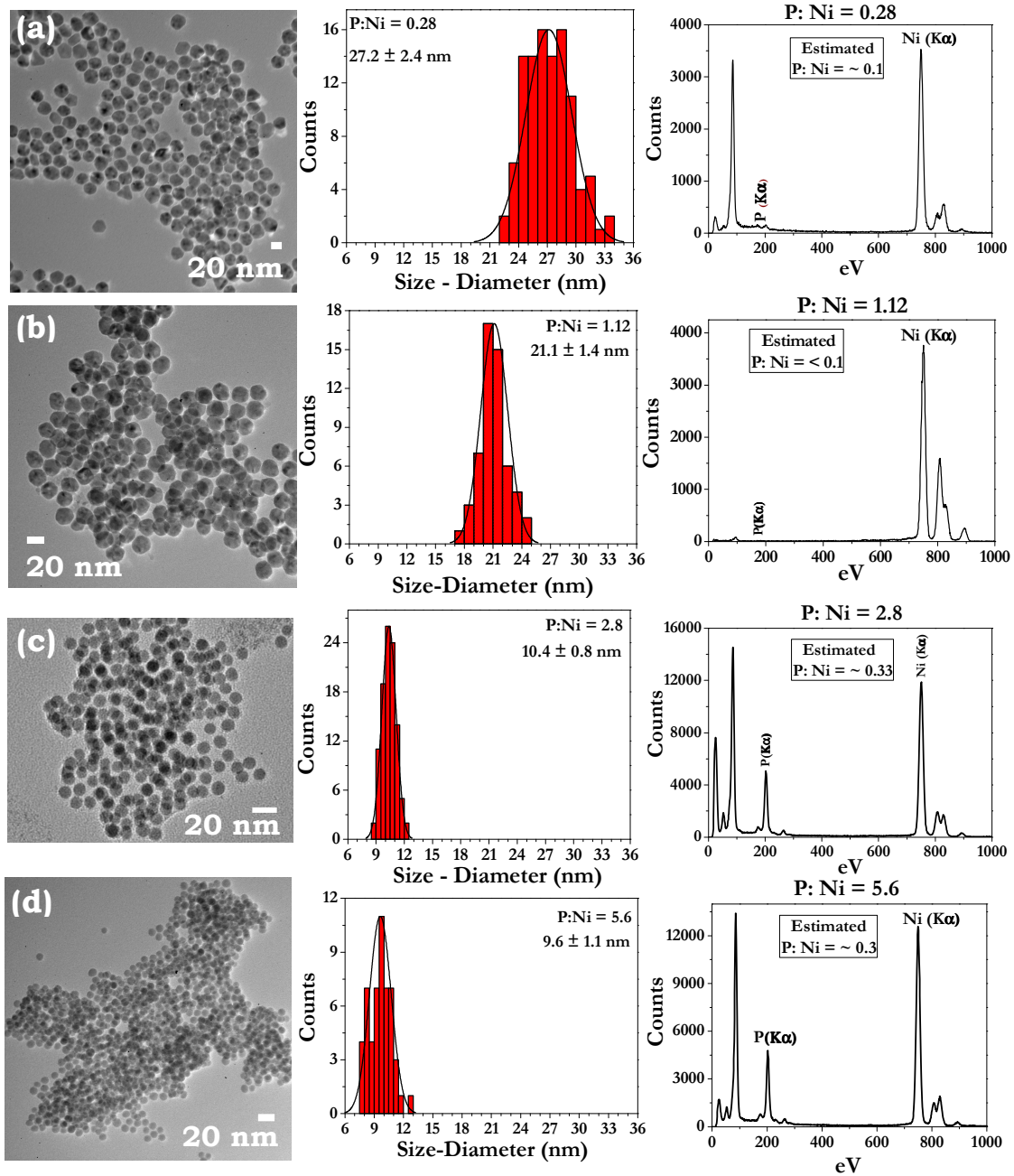
Figure 4.5. TEM images, histograms and EDS patterns of nanoparticles prepared at 200-230 °C with varying P:Ni precursor ratios. (a) 0.28; (b) 1.12; (c) 2.8 and (d) 5.6.

4.3.3 Transformation of Crystalline Ni and Amorphous Ni_xP_y Nanoparticles to Hollow and Dense Ni_2P, Nanoparticles

The generated precursor nanoparticles were then converted into crystalline Ni_2P by reaction with TOP in order to observe the effects of precursor composition on morphology. In order to favor Ni_2P over $Ni_{12}P_5$, we used a higher conversion temperature (350 °C) relative to Tracy and coworkers (300 °C) and simultaneously employed longer reaction times (3-4 h) and excess TOP. ~ 50 mg of each of the precursor nanoparticles in Figure 4.6 were combined with 10.0 mL octyl ether and 2.0 mL oleylamine and subsequently reacted with 11.2 mmol of TOP at 350 °C for 3-4 h to yield samples of Ni_2P. The isolated final products were then characterized by PXRD and the patterns indicate that all precursor nanoparticles were completely converted into crystalline phase-pure samples of Ni_2P (Figure 4.6). No magnetic response was observed in any of the samples, consistent with complete conversion to the phosphide phase. The PXRD patterns clearly indicate size differences between Ni_2P nanoparticles obtained from crystalline Ni nanoparticles and the amorphous Ni_xP_y nanoparticles. The peaks were all broader, and peaks corresponding to (002/300) and (211) reflections were found to merge together for the Ni_2P nanoparticles obtained from amorphous Ni_xP_y nanoparticles, whereas the reflections can be identified discretely for Ni_2P nanoparticles obtained from crystalline Ni nanoparticles. Crystallite size calculations made on (111) reflections of Ni_2P nanoparticles using the Scherrer equation substantiates the qualitative observations made from the PXRD patterns (Table 4.1). Ni_2P obtained from the crystalline Ni precursor nanoparticles were comparatively larger in size when compared to the products obtained from amorphous Ni_xP_y nanoparticles.

TEM analyses (Figure 4.7) of Ni_2P nanoparticles are in rough agreement with the size calculations in Table 4.1 but crystallite size calculations significantly underestimate sizes for hollow particles due to the presence of the void. Ni_2P nanoparticles obtained from crystalline Ni nanoparticles in Figure 4.5a (27.2 ± 2.4 nm) and 4.5b (21.1 ± 1.4 nm) were found to be composed of hollow structures with an average particle size of 31.6 ± 2.7 nm and 24.0 ± 2.4 nm, respectively (Figure 4.7a, b). The ca. 15% increase in size during transformation to Ni_2P is expected due to the incorporation of phosphorus and the formation of hollow voids within the particles. On the other hand, the Ni_2P nanoparticles obtained from amorphous Ni_xP_y nanoparticles in Figure 4.5c (10.4 ± 0.8 nm) and 4.5d (9.6 ± 1.1 nm) resulted in solid spherical nanoparticles of size of 11.0 ± 0.7 nm and 10.2 ± 1.0 respectively (Figure 4.7c, d). In contrast to the hollow structure formation, the size increase is considerably smaller (5-6%), as expected for a dense structure.
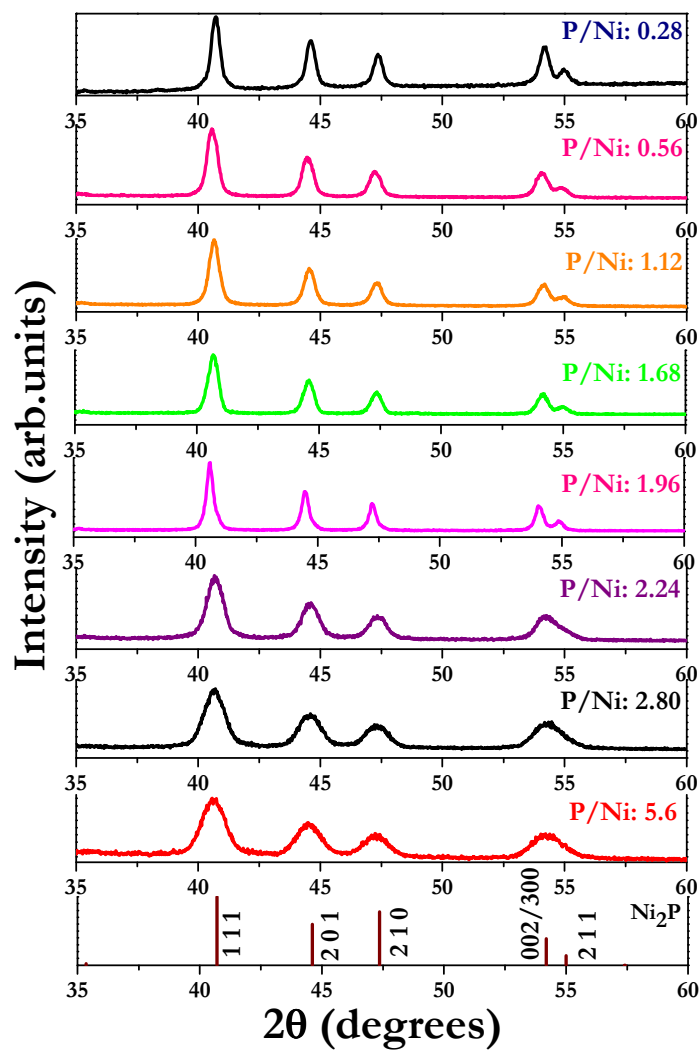
Figure 4.6. PXRD patterns of the final products obtained by the reaction of the various precursor nanoparticles from Figure 4.4 with TOP at 350 °C for 3-4 h compared to the Ni$_2$P reference pattern (PDF # 74-1385).

Table 4.1. Summary of the effect of precursor P:Ni ratio on precursor nanoparticle phase, size, magnetic response and product phase, crystallite size, and morphology/ particle size.

Precursor nanoparticles (P:Ni ratio)	Precursor nanoparticles (PXRD)	Precursor particle size (nm) TEM	Precursor nanoparticles (Magnetic response)	Product after conversion (PXRD)	Ni_2P crystallite size (nm) (PXRD)	Ni_2P particle size (nm) TEM
0.28	Crystalline Ni	27.2 ± 2.4	YES, Strong	Crystalline Ni_2P	23.0	31.6 ± 2.7 HOLLOW
0.56	Crystalline Ni	Not Available	YES, Strong	Crystalline Ni_2P	18.4	Not Available
1.12	Crystalline Ni	21.1 ± 1.4	YES, Strong	Crystalline Ni_2P	18.9	24.0 ± 2.4 HOLLOW
1.68	Crystalline Ni	Not Available	YES, Strong	Crystalline Ni_2P	18.1	Not Available
1.96	Crystalline Ni	Not Available	YES, Weak	Crystalline Ni_2P	27.1	Not Available
2.24	Amorphous Ni_xP_y	Not Available	NO	Crystalline Ni_2P	11.5	Not Available
2.80	Amorphous Ni_xP_y	10.4 ± 0.8	NO	Crystalline Ni_2P	8.9	11.0 ± 0.7 SOLID
5.60	Amorphous Ni_xP_y	9.6 ± 1.1	NO	Crystalline Ni_2P	7.9	10.2 ± 1.0 SOLID

These results clearly indicate that the morphology and size of the final product is dictated by the initial P:Ni precursor ratio chosen for a particular synthesis. Moreover, they show that conditions exist whereby a single phase product (Ni_2P) can be produced with hollow and solid morphologies. The Ni_2P phase was achieved by carrying out the conversion reactions for longer times (3-4 h) with excess TOP (compared to Ni) at higher temperatures (350 °C) which ensured adequate availability of reactive phosphorus for the formation of the more P-rich phase among accessible phases in this synthesis (Ni_2P over $Ni_{12}P_5$).
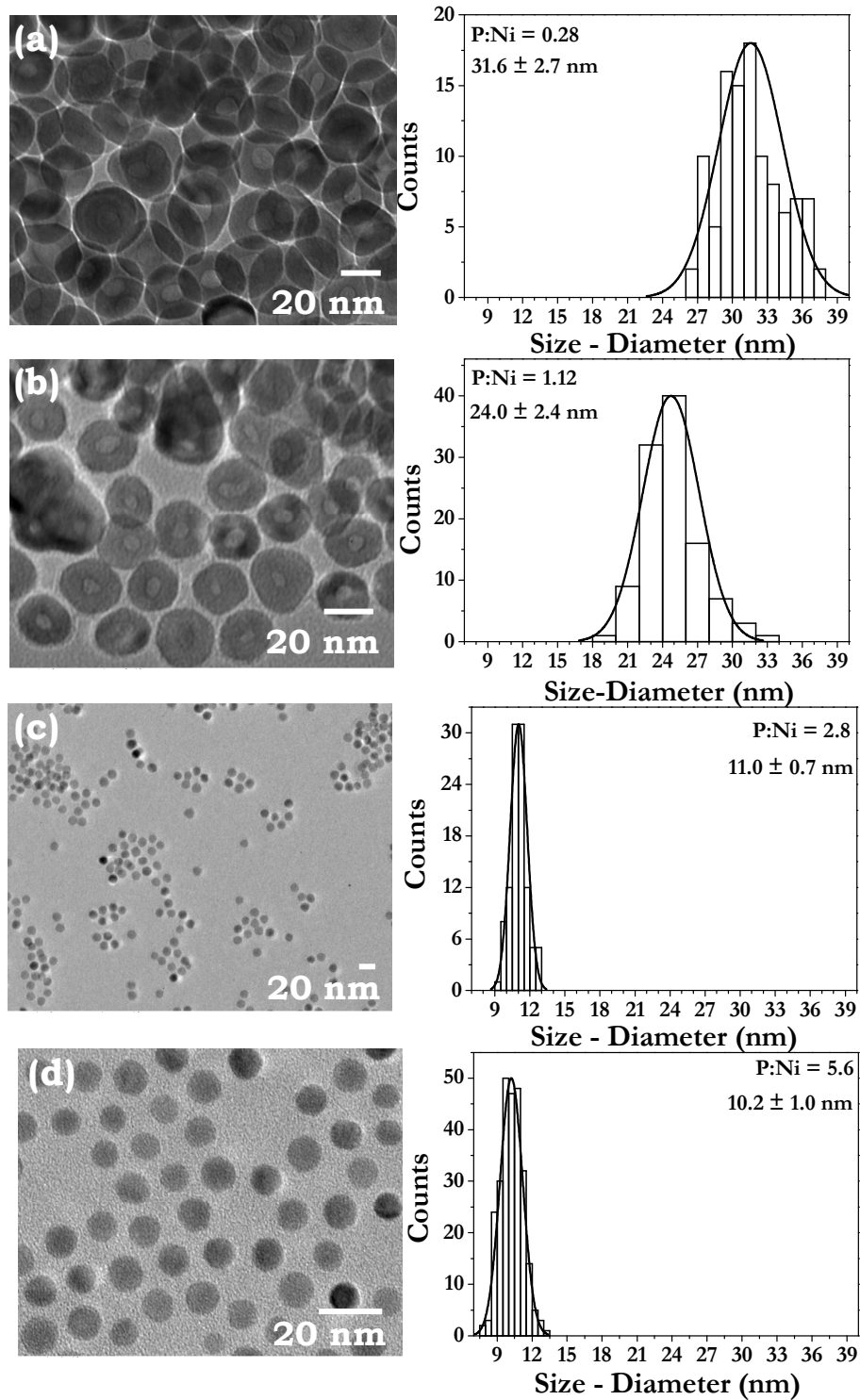
Figure 4.7. TEM images and histograms for Ni$_2$P nanoparticles obtained from different precursor nanoparticles prepared with varying P:Ni ratios: (a) 0.28; (b) 1.12; (c) 2.8 and (d) 5.6.

4.3.4 Effect of Oleylamine: Generation of Solid $Ni_{12}P_5$ Nanoparticles

The preparation of solid particles of $Ni_{12}P_5$ proved to be a complicated problem as a P:Ni precursor ratio of 2.8 or higher is needed to generate solid nanoparticles, but such high ratios favor formation of the more P-rich phase (Ni_2P) during conversion to the phosphide phase. In order to favor a more metal-rich phase, we explored the role of oleylamine as a reducing agent in the reaction.

Accordingly, a series of reactions was performed wherein the quantity of oleylamine was varied systematically while keeping all other reaction parameters constant. The ratio of oleylamine:Ni used in the reaction was varied from 3 to 22.5 and the PXRD patterns (Figure 4.8) of the isolated final products clearly indicated that higher amounts of oleylamine favors the formation of the metal-rich phase, $Ni_{12}P_5$. Specifically, the most intense peak corresponding to $Ni_{12}P_5$ was found to gradually grow with increasing oleylamine quantity and $Ni_{12}P_5$ was found to be the major product when the oleylamine:Ni ratio was 22.5. At this point the exact mechanism by which oleylamine tends to favor the metal-rich phase ($Ni_{12}P_5$) under conditions more suitable for the formation of Ni_2P is not known. However, oleylamine is purported to play the role of a reducing agent in metal nanoparticle syntheses[93] and thus the presence of excess amine could promote the stabilization of the more reduced phase ($Ni_{12}P_5$). A similar observation has been reported in the literature by Hyeon and coworkers wherein they observed the use of oleylamine favored the formation of metal-rich phase Fe_2P under conditions typically employed for FeP.[48]
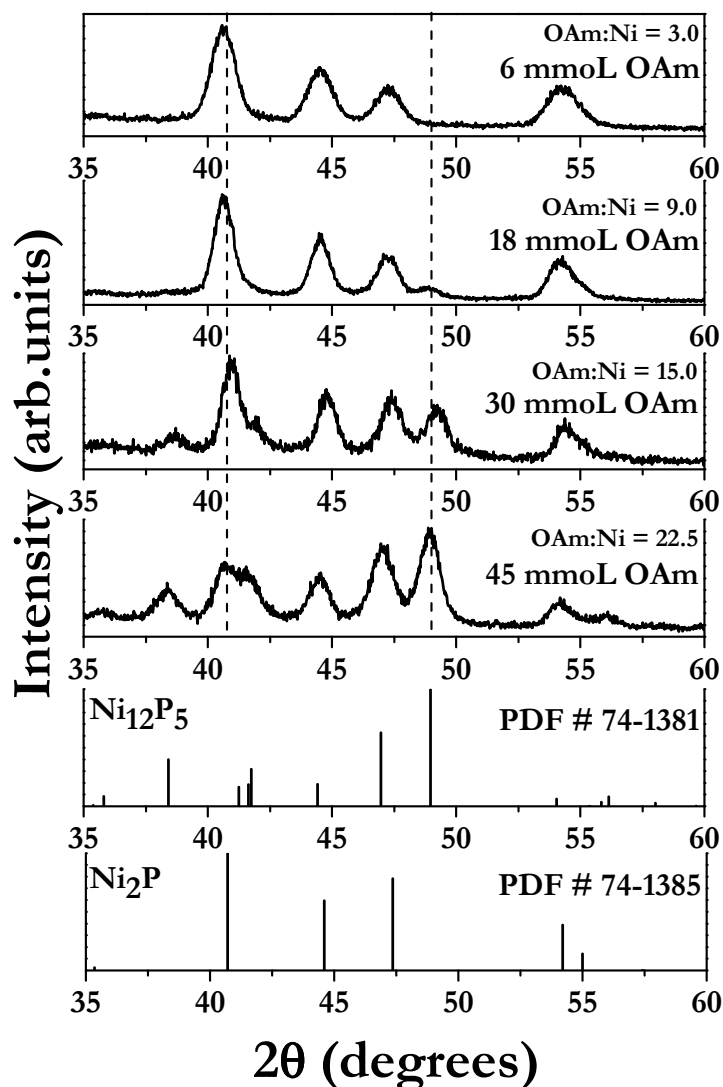
Figure 4.8. PXRD patterns of the final product prepared with varying oleylamine (OAm) quantity compared to the reference patterns for $Ni_{12}P_5$ and Ni_2P.

With this information in hand we attempted to make $Ni_{12}P_5$ with solid morphology by carrying out reactions with additional quantity of oleylamine. For the generation of $Ni_{12}P_5$ with solid morphology, the ratio of oleylamine:Ni was set at 15.0 (60 mmol oleylamine and 4 mmol $Ni(acac)_2$). A series of reactions was carried out at 350 °C for 1 h wherein the P:Ni precursor ratio was gradually varied from 1.12 to 5.6. As

expected, the addition of excess oleylamine was observed to stabilize the metal-rich phase $Ni_{12}P_5$ (Figure 4.9). All four samples were observed to be phase-pure $Ni_{12}P_5$ with no evidence of Ni_2P phase formation.
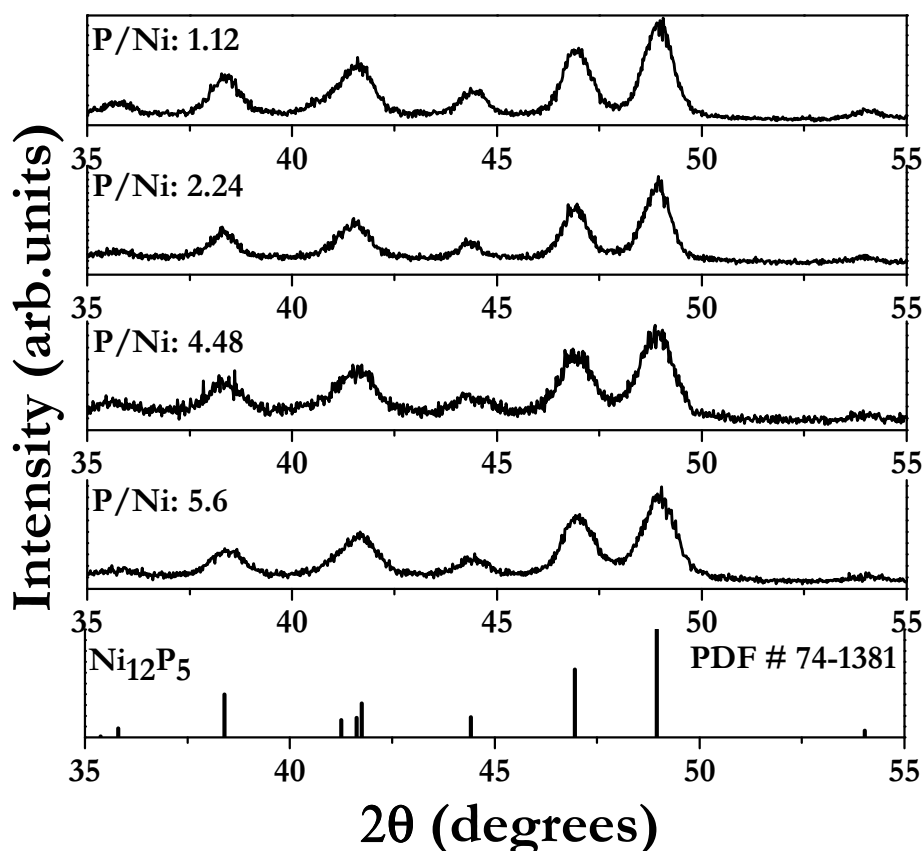
Figure 4.9. PXRD patterns of $Ni_{12}P_5$ nanoparticles prepared with varied P:Ni precursor ratios compared to the reference pattern (PDF # 74-1381).

TEM analyses of the $Ni_{12}P_5$ nanoparticles prepared with a P:Ni precursor ratio of 1.12 revealed formation of hollow nanoparticles (Figure 4.10a) with an average size of 25.3 ± 2.5 nm, as expected for this ratio. A gradual increase in P:Ni precursor ratio to 5.6 results in the transformation of hollow nanoparticles into solid spherical nanoparticles, while simultaneously resulting in smaller nanoparticles (Figure 4.10b, c, d) consistent

with the observation for Ni_2P. EDS analyses carried out on all nanoparticles are consistent with the stabilization of $Ni_{12}P_5$ phase. The ideal P:Ni atomic percent composition for $Ni_{12}P_5$ is 0.42, and the slight excess value observed can be attributed to the TOP ligands bound to the surface of the $Ni_{12}P_5$ nanoparticles.[58]
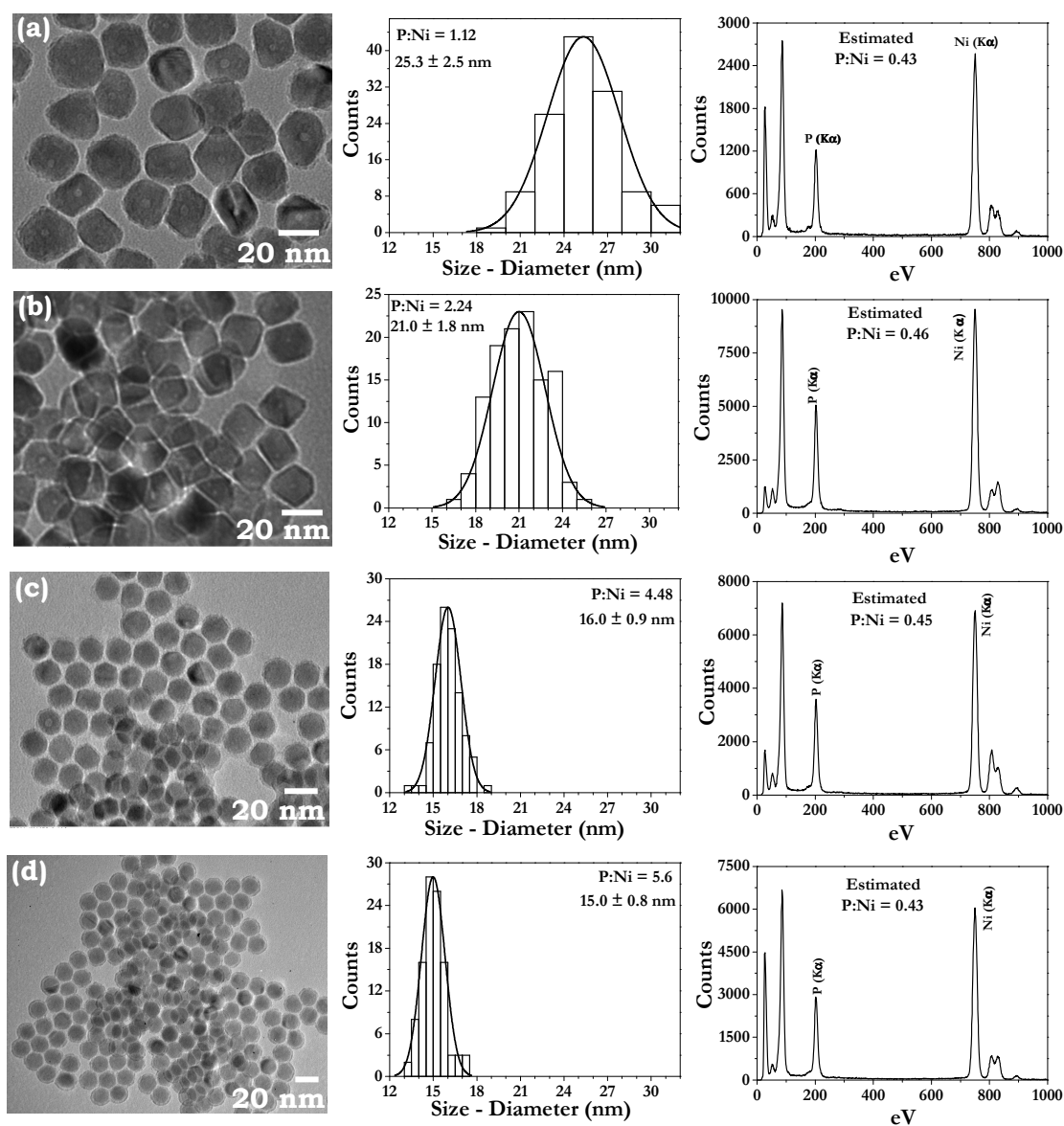
Figure 4.10. Characterization (TEM image, histogram and EDS pattern) of $Ni_{12}P_5$ nanoparticles prepared with varying P:Ni ratios: (a) 1.12, (b) 2.24, (c) 4.48 and (d) 5.60.

In order to prove that the excess amine addition is essential for the generation of solid $Ni_{12}P_5$, a set of control reactions (positive and negative) was carried out. The results of the reactions are given in Figure 4.11. When the reaction was carried out without the additional quantity of oleylamine, the product was characterized to be Ni_2P (Figure 4.11a). In order to discount the effect of dilution which occurs on addition of excess oleylamine, the system was diluted by an equivalent volume (16.0 mL) of octyl ether (non-coordinating solvent). The product of the reaction was again characterized to be Ni_2P (Figure 4.11b). In the last control reaction, the excess oleylamine was replaced by an equivalent quantity (in moles) by octadecylamine (Figure 4.11c). This time the product of the reaction was characterized to be $Ni_{12}P_5$. All the nanoparticles were observed to possess a solid morphology (Figure 4.11), as dictated by the P:Ni precursor ratio (5.6). These results confirm the requirement of excess amine to promote the stabilization of solid $Ni_{12}P_5$ nanoparticles.
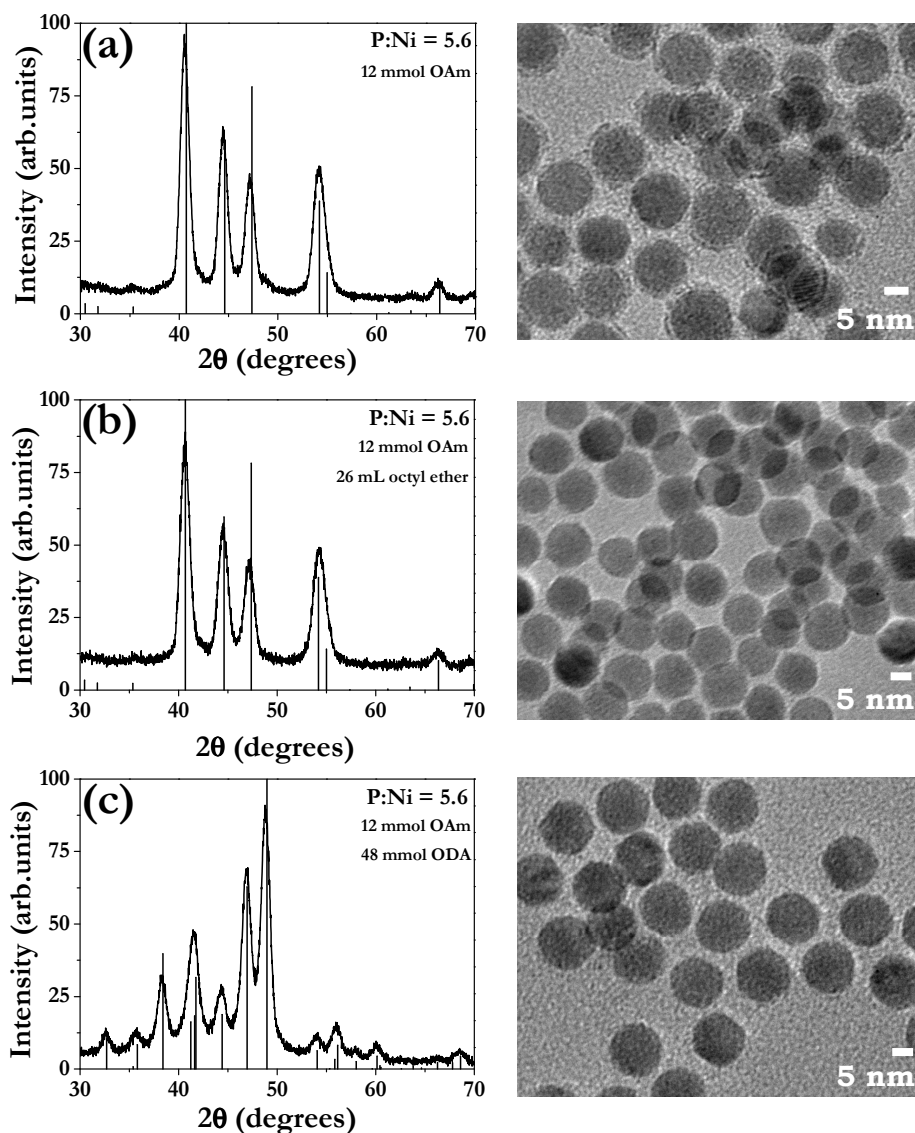
Figure 4.11. PXRD patterns and TEM images of the final product of the control reactions carried out to prove the effect of excess amine in the $Ni_{12}P_5$ solid nanosphere synthesis: (a) without excess oleylamine (OAm), (b) with excess octyl ether (solvent) and (c) with excess octadecylamine.

It should also be noted that the addition of excess oleylamine has also resulted in the reduction in size of the hollow structures. A size comparison made between the hollow structures of $Ni_{12}P_5$ nanoparticles prepared with different oleylamine quantities

indicates that higher oleylamine quantities results in smaller hollows (Figure 4.12). Thus, oleylamine countermands the tendency towards hollow structure formation, at the same time favoring the more metal-rich phase.
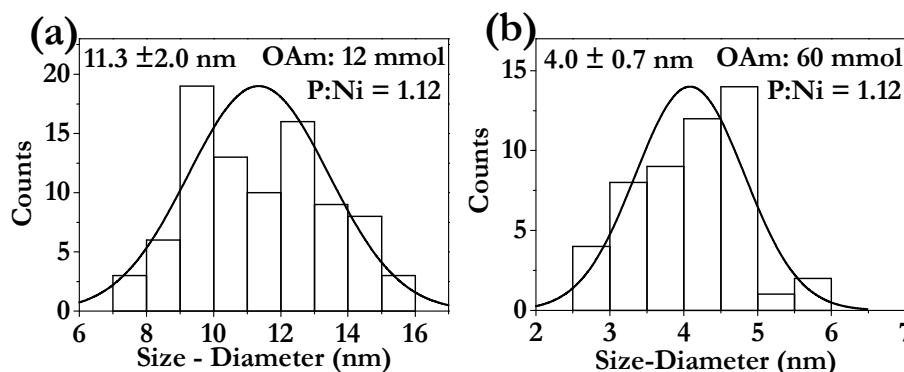
Figure 4.12. Histograms of the size of the voids in $Ni_{12}P_5$ hollow nanoparticles prepared with varying oleylamine quantities (a) 12 mmol (b) 60 mmol.

4.3.5 Topotactic conversion of $Ni_{12}P_5$ to Ni_2P

During the course of the investigation on controlling phase in the nickel phosphide system, it was observed that even at a relatively low temperature of 300 °C, the metal-rich $Ni_{12}P_5$ will undergo a transformation to the less metal-rich Ni_2P phase with increasing heating time (Figure 4.13). This transformation was similar to those observed for the Fe-P system, as described in Chapter 3.[86] Thus, when the heating time was varied in one-pot reaction reactions carried out at 300 °C with a P:Ni precursor ratio of 2.24 (4 mmol Ni and 4 mL TOP) and 3 equivalents of oleylamine (relative to Ni), a gradual transformation from $Ni_{12}P_5$ to Ni_2P was observed. The PXRD pattern of the sample isolated after 30 minutes of reaction time was indicative of a poorly crystalline material, and it was difficult to associate the pattern with any particular phase. After 1 h, an almost phase pure product, $Ni_{12}P_5$ formed, and when the reaction time was extended to 2 h, the

additional heating time was observed to promote the formation of the more P-rich product, Ni_2P as a minor phase along with $Ni_{12}P_5$. After nearly 6 h of reaction time, the product was characterized to be Ni_2P rich along with $Ni_{12}P_5$ as minor phase. This trend continues in the 12 h reaction product but even after 24 h heating time, a significant amount of $Ni_{12}P_5$ remains. We hypothesized that the limiting factor in this case could be the P:Ni precursor ratio (2.24) and the reaction temperature (300 °C). Indeed, when a similar reaction series was carried out at 350 °C with a slightly higher P:Ni ratio of 2.8 (4 mmol Ni and 5 mL TOP) and 3 equivalents of oleylamine (relative to Ni), complete transformation to Ni_2P was achieved within 6 h (Figure 4.14).
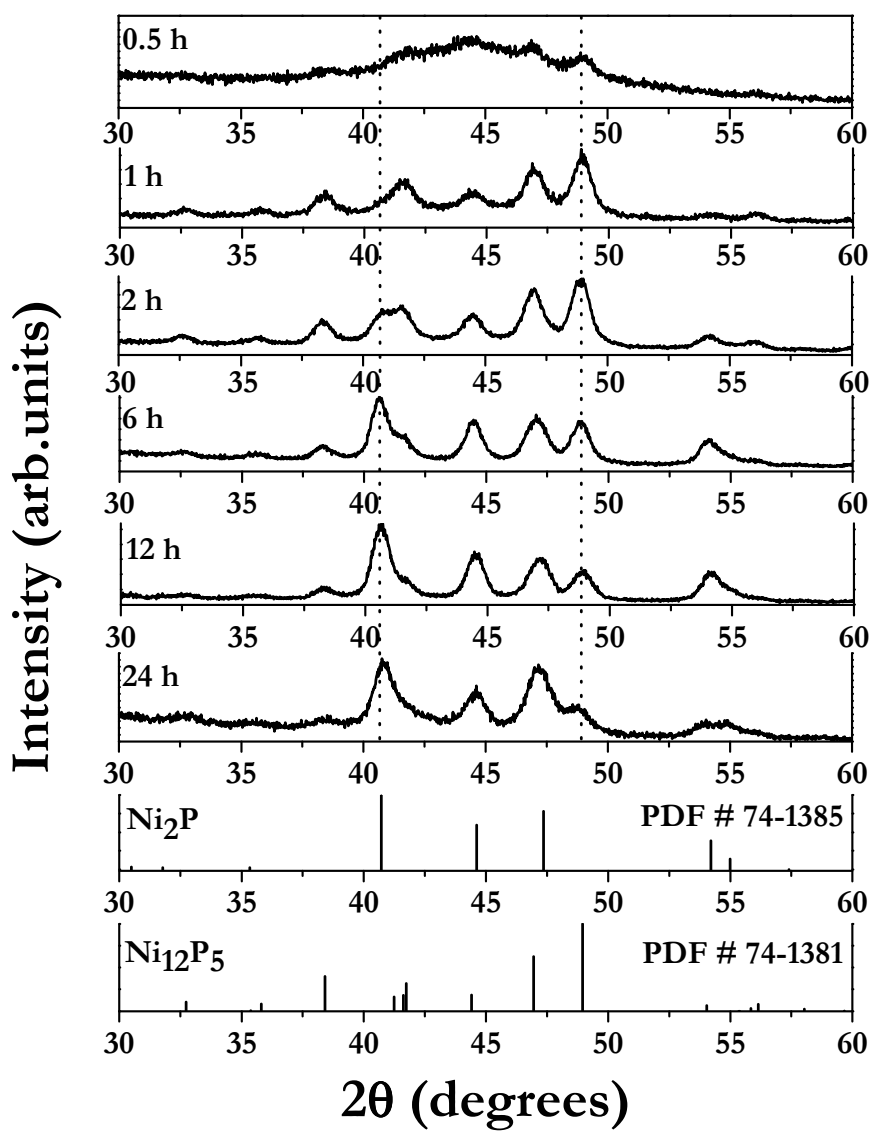
Figure 4.13. PXRD patterns of the final products prepared with varying reaction times at

300 °C and compared to the reference patterns for $Ni_{12}P_5$ and Ni_2P.
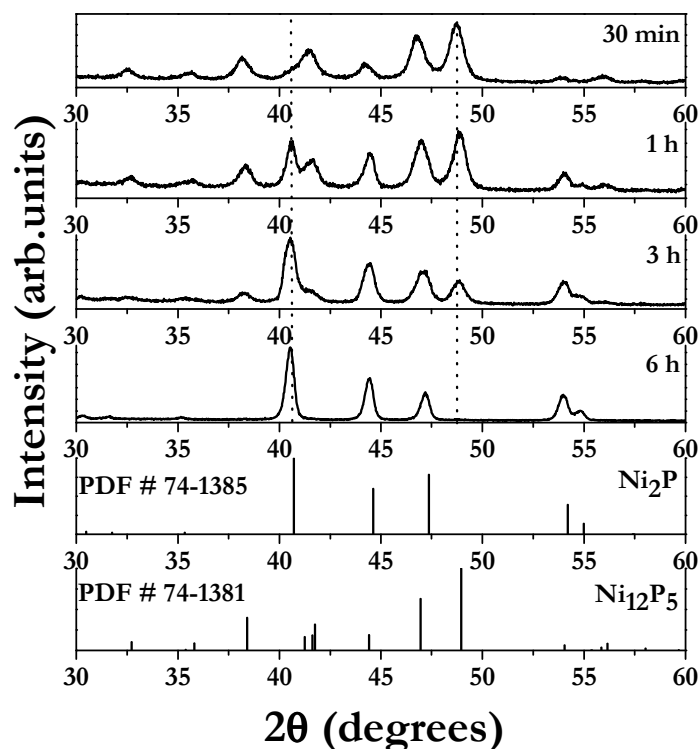
Figure 4.14. PXRD patterns of the final products prepared with varying reaction times at 350 °C and compared to the reference patterns for $Ni_{12}P_5$ and Ni_2P.

The results in Figure 4.13 and 4.14 suggested that when reaction conditions are optimum, it should be possible to achieve complete transformation of metal-rich to P-rich phases by reaction with TOP. To test this hypothesis, hollow and solid $Ni_{12}P_5$ nanoparticles were prepared following the optimized reaction conditions as described in the previous sections 4.3.1 and 4.3.4, respectively. 200-250 mg of the as-prepared nanoparticles were combined with octyl ether and oleylamine and the temperature raised to 300 °C under Ar after degassing. 15 mL TOP was introduced into the system at this stage and the temperature was subsequently raised to 350 °C and maintained for 3-4 h. PXRD patterns of the isolated products indicated that both hollow and solid $Ni_{12}P_5$ nanoparticles completely converted to Ni_2P (Figure 4.15a, b).
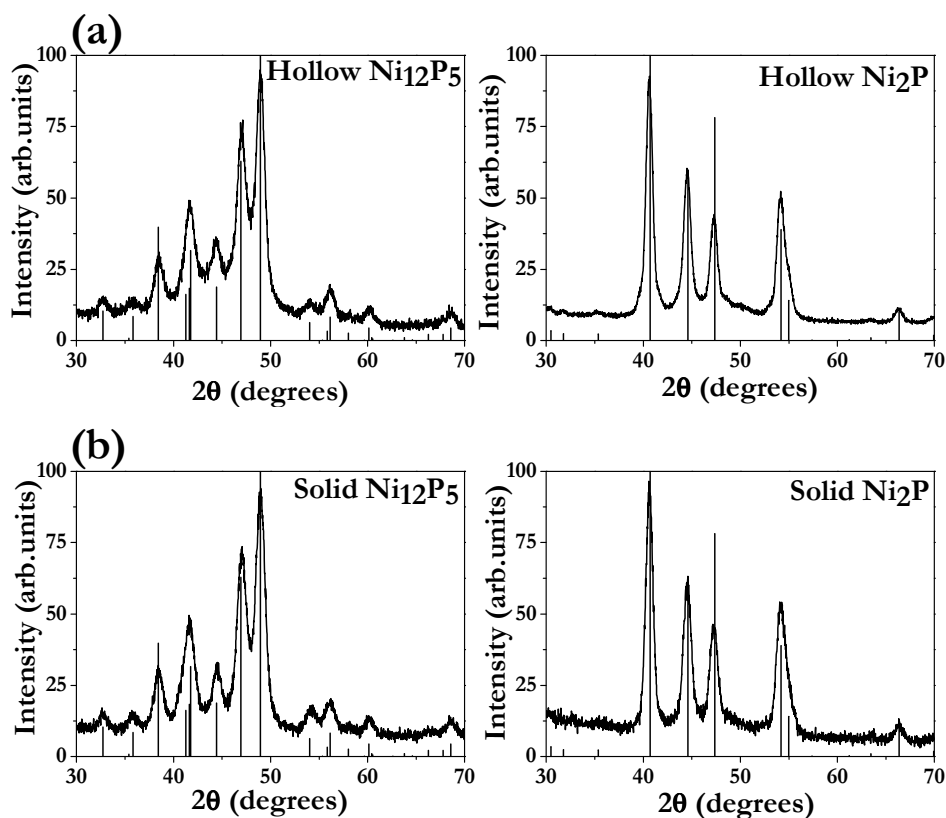
Figure 4.15. PXRD and reference patterns indicating the transformations from $Ni_{12}P_5$ to Ni_2P. (a) Hollow $Ni_{12}P_5 \rightarrow Ni_2P$ and (b) Solid $Ni_{12}P_5 \rightarrow Ni_2P$.

When the products were analyzed by TEM, it was observed that the Ni_2P samples retained the morphology of the precursor hollow $Ni_{12}P_5$ nanoparticles. EDS data obtained on both hollow $Ni_{12}P_5$ and hollow Ni_2P nanoparticles were observed to be consistent with the expected values (Figure 4.16a, b). Similarly, solid $Ni_{12}P_5$ nanoparticles on transformation yielded solid Ni_2P nanoparticles and EDS data again was in agreement with the expected values associated with the transformation to a more P-rich phase (Figure 4.16 c, d). The product sizes were almost identical to the starting materials. This fact, coupled with the retention of morphology, makes a strong argument for a topotactic transformation.

(a) Hollow Ni₁₂P₅ nanoparticles
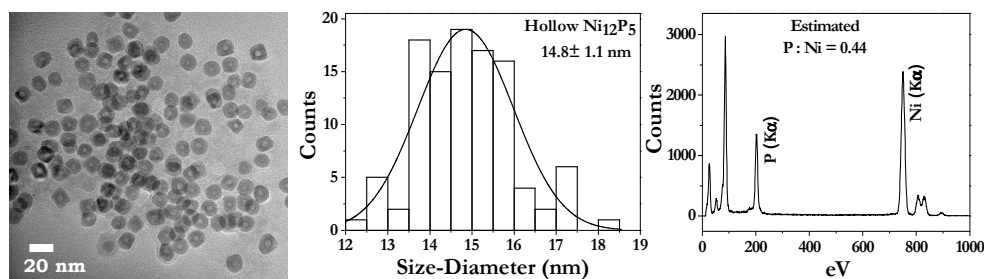
(b) Hollow Ni₂P nanoparticles
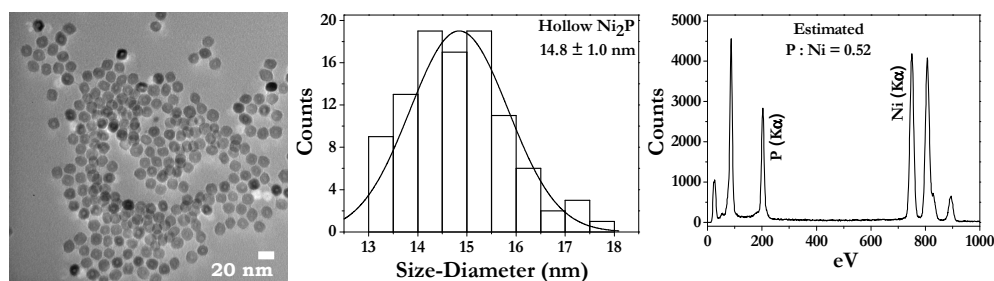
(c) Solid Ni₁₂P₅ nanoparticles
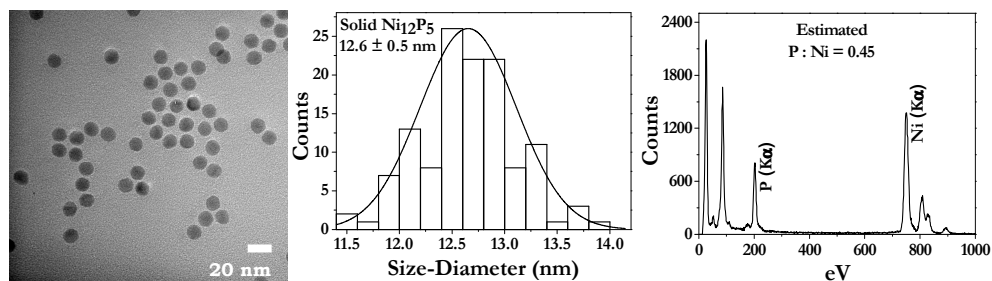
(d) Solid Ni₂P nanoparticles
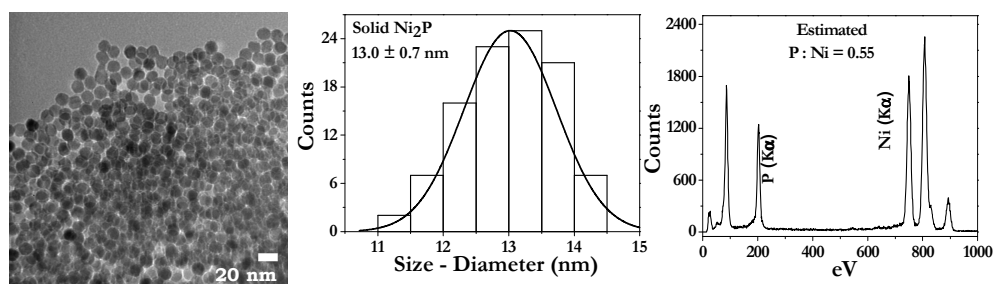
Figure 4.16. Characterization of nanoparticles: (a) Hollow Ni$_{12}$P$_5$, (b) Hollow Ni$_2$P, (c) Solid Ni$_{12}$P$_5$ and (d) Solid Ni$_2$P: TEM images (left), Histograms (center) and EDS patterns (right). Ideal P:Ni atomic percent compositions for Ni$_{12}$P$_5$ and Ni$_2$P are 0.42 and 0.5, respectively. Excess P is attributed to residual TOP bound to the nanoparticle surface.

4.4.5 Porosimetry Analysis

Preparation of hollow nanoparticles has been given increased attention in recent times due to the potential benefits in catalysis[56] and drug delivery.[94] Yin and coworkers reported that the voids present in hollow nanoparticles are accessible to gas molecules (H_2, C_2H_4, and C_2H_6). Pt@CoO nanoparticles in yolk-shell morphology, were utilized to demonstrate the accessibility by carrying out the Pt nanoparticle catalyzed hydrogenation reaction of ethylene.[56] We expected that porosimetry analysis carried out on the hollow nickel phosphide samples would provide more information on the accessibility of the voids present in them.

Nitrogen adsorption/desorption measurements were carried out on the hollow nickel phosphide ($Ni_{12}P_5$ and Ni_2P) samples at 77 K after degassing at 150 °C overnight. The adsorption and desorption isotherms and pore size distribution derived from the adsorption branch for hollow $Ni_{12}P_5$ and hollow Ni_2P samples are given in Figure 4.17a, b. The isotherms for both samples correspond to a Type IV isotherm. Hysteresis phenomena are observed in both isotherms indicating clearly that the process of pore filling and emptying takes place during the experiment. However, the desorption curve of hollow Ni_2P samples (Figure 4.17b) falls below the adsorption curve, indicating that all pores were not emptied during the degassing step. The computed pore volumes for hollow $Ni_{12}P_5$ and Ni_2P are 0.09 and 0.063 cm^3/g, respectively (Table 4.2). These numbers do not compare well with the pore volumes obtained for porous materials such as the MCM-41 type mesoporous silica nanoparticles, which are observed to be greater than 1.0 cm^3/g.[95] The BET surface area was determined by the application of Equation 2.5 in the adsorption region 0.2 to 2.0. The computed values for BET surface area for the

hollow nickel phosphides are given in Table 4.2. While, the BET surface area of hollow $Ni_{12}P_5$ is comparable to the theoretically obtained value (outer surface only), the surface area has been observed to decrease by more than 50% on its transformation to Ni_2P, despite the fact that TEM analysis (Figure 4.16a, b) does not indicate a change in size of the nanoparticles during transformation. The lower surface area may be attributed to aggregation of the nanoparticles.

The BJH pore size distributions for the hollow $Ni_{12}P_5$ and Ni_2P nanoparticles are given in Figure 4.17a and b, respectively. The average pore size determined from the BJH pore-size determination is given in Table 4.2 and is in the range 6.6-6.9 nm for the hollow nickel phosphide nanoparticles. The comparable pore-sizes to their void size could be an indication of sampling of the voids by the test gas (N_2).

Table 4.2. Table indicating particle and void size, pore volume, average pore size and theoretical and BET surface area of the hollow nickel phosphide nanoparticles.

Hollow sample	TEM particle size (nm)	TEM void size (nm)	BJH pore volume (cm³/g)	BJH avg. pore size (nm)	Theoretical surface area (m²/g)	BET surface area (m²/g)
$Ni_{12}P_5$	14.8	4.2	0.09	6.6	58.7	67.3
Ni_2P	14.8	4.2	0.063	6.9	60.1	17.3

The results of a similar analysis carried out with the solid nanoparticles of $Ni_{12}P_5$ and Ni_2P are given in Table 4.3. Surprisingly, the isotherms for both samples again correspond to a Type IV isotherm (Figure 4.17c, d) and pore filling and emptying are indicated by the presence of hysteresis loops with the desorption isotherm for solid Ni_2P

sample falling below the adsorption indicating an incomplete degassing process. The computed pore volumes for the solid $Ni_{12}P_5$ and Ni_2P nanoparticles are somewhat smaller than those for hollow nanoparticles at 0.031 and 0.039 cm^3/g, respectively. However, distinct differences were not observed in the pore size distributions of solid nickel phosphide samples relative to the hollow nickel phosphide nanoparticles. The BJH pore-size distribution for the solid nickel phosphide nanoparticles are given in Figure 4.17c, d and the average pore-size determined from the distribution is in the range 5.4-7.9 nm very similar to those observed for hollow nanoparticles. The pore sizes correspond to nearly half the size of the nanoparticles and thus may be more reflective of voids formed between the nanoparticles rather than the pores and hollow structures present in individual nanoparticles.

Table 4.3. Table indicating particle size, pore volume, average pore size and theoretical and BET surface area of the solid nickel phosphide nanoparticles.

Solid Sample	TEM Particle Size (nm)	BJH Pore Volume (cm^3/g)	BJH Avg. Pore Size (nm)	Theoretical Surface Area (m^2/g)	BET Surface Area (m^2/g)
$Ni_{12}P_5$	12.6	0.031	5.4	58.7	67.3
Ni_2P	13.0	0.039	7.9	60.1	17.3

Given the uniformity of the particle sizes, close-packed structures or similar local order could give rise to a relatively uniform sampling volume – translating to the narrow pore-size distribution from the BJH model. Thus a conclusive evidence of the

accessibility of the voids to the test gas (N_2), could not be established with this set of preliminary porosimetry experiments.
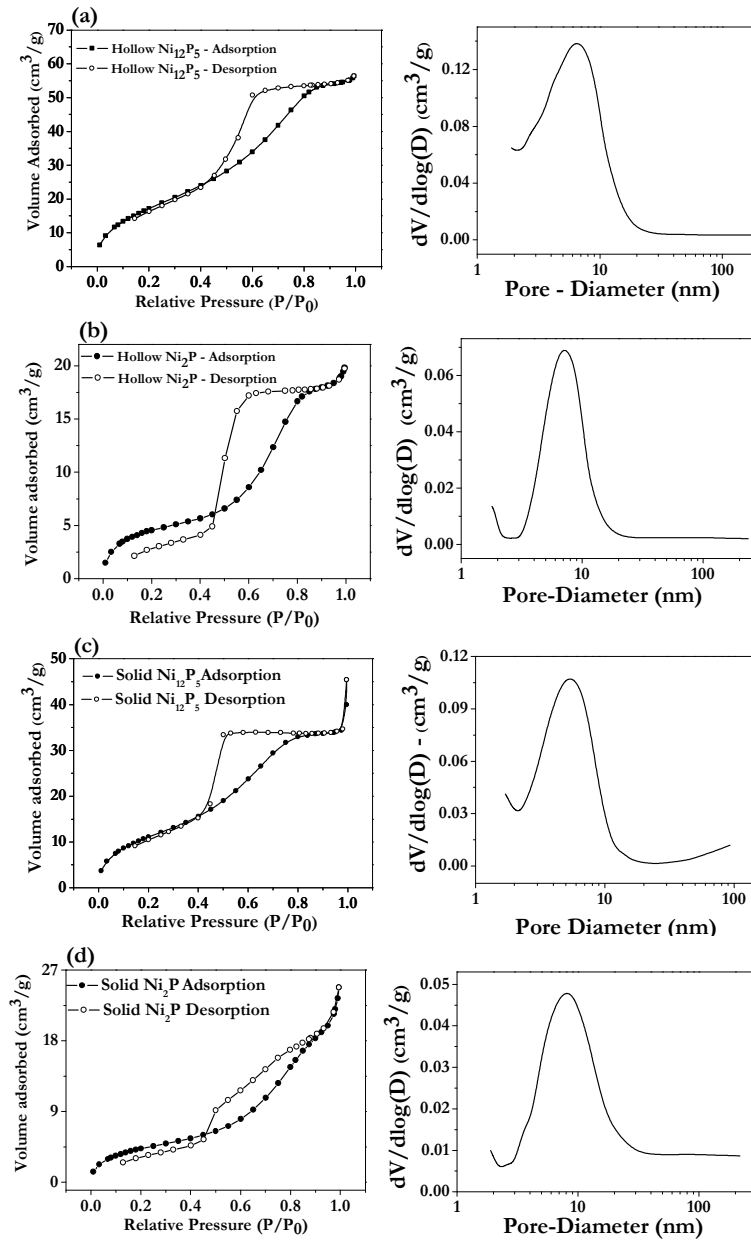
Figure 4.17. Adsorption and desorption isotherms and BJH pore size distributions (derived from the adsorption branch) of (a) hollow $Ni_{12}P_5$, (b) hollow Ni_2P, (c) solid $Ni_{12}P_5$ and (d) solid Ni_2P.

4.4.6 Conclusion

Reaction parameters have been utilized as levers to tune phase, size and morphology in the nickel phosphide system, enabling phase pure samples of $Ni_{12}P_5$ and Ni_2P to be prepared in both solid and hollow morphologies. The P:Ni precursor ratio has been identified as the primary synthetic lever, playing an important role in controlling all the above mentioned physical attributes of the samples. Reaction time and temperature played a secondary role in controlling the phase of the final product. Excess oleylamine stabilized the more reduced phase $Ni_{12}P_5$, offsetting the effects of a high P:Ni ratio and enabling this phase to be realized in solid morphology. In addition to being able to access the different phases, it was discovered that they can be topotactically transformed from $Ni_{12}P_5$ to Ni_2P. Finally, the nature of the voids was probed by N_2 physisorption, but based on data from hollow and solid nanoparticles it appears that only the inter particle voids are being probed.

CHAPTER 5

SOLUTION PHASE CONVERSION OF NANOSCALE TRANSITION METAL OXIDES TO PHOSPHIDES AND SULFIDES

5.1 Introduction

In this chapter, the transformation of transition metal oxide nanoparticles to their corresponding phosphides and sulfides is described. The conversion reactions illustrated in this chapter demonstrate the reactive nature of oxide systems when prepared on the nanoscale and address a persistent concern that oxidation limits reactivity in nanoparticle conversion reactions.[53] The preparation of NiO, Fe_3O_4, CoO and Mn_3O_4 nanoparticles by the decomposition of their salts in air and their subsequent transformation to phosphides and sulfides by reaction with TOP and elemental sulfur, respectively, is reported. PXRD and EDS were employed to monitor the transformation to phosphides. In addition, the non-reactive nature of a bulk oxide system under similar reaction conditions is presented to highlight the enhanced reactivity on the nanoscale.

5.2 Experimental Section

All chemicals used for syntheses described in this chapter are listed in Chapter 2.1.

5.2.1 Synthesis of NiO nanoparticles and subsequent transformation to Ni_2P

The oxide nanoparticle formation was brought about by the decomposition of a metal salt in a high boiling solvent/surfactant system under air flow, a route previously reported by Yin and coworkers for CoO.[56] In the case of NiO nanoparticles, 4 mmol of $Ni(acac)_2$ was combined with 10 mL octyl ether and 8 mL oleylamine. The system was

raised to 250 °C under slow and steady air flow and maintained at that temperature for 2-3 h. The resultant brownish dispersion was then cooled down to room temperature (RT) and the final product was isolated by precipitation with excess ethanol, followed by centrifugation. The isolated nanoparticles were re-dispersed in a small quantity of $CHCl_3$ (1-2 mL) and then re-precipitated with excess ethanol. The washed product was dried under vacuum to obtain a free flowing powder.

The transformation of oxides to phosphides was carried out under Ar atmosphere. A known quantity of the NiO nanoparticles (50-100 mg) was combined with octyl ether (10.0 mL) and oleylamine (2.0 mL) and the system was degassed at 100 °C under partial vacuum for 20-30 minutes. The system was then purged with Ar and the temperature was raised to 300 °C. 15.0 mL TOP was injected into the system and the temperature was subsequently raised to 350-370 °C for reaction times of 3-4 h. Isolation of the final product was carried out by precipitation with excess ethanol followed by centrifugation at RT. Isolated nanoparticles were then dispersed in a minimum quantity of $CHCl_3$ and re-precipitated again with excess ethanol to obtain a free flowing powder.

5.2.2 Synthesis of CoO, Fe_3O_4 and Mn_3O_4 nanoparticles and subsequent transformation to their corresponding phosphide phases

CoO, Fe_3O_4, and Mn_3O_4 nanoparticles were prepared using a similar decomposition route as described for the preparation of NiO nanoparticles, using $Co(acac)_2$, $Fe(acac)_3$, and $Mn(acac)_2$, respectively. CoO, Fe_3O_4 and Mn_3O_4 nanoparticles were subjected to transformation reactions with TOP at 370 °C from between 3 and 24 h. Isolation of the final products was carried out as described for the Ni_2P system in 5.2.1.

5.2.3 Reaction of commercial NiO nanoparticles with TOP

1 mmol of commercial NiO nanopowder was combined with 10.0 mL octadecene and 2.0 mL oleylamine. The system was degassed at 100 °C under a partial vacuum for 20 min, and then the temperature was raised to 300 °C, where it was maintained for about 1 h. The hot NiO nanoparticle dispersion was then cannulated into another Schlenk flask, containing 20.0 mL TOP preheated to 350 °C. The temperature of the resultant solution was then raised to 385 °C and maintained for 16 h. Subsequently, an additional 15.0 mL of TOP was then injected into the system at a rate of 0.5 mL/min. The system was maintained at 385 °C for another 8 h. Isolation of the final product was carried out in the same way as described for Ni_2P in 5.2.1.

5.2.4 Reaction of a bulk NiO sample with TOP

0.3 g of NiO was combined with 10.0 mL octyl ether and 2.0 mL oleylamine. The system was degassed at 100 °C under partial vacuum and then the temperature was raised to 300 °C under an Ar atmosphere. The system was maintained at 300 °C for about 1 h and then raised to 370 °C. 20.0 mL TOP was injected into the system and the temperature was raised to 385 °C, where it was maintained for about 16 h. Isolation of the final product was carried out as described for Ni_2P in 5.2.1.

5.2.5 Conversion to sulfide phases

50-60 mg of the as-prepared oxide nanoparticles was combined with octyl ether (10.0 mL) and oleylamine (10.0 mL) and 8 mmol sulfur flakes. The system was degassed at 100 °C under partial vacuum for about 15-20 minutes. The temperature was raised to 300-350 °C under an atmosphere of Ar and maintained for 6-8 h. Isolation of final product was carried out at RT by precipitation with excess ethanol (20-30 mL) followed

by centrifugation. The isolated product was then dispersed in a minimum quantity of chloroform (1.0 mL), re-precipitated with excess ethanol again and then dried under vacuum to yield a free flowing powder.

5.3 Results and Discussion

Schaak and coworkers described the use of TOP as a general precursor for converting transition metal nanoparticles into phosphides.[53] This approach was adapted to generate phase-pure products of iron and nickel phosphides of different stoichiometries, as described in Chapter 3 and 4. However, surface oxidation, which is endemic among most transition metal nanoparticles, was purported by Schaak and coworkers to limit reactivity towards TOP.[53] Nevertheless, a few reports indicated the possible transformation of oxides into phosphides and sulfides. Lee and coworkers transformed Fe_3O_4 nanoparticles into Fe_2P nanorods by reaction with TOP at 310 °C, using Pd nanoparticles as a catalyst.[96] Hydrogen plasma was employed by Wang and coworkers to convert bulk and supported metal oxide precursors into their respective phosphides by treating them with P_2O_5.[97] Finally, Seo and coworkers reported the conversion of Nd_2O_3 nanoparticles into phase pure NdS_2 using a mixture of boron and sulfur powders at 450 °C in vacuum sealed tubes.[98] Herein we show that not only is surface oxidation no impediment to phosphide formation, even completely oxidized particles can be converted to phosphides with TOP, and into sulfides with elemental sulfur, without the need of noble metal catalysts and at temperatures < 400 °C.

5.3.1 NiO nanoparticle synthesis and subsequent conversion to Ni_2P nanorods

$Ni(acac)_2$ was decomposed under air flow to result in the formation of NiO nanoparticles. The isolated nanoparticles were brownish in color, and the PXRD pattern

was found to be a perfect match to the reference pattern of NiO (Figure 5.1). No additional peaks were observed, suggesting little or no crystalline impurities were present. Moreover, the linear response of the room temperature magnetization with applied field (Figure 5.2) is indicative of field-independent magnetic susceptibility, consistent with a paramagnetic response, and thus the absence of unreacted Ni.
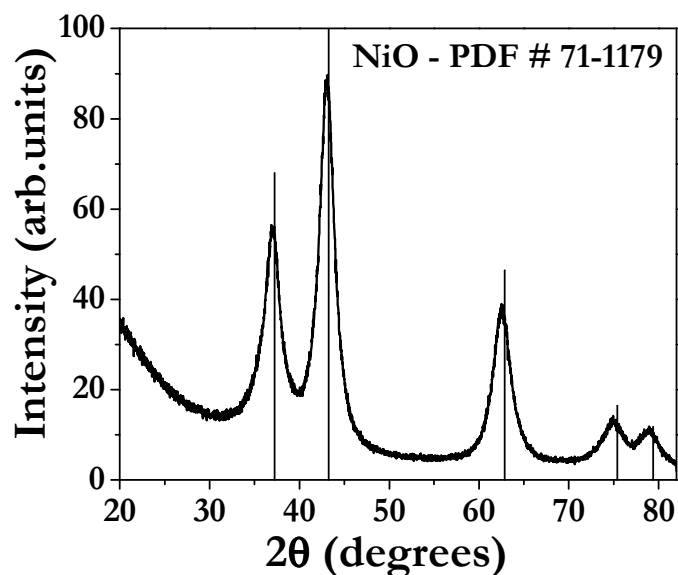
Figure 5.1 PXRD pattern of NiO nanoparticles compared to the reference pattern (PDF # 71-1179). Reproduced with permission from reference[99]. Copyright 2010 American Chemical Society.
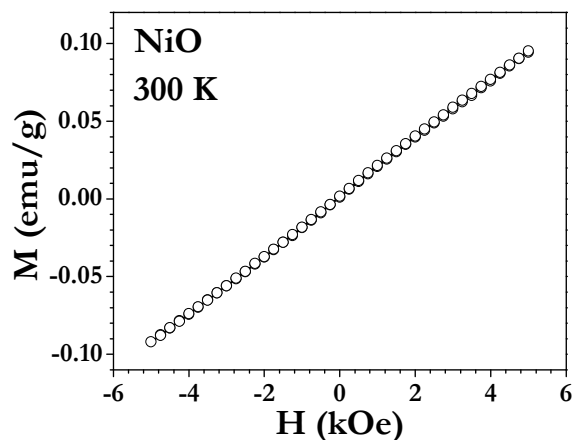
Figure 5.2 M(H) measurement carried out between -5 kOe and 5 kOe for NiO nanoparticles at 300 K. Reproduced with permission from reference[99]. Copyright 2010 American Chemical Society.

TEM images revealed the formation of nanoparticles with roughly spherical morphology and of sizes in the range 3-5 nm (Figure 5.3). This is consistent with the size obtained by Scherrer analysis of the PXRD pattern, 4.4 nm, suggesting that the particles are completely crystalline.
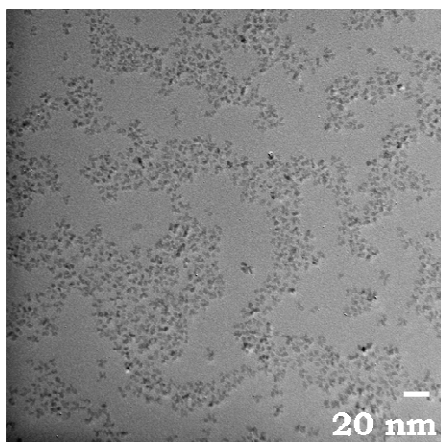
Figure 5.3 TEM image indicating a roughly spherical morphology for NiO nanoparticles. Reproduced with permission from reference[99]. Copyright 2010 American Chemical Society.

The free-flowing dry NiO nanoparticles were then treated with TOP in a solvent mixture of octyl ether and oleylamine at 350 °C for 2-3 h, during which time the color of the solution turned from the characteristic brown of NiO to black. Isolation of the final product was carried out by precipitation with excess ethanol followed by centrifugation.

The PXRD pattern of the reaction product of NiO with TOP suggested complete conversion to Ni_2P (Figure 5.4). There was no evidence of residual oxide or of any other nickel phosphide phase. Additionally, relative to the other peaks in the pattern, the (002) reflection was found to be sharp, and the (210) broad, suggesting that the particles have a preferred direction of growth along the *c*-axis.[48]
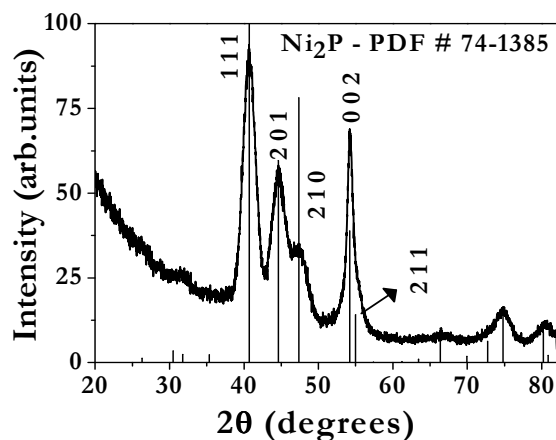
Figure 5.4 PXRD pattern of Ni_2P obtained from the reaction of NiO nanoparticles with TOP compared to the reference pattern (PDF # 74-1385). Reproduced with permission from reference[99]. Copyright 2010 American Chemical Society.

The formation of rods was confirmed by TEM analysis (Figure 5.5a) and the nanorods were calculated to have an average length of 17.9 ± 2.6 nm and width of 4.0 ±

0.3 nm (Figure 5.5 b, c). EDS data is in agreement with the expected ratios for Ni:P (Figure 5.5d), but with an excess 10.3 at. % P over the ideal 2:1 Ni:P ratio, which can be attributed to residual TOP ligating groups present on the nanorod surface.
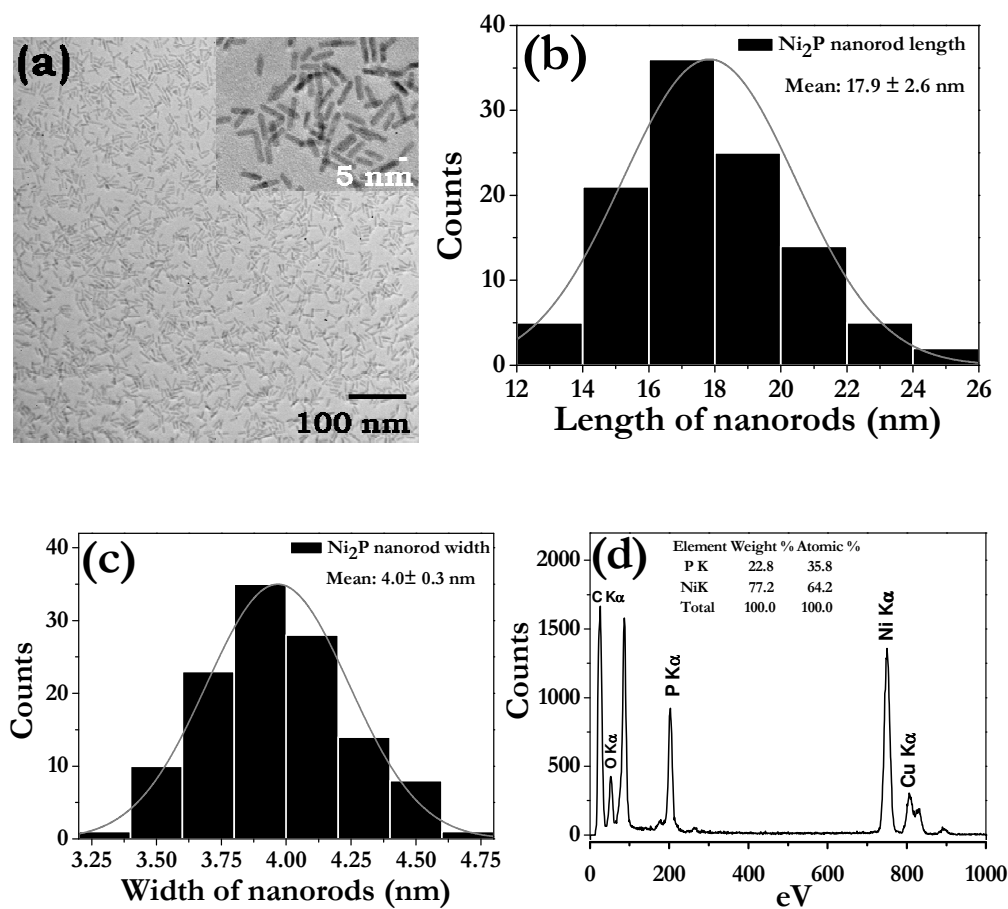
Figure 5.5 (a) TEM image indicating rod morphology of Ni$_2$P. Histograms depicting the distribution of the dimensions of Ni$_2$P nanorods (b) for length (c) for width and (d) EDS data of Ni$_2$P nanorods indicating a slight excess at. % P, attributed to surface TOP ligating groups. Reproduced with permission from reference[99]. Copyright 2010 American Chemical Society.

The formation of nanorods indicates that the reaction of NiO with TOP is not topotactic, but probably arises from dissolution of the oxide, with anisotropy exhibited as a consequence of a high constant concentration of Ni obtained from NiO, and the hexagonal symmetry of the crystal structure.[100] This new method of producing nanorods does not require continuous controlled injection of precursors,[48, 50] or the use of multiple ligands[22] with different binding strengths to promote formation of rods/wires. Moreover, it is possible to adjust the aspect ratio of the nanorods by varying the NiO concentration. Thus, increasing the concentration 3-fold led to a corresponding increase in aspect ratio (Figure 5.6).
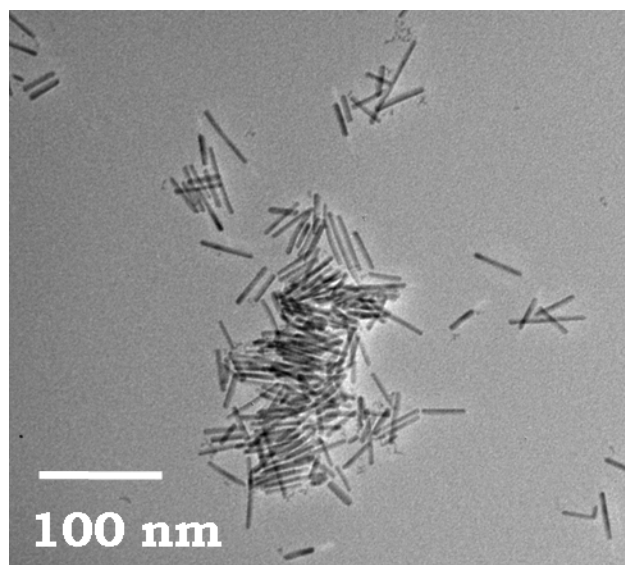
Figure 5.6 TEM image of Ni_2P nanorods with higher aspect ratio (~12.5). Reproduced with permission from reference[99]. Copyright 2010 American Chemical Society.

5.3.2 CoO and Fe$_3$O$_4$ nanoparticles and subsequent conversion to phosphides

In addition to NiO, we also tested the reactivity of TOP towards iron and cobalt oxide nanoparticles. Oxide nanoparticles of Fe and Co were synthesized analogously to NiO, as described in 5.3.1. The isolated nanoparticles were characterized by PXRD and the patterns confirm the formation of Fe$_3$O$_4$ and CoO (Figure 5.7a, b). TEM images indicate the formation of roughly spherical nanoparticles (Figure 5.7c, d). Detailed analysis of the particle size was not carried out: however, size measurements indicated that the Fe$_3$O$_4$ nanoparticles were in 4-7 nm range and CoO nanoparticles were in the 8-12 nm range.
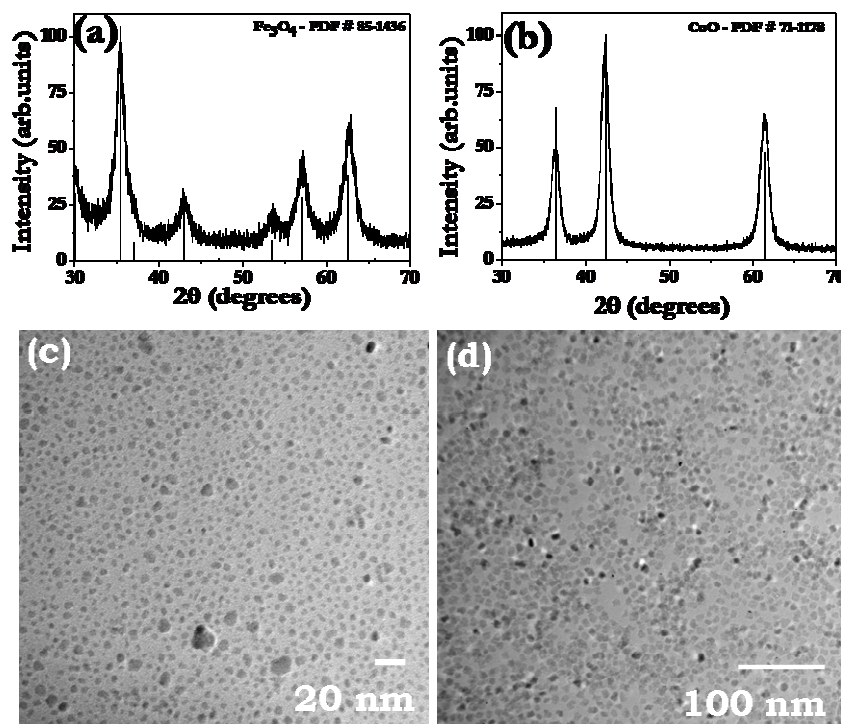
Figure 5.7 PXRD patterns of (a) Fe$_3$O$_4$ nanoparticles and (b) CoO nanoparticles. TEM images of (c) Fe$_3$O$_4$ nanoparticles and (d) CoO nanoparticles. Reproduced with permission from reference[99]. Copyright 2010 American Chemical Society.

Conversion reactions were carried out with the as-prepared Fe_3O_4 nanoparticles (Figure 5.7a, c) and CoO nanoparticles (Figure 5.7b, d) with TOP over 4 h at 350 °C. In both systems, the products were characterized to be a mixture of two phases by PXRD (Figure 5.8). Similar to Ni, the metal (M)-rich M_2P phases appear to be favored at shorter times, but were also accompanied by significant quantities of the MP phases.
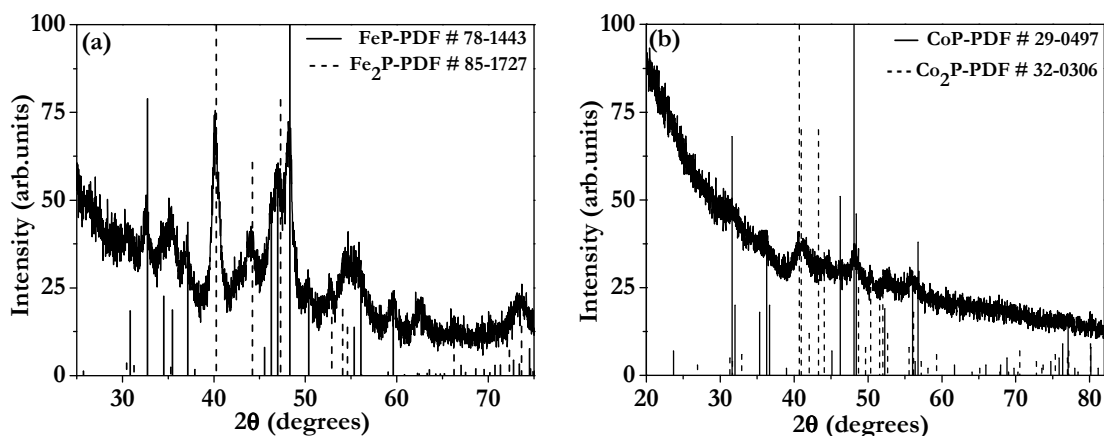
Figure 5.8 PXRD patterns of the final products obtained after 4 h reactions with TOP at 350 °C for (a) iron oxide and (b) cobalt oxide nanoparticles. Reproduced with permission from reference[99]. Copyright 2010 American Chemical Society.

Based on the knowledge developed from the Fe-P and Ni-P work described in Chapter 3 and 4, phase-pure products can be prepared by extending the heating time and/or by working at a higher temperature. Accordingly, conversion reactions of both Fe_3O_4 and CoO nanoparticles were extended to 24 h while the reaction for Co was carried out at a higher temperature, 370 °C. PXRD patterns of the isolated products indicated synthesis of phase-pure FeP and CoP (Figure 5.9a, b). The formation of the less metal-rich phase at longer times and higher temperatures is consistent with our previous work

on phosphidation of Fe and Ni nanoparticles (Chapter 3, 4).[86] TEM analyses of the final products indicated that the FeP nanoparticles were present as clumps up to 50 nm in diameter (Figure 5.10a), whereas CoP nanoparticles form as discrete particles of comparable size to the CoO precursor (Figure 5.10b). EDS analysis indicated the presence of excess phosphorus for both FeP and CoP samples, which is attributed to the presence of ligating TOP on their surface. Based on the metal content, an excess of 23.3 and 26.0 at. % P was present in FeP and CoP, respectively (Figure 5.11a,b).
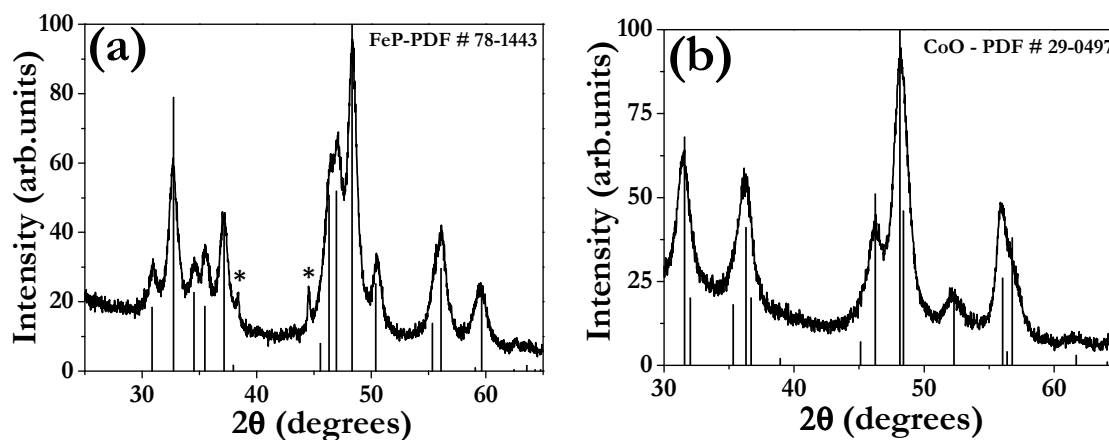
Figure 5.9 PXRD patterns of (a) FeP and (b) CoP nanoparticles compared to their reference patterns. * indicates peaks from sample holder. Reproduced with permission from reference[99]. Copyright 2010 American Chemical Society.
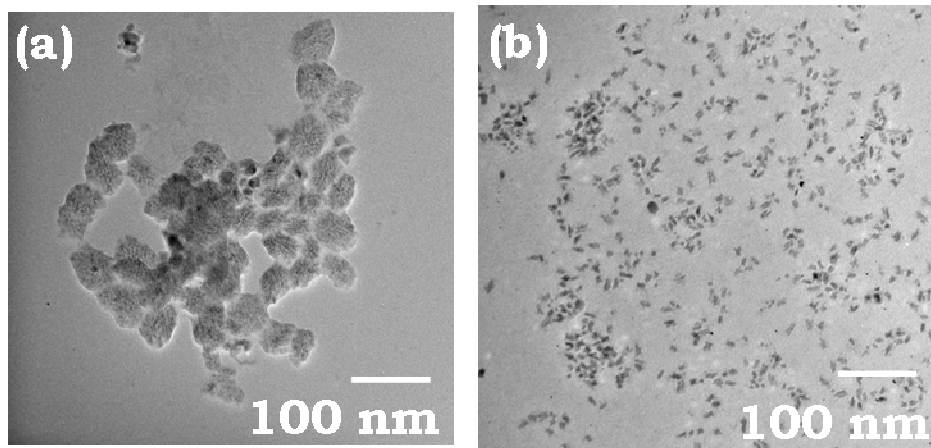
Figure 5.10 TEM images of phase-pure (a) FeP nanoparticles and (b) CoP nanoparticles. Reproduced with permission from reference[99]. Copyright 2010 American Chemical Society.
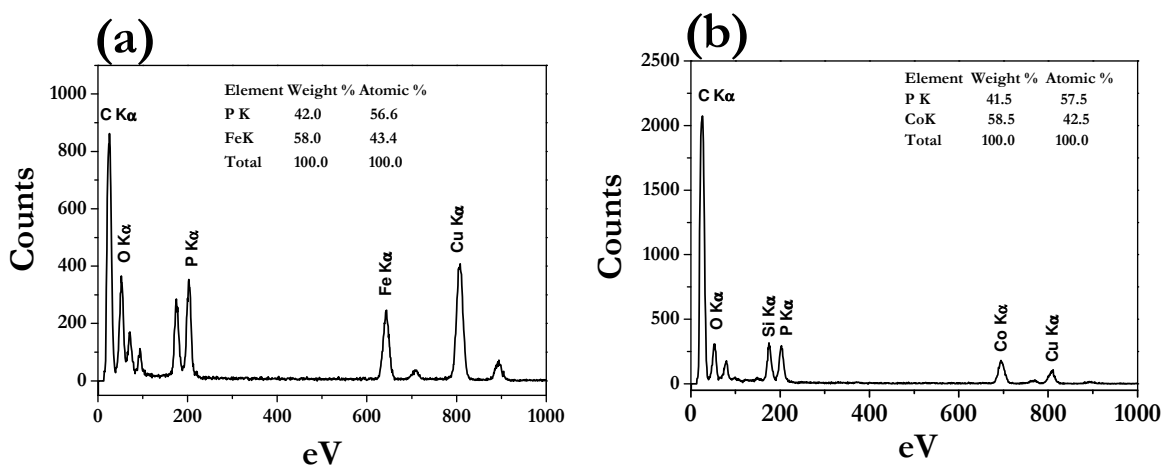
Figure 5.11 EDS data obtained on the phase-pure samples of (a) FeP nanoparticles and (b) CoP nanoparticles. Reproduced with permission from reference[99]. Copyright 2010 American Chemical Society.

5.3.3 Unsuccessful conversion of Mn₃O₄ into phosphide phase

Reaction of TOP with Mn_3O_4 nanoparticles at 370 °C for 24 h was found to be insufficient enough for transformation to phosphide phase. Instead, the PXRD pattern of the final product indicated that TOP induced reduction of Mn_3O_4 to MnO (Figure 5.12). Gopalakrishnan and coworkers reported a similar inability to reduce Mn-phosphate to phosphide under hydrogen at high temperatures. They suggested that the barrier for phosphide generation of Mn is due to its low electronegativity relative to later transition metals.[101]
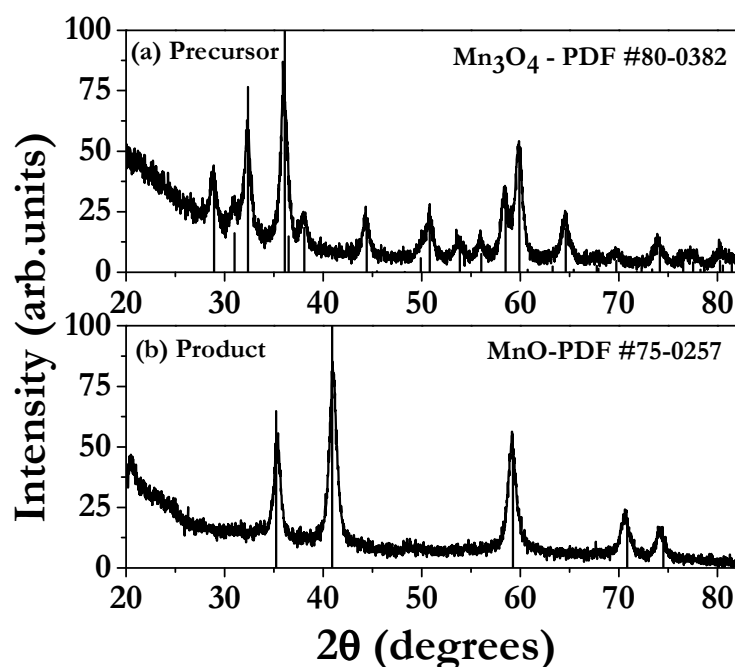
Figure 5.12 PXRD and reference patterns of (a) Mn_3O_4 nanoparticles and the product (b) MnO obtained after reaction with TOP. Reproduced with permission from reference[99]. Copyright 2010 American Chemical Society.

5.3.4 Effect of particle size on conversion

In order to test the effect of size on the conversion of oxides to phosphides, control reactions were carried out by treating a sample of bulk NiO with TOP. The PXRD pattern of the product clearly indicated that the bulk samples remained principally oxides (Figure 5.13a), although there was a small peak at 41° 2θ that may be indicative of phosphide formation on the surface. However, when a polydisperse sample of NiO nanoparticles with size ≤50 nm was treated with TOP for 24 h at 385 °C, the product was found to be a mixture of NiO and Ni_2P (Figure 5.13b). Thus, while smaller nanoparticles transformed completely into phosphide within 3-4 h (Figure 5.4 and 5.5), complete transformation to the phosphide phase was not achieved with the commercial NiO nanoparticles even after a 24 h reaction time. These observations lead us to conclude that the transformation of oxide to phosphide is related to solubility or reactivity of the oxide nanoparticles, effects augmented at small particle sizes. The phosphides formed on the surface can also act as barriers, inhibiting complete conversion of the system even under forcing conditions, similar to the results obtained for the Fe-P system (Chapter 3).[86]
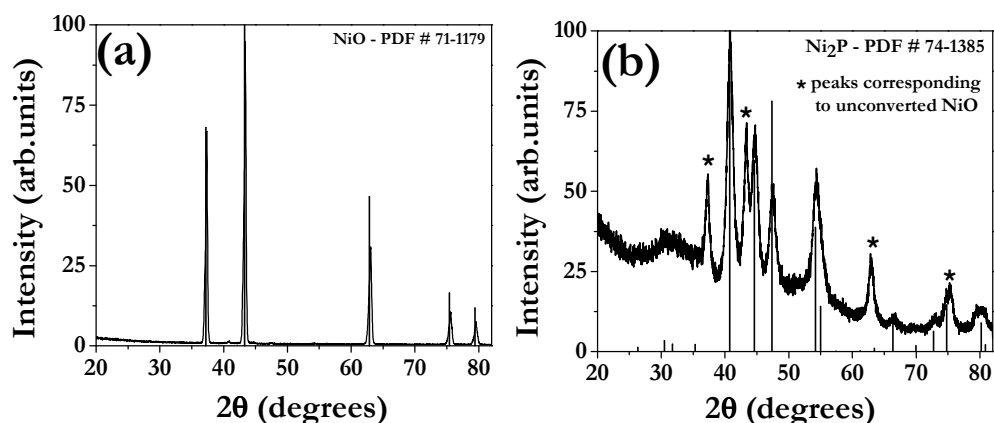
Figure 5.13 PXRD and reference patterns of the final products obtained after the reaction of TOP with (a) Bulk NiO sample and (b) Commercial NiO nanoparticles (<50 nm by BET). Reproduced with permission from reference[99]. Copyright 2010 American Chemical Society.

5.3.5 Conversion to sulfides

Oxide to sulfide nanoparticle transformation was first reported by Seo and coworkers, for the conversion of Nd_2O_3 nanoparticles into phase pure NdS_2 using a mixture of boron and sulfur powders at 450 °C in vacuum sealed tubes.[98] We tested the applicability of our oxide conversion method for the formation of transition metal sulfides using elemental sulfur. The as-prepared oxide nanoparticles (50-60 mg) were reacted with 8 mmol sulfur flakes at 350 °C for 6 h in a solvent/surfactant system composed of octyl ether and oleylamine. The PXRD pattern (Figure 5.14a) of the product of NiO nanoparticles with sulfur indicates the successful transformation into Ni_9S_8 (major) and Ni_3S_2. Co and Fe oxides were also successfully transformed under similar reaction conditions, producing phase-pure Co_9S_8 (Figure 5.14b) and a mixed phase sample of FeS_2 (major) and Fe_7S_8 (Figure 5.14c), respectively. Although Mn_3O_4 was not

reactive towards TOP, it readily combined with sulfur to form single phase MnS (Figure 5.14d). Hence oxides are more easily converted into sulfides than to phosphides.
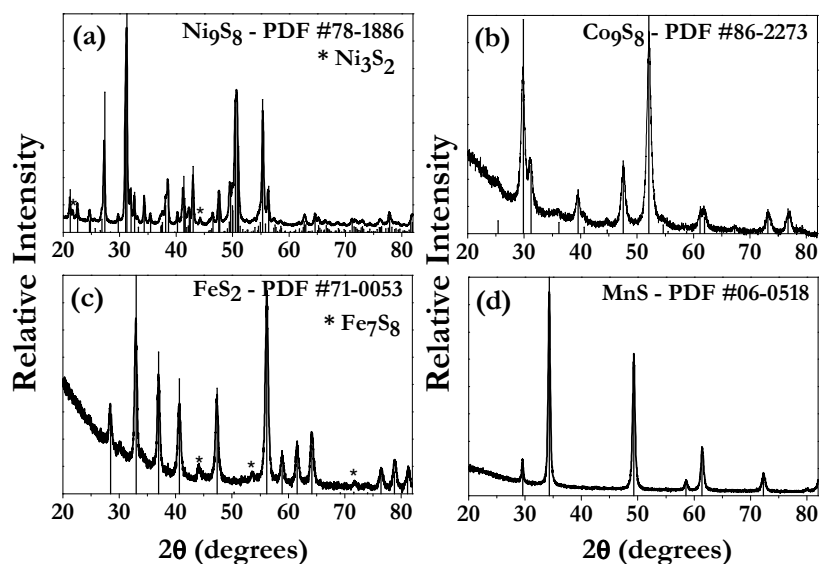
Figure 5.14 PXRD and reference patterns of sulfides prepared by the reaction of sulfur flakes with oxide nanoparticles. (a) Ni_9S_8 (major) and Ni_3S_2 (minor), (b) Co_9S_8, (c) FeS_2 (major) and Fe_7S_8 (minor) and (d) MnS. Reproduced with permission from reference[99]. Copyright 2010 American Chemical Society.

5.4 Conclusions

The results clearly demonstrate that oxidation does not preclude nanoparticle conversion to phosphides, provided the samples are small enough to dissolve (ca. 10 nm) and the metal oxides reactive (Fe, Co, Ni). Moreover, the slow rate of reactant introduction and the high local concentration can enable shape anisotropy to be accessed and controlled. Oxides are even more reactive towards sulfur, yielding sulfides even in cases where the corresponding phosphides can not be produced (as is the case with Mn).

Overall, use of oxide nanoparticles, easily accessed via reaction of inexpensive salts with air, in lieu of organometallic reagents (e.g., metal carbonyls), which may or may not be transformed into metal nanoparticles, greatly simplifies production of nanoscale phosphides and sulfides. The precursor nanoparticles can be produced in large quantities and stored in the solid state without concern that "oxidation" will limit reactivity. Moreover, this reaction is capable of generating phase-pure product in solution at temperatures ≤ 370 °C.

CHAPTER 6

CONCLUSIONS AND PROSPECTUS

Over the last two decades, there has been an increasing interest in the use of nanoscale building blocks for the development of advanced materials.[102] As a result, the attention of the research community has shifted towards the development of synthetic methods to prepare nanoparticles with better control of their physical attributes (size, shape, morphology and phase).[103] Since properties of nanoscale systems vary with size and shape, their size and shape dependant properties are also being continuously explored in order to figure out the optimum characteristics suitable for applications.[5] However, the transition metal pnictide system is much less developed in comparison to the related oxides and chalcogenides, despite the fact that the transition metal pnictides exhibit a range of properties making them suitable for various applications including in catalysis, thermoelectrics and magnetics.[30]

The existence of transition metal pnictides in a wide range of stoichiometries makes it a challenge to prepare these materials as phase-pure samples on the nanoscale. Several synthetic methods reported in the literature were found to suffer from incorporation of small amounts of impurities (competing phases and unreacted metallic species).[48, 67, 72] As a result, accurate determination of the nanoscale properties of the transition metal pnictides was not possible. The recent work of Schaak and coworkers showed the versatility of tri-octylphosphine (TOP) in converting a variety of transition metals into their corresponding phosphides.[53]

The main goal of this dissertation research was to address the issue of contamination in nanoscale samples of transition metal phosphides by developing a general synthetic strategy that can result in better control of phase on the nanoscale, thereby enabling size-dependent properties of selected phases to be probed on the nanoscale. The conversion strategy reported by Schaak and coworkers was adapted to carry out a systematic study, evaluating the effects of various reaction parameters on the phase of the final product. Observations that were made during the investigation led to the arrival of optimum reaction conditions to yield phase-pure samples of FeP and Fe_2P nanoparticles at first. The successful methodology was later applied to the Ni-P system. This combined with the discovery of some additional synthetic levers, has led to simultaneous control on phase, size and morphology of the nanoparticles.

The systematic study reported in Chapter 3 enabled the formation of phase-pure samples of FeP and Fe_2P and the magnetic studies carried out on the as-prepared samples resolved the issues related to their unusual magnetic properties.[86] The selection of phase (FeP or Fe_2P) in the transformation of Fe nanoparticles to phosphides was found to be a sensitive function of heating time, temperature, reaction concentration, and the order of reagent addition. It was found that Fe_2P formed at short reaction times and always tended to adopt a rod morphology. High concentrations of Fe and relatively lower temperatures ($\leq$ 350°C) were required to promote the formation of phase-pure Fe_2P. Increasing reaction times and temperatures resulted in the transformation of Fe_2P to FeP, consistent with the expectation of more reactive phosphorus production in the system. FeP was observed to adopt a spherical morphology. Achieving complete transformation of Fe_2P to FeP proved to be challenging, perhaps due to formation of an FeP shell over the Fe_2P,

which then could act as a barrier to diffusion. This was overcome by carrying out reactions under conditions that thermodynamically suited the formation of P-rich phase, FeP. Hot Fe nanoparticles were cannulated into pre-heated TOP and reactions were carried out at temperatures >350 °C to generate phase-pure FeP nanoparticles. The observed magnetic properties of both Fe_2P and FeP nanoparticles were found to be in agreement with the intrinsic properties reported for their corresponding bulk materials. Based on the results of this study, we were able to conclusively report that the previous reports of unusual magnetic properties could be due to the presence of ferromagnetic impurities (Fe, Fe_2P, Fe_3P) not identifiable by powder X-ray diffraction.

The developed phase-control strategy was successfully extended to the Ni-P system in Chapter 4. Reaction parameters have been utilized as levers to tune phase, size and morphology, enabling phase pure samples of $Ni_{12}P_5$ and Ni_2P to be prepared in both solid and hollow morphologies. The P:Ni precursor ratio has been identified as the primary synthetic lever operating at the precursor particle formation temperature, controlling morphology. At the nickel phosphide crystallization temperature, addition of TOP, reaction time and temperature played key roles in stabilizing the final phase of the product, enabling formation of hollow particles of $Ni_{12}P_5$ and Ni_2P and dense particles of Ni_2P. Excess oleylamine stabilized the more reduced phase $Ni_{12}P_5$, offsetting the effects of a high P:Ni ratio and enabling this phase to be realized in solid morphology, as well as reducing the void size in hollow structures. Thus, the ability to control phase, size and morphology in the Ni-P system is expected to enable the effect of these parameters on HDS catalysis.

As in the case of Fe-P system, it was also observed that with heating time, the phase of the final product can be tuned from $Ni_{12}P_5$ to Ni_2P. In this case, the transformation appears to be topotactic because the morphology of the starting material was conserved. This is in contrast to the case for Fe-P, where clear changes in morphology suggest a dissolution/re-precipitation process.

The enhanced reactivity of oxide systems when prepared in nanoscale was observed in their reaction with TOP as described in Chapter 5. Oxide nanoparticles were prepared by the decomposition of metal salts in high boiling solvent/surfactant systems under a slow and steady air flow. Treatment of the oxide nanoparticles (Fe, Co and Ni) with TOP at elevated temperatures (>350 °C) resulted in the formation of corresponding phosphide phases. The corresponding reactions carried out with bulk oxide samples did not generate the phosphide phases. These results clearly demonstrate that oxidation does not preclude nanoparticle conversion to phosphides, provided the samples are small enough to dissolve (ca. 10 nm) in contrast to previous report by Schaak and coworkers.[53] However, the unreactivity of nanoscale Mn oxides indicates that the method cannot be a general and applicable to all metal oxide systems. Oxides were also found to be reactive towards elemental sulfur, transforming into the corresponding sulfides (even for Mn). These observations suggest that, in most cases, oxidation is not an impediment to phosphide/sulfide formation, and stringent air-free handling of transition metal nanoparticle precursors is unnecessary.

The dissertation research has uncovered a series of synthetic levers that control composition, morphology and size in metal phosphide nanoparticles. The approaches developed, can be extended to generate ternary phosphides containing two different

metals. Doping a second transition metal (Mn, Fe, Ni, Co) into a binary phase has been shown to improve both catalytic activity and augment T_c's in the magnetic materials.[104] Preliminary experiments carried out for the formation of mixed metal phosphides are promising. We are also looking towards the preparation of ternary phosphides with alkali metals such as Na, in order to understand the effect of introducing ionic character into the system. Currently the work on preparation of ternary phosphides is ongoing in our laboratory.

REFERENCES

1.   Freestone, I.; Meeks, N.; Sax, M.; Higgitt, C., The Lycurgus Cup - The Roman Nanotechnology. *Gold Bull.* **2007,** *40* (4), 270-277.

2.   Thompson, D., Birth of Modern Nanotechnology. *Gold Bull.* **2007,** *40* (4), 267-269.

3.   Brock, S., L.; Perera, S.; Stamm, K., L., Chemical Routes for Production of Transition-Metal Phosphides on the Nanoscale: Implications for Advanced Magnetic and Catalytic Materials. *Chem. Eur. J.* **2004,** *10* (14), 3364-3371.

4.   Brock, S. L.; Senevirathne, K., Recent Developments in Synthetic Approaches to Transition Metal Phosphide Nanoparticles for Magnetic and Catalytic Applications. *J. Solid State Chem.* **2008,** *181* (7), 1552-1559.

5.   Burda, C.; Chen, X.; Narayanan, R.; El-Sayed, M. A., Chemistry and Properties of Nanocrystals of Different Shapes. *Chem. Rev.* **2005,** *105* (4), 1025-1102.

6.   Schmid, G., Nanoparticles - From Theory to Application. *Wiley-VCH* **2004**.

7.   Nanoscale Materials in Chemistry. *Wiley-Interscience: NewYork* **2001**.

8.   Huynh, W. U.; Dittmer, J. J.; Alivisatos, A. P., Hybrid Nanorod-Polymer Solar Cells. *Science* **2002,** *295* (5564), 2425-2427.

9.   Liu, J.; Tanaka, T.; Sivula, K.; Alivisatos, A. P.; Fréchet, J. M. J., Employing End-Functional Polythiophene To Control the Morphology of Nanocrystal–Polymer Composites in Hybrid Solar Cells. *J. Am. Chem. Soc.* **2004,** *126* (21), 6550-6551.

10.   Michalet, X.; Pinaud, F. F.; Bentolila, L. A.; Tsay, J. M.; Doose, S.; Li, J. J.; Sundaresan, G.; Wu, A. M.; Gambhir, S. S.; Weiss, S., Quantum Dots for Live Cells, in Vivo Imaging, and Diagnostics. *Science* **2005,** *307* (5709), 538-544.

11.   Yao, Q.; Brock, S. L., Optical Sensing of Triethylamine Using CdSe Aerogels. *Nanotechnology* **2010,** *21* (11), 115502.

12.   Murray, C. B.; Sun, S.; Gaschler, W.; Doyle, H.; Betley, T. A.; Kagan, C. R., Colloidal Synthesis of Nanocrystals and Nanocrystal Superlattices. *IBM J. Res. Dev.* **2001,** *45* (1), 47-56.

13.   Eustis, S.; El-Sayed, M. A., Why Gold Nanoparticles are More Precious than Pretty Gold: Noble Metal Surface Plasmon Resonance and its Enhancement of the Radiative and Nonradiative Properties of Nanocrystals of Different Shapes. *Chem. Soc. Rev.* **2006,** *35* (3), 209-217.

14.   Rosi, N. L.; Mirkin, C. A., Nanostructures in Biodiagnostics. *Chem. Rev.* **2005,** *105* (4), 1547-1562.

15.   Leslie-Pelecky, D. L.; Rieke, R. D., Magnetic Properties of Nanostructured Materials. *Chem. Mater.* **1996,** *8* (8), 1770-1783.

16.   Spaldin, N., Magnetic Materials, Fundamentals and Device Applications: Cambridge. *Cambridge* **2003**.

17.   Lübbe, A. S.; Alexiou, C.; Bergemann, C., Clinical Applications of Magnetic Drug Targeting. *J. Surg. Res.* **2001,** *95* (2), 200-206.

18.   Dobson, J., Magnetic Nanoparticles for Drug Delivery. *Drug Develop. Res.* **2006,** *67* (1), 55-60.

19.   Tegus, O.; Brück, E.; Buschow, K. H. J.; de Boer, F. R., Transition-Metal-Based Magnetic Refrigerants for Room-Temperature Applications. *Nature* **2002,** *415*, 150-152.

20.   Reiss, G.; Hutten, A., Magnetic Nanoparticles: Applications Beyond Data Storage. *Nat. Mater.* **2005,** *4* (10), 725-726.

21.   Murray, C. B.; Kagan, C. R.; Bawendi, M. G., Synthesis and Characterization of Monoodisperse Nanocrystals and Close-Packed Nanocrystal Assemblies. *Annu. Rev. Mater. Sci.* **2000,** *30* (1), 545-610.

22.   Gregg, K. A.; Perera, S. C.; Lawes, G.; Shinozaki, S.; Brock, S. L., Controlled Synthesis of MnP Nanorods: Effect of Shape Anisotropy on Magnetization. *Chem. Mater.* **2006,** *18* (4), 879-886.

23.   Murray, C. B.; Norris, D. J.; Bawendi, M. G., Synthesis and Characterization of Nearly Monodisperse CdE (E = Sulfur, Selenium, Tellurium) Semiconductor Nanocrystallites. *J. Am. Chem. Soc.* **1993,** *115* (19), 8706-8715.

24.   Park, J.; Kang, E.; Son, S.; Park, H.; Lee, M.; Kim, J.; Kim, K.; Noh, H. J.; Park, J. H.; Bae, C.; Park, J. G.; Hyeon, T., Monodisperse Nanoparticles of Ni and NiO: Synthesis, Characterization, Self-Assembled Superlattices, and Catalytic Applications in the Suzuki Coupling Reaction. *Adv. Mater.* **2005,** *17* (4), 429-434.

25.   LaMer, V. K.; Dinegar, R. H., Theory, Production and Mechanism of Formation of Monodispersed Hydrosols. *J. Am. Chem. Soc.* **1950,** *72* (11), 4847-4854.

26.   Klimov, V. I., Semiconductor and Metal Nanocrystals - Synthesis and Electronic and Optical Properties. *Marcel Dekker, Inc*. **2004**.

27.   Hyeon, T., Chemical Synthesis of Magnetic Nanoparticles. *Chem. Commun.* **2003,** (8), 927-934.

28.   Jiles, D., Introduction to Magnetism and Magnetic Materials. *Chapman and Hall: London* **1998,** *2nd Edition.*

29.   Sun, S.; Murray, C. B., Synthesis of Monodisperse Cobalt Nanocrystals and Their Assembly Into Magnetic Superlattices (Invited). *J. Appl. Phys.* **1999,** *85* (8), 4325-4330.

30.   Hullinger, F., Crystal Chemistry of the Chalcogenides and Pnictides of the Transition Metals. *Struct. Bond.* **1968,** *4*, 83-229.

31.   Oyama, S., Ted, Novel Catalysts for Advanced Hydroprocessing: Transition Metal Phosphides. *J. Catal.* **2003,** *216*, 343-352.

32.   Yang, J. B.; Kamaraju, K.; Yelon, W. B.; James, W. J.; Cai, Q.; Bollero, A., Magnetic Properties of the MnBi Intermetallic Compound. *Appl. Phys. Lett.* **2001,** *79* (12), 1846-1848.

33.   Sweeney, C. M.; Stamm, K. L.; Brock, S. L., On the Feasibility of Phosphide Generation From Phosphate Reduction: The Case of Rh, Ir, and Ag. *J. Alloys Compd.* **2008,** *448* (1-2), 122-127.

34.   Senevirathne, K.; Tackett, R.; Kharel, P. R.; Lawes, G.; Somaskandan, K.; Brock, S. L., Discrete, Dispersible MnAs Nanocrystals from Solution Methods: Phase Control on the Nanoscale and Magnetic Consequences. *ACS Nano* **2009,** *3* (5), 1129-1138.

35.   Li, J.; Ni, Y.; Liao, K.; Hong, J., Hydrothermal Synthesis of $Ni_{12}P_5$ Hollow Microspheres, Characterization and Photocatalytic Degradation Property. *J. Colloid Interface Sci.* **2009,** *332* (1), 231-236.

36.   Wang, X.; Clark, P.; Oyama, S. T., Synthesis, Characterization, and Hydrotreating Activity of Several Iron Group Transition Metal Phosphides. *J. Catal.* **2002,** *208* (2), 321-331.

37.   Oyama, S., Ted; Gott, T.; Zhao, H.; Lee, Y.-K., Transition Metal Phosphide

Hydroprocessing Catalysts: A Review. *Catal. Today* **2009,** *143*, 94-107.

38.   Yunle, G.; Fan, G.; Yitai, Q.; Huagui, Z.; Ziping, Y., A Solvothermal Synthesis of

Ultra-Fine Iron Phosphide. *Mater. Res. Bull.* **2002,** *37* (6), 1101-1105.

39.   Xie, Y.; Su, H. L.; Qian, X. F.; Liu, X. M.; Qian, Y. T., A Mild One-Step

Solvothermal Route to Metal Phosphides (Metal=Co, Ni, Cu). *J. Solid State Chem.* **2000,**

149 (1), 88-91.

40.   Qian, X. F.; Xie, Y.; Qian, Y. T.; Zhang, X. M.; Wang, W. Z.; Yang, L., Organo-

Thermal Preparation of Nanocrystalline Cobalt Phosphides. *Mater. Sci. Eng. B* **1997,** *49*

(2), 135-137.

41.   Wang, C.; Qian, X. F.; Zhang, X. M.; Li, Y. D.; Xie, Y.; Qian, Y. T., A New

Chemical Route to Prepare Nanocrystalline Cobalt Monoarsenide. *Mater. Res. Bull.*

1999, *34* (7), 1129-1133.

42.   Zhang, X. M.; Wang, C.; Qian, X. F.; Xie, Y.; Qian, Y. T., Synthesis of

Nanocrystalline Iron Monoarsenide via a Reductive Recombination Pathway. *J. Solid

State Chem.* **1999,** *144* (2), 237-239.

43.   Xie, Y.; Lu, J.; Yan, P.; Jiang, X.; Qian, Y., Solvothermal Coordination-

Reduction Route to [gamma]-NiSb Nanocrystals at Low Temperature. *J. Solid State

Chem.* **2000,** *155* (1), 42-45.

44.   Lukehart, C. M.; Milne, S. B.; Stock, S. R., Formation of Crystalline Nanoclusters

of Fe_2P, RuP, Co_2P, Rh_2P, Ni_2P, Pd_5P_2, or PtP_2 in a Silica Xerogel Matrix from Single-

Source Molecular Precursors. *Chem. Mater.* **1998,** *10* (3), 903-908.

45.   Burnam, K. J.; Carpenter, J. P.; Lukehart, C. M.; Milne, S. B.; Stock, S. R.; Jones, B. D.; Glosser, R.; Wittig, J. E., Nanocomposites Containing Nanoclusters of Ag, Cu, Pt, Os, Co_3C, Fe_2P, Ni_2P, Ge, or Pt/Sn. *Nanostruct. Mater.* **1995,** *5* (2), 155-169.

46.   Perera, S. C.; Fodor, P. S.; Tsoi, G. M.; Wenger, L. E.; Brock, S. L., Application of De-silylation Strategies to the Preparation of Transition Metal Pnictide Nanocrystals: The Case of FeP. *Chem. Mater.* **2003,** *15* (21), 4034-4038.

47.   Perera, S. C.; Tsoi, G.; Wenger, L. E.; Brock, S. L., Synthesis of MnP Nanocrystals by Treatment of Metal Carbonyl Complexes with Phosphines: A New, Versatile Route to Nanoscale Transition Metal Phosphides. *J. Am. Chem. Soc.* **2003,** *125* (46), 13960-13961.

48.   Park, J.; Koo, B.; Hwang, Y.; Bae, C.; An, K.; Park, J. G.; Park, H. M.; Hyeon, T., Novel Synthesis of Magnetic Fe_2P Nanorods from Thermal Decomposition of Continuously Delivered Precursors using a Syringe Pump. *Angew. Chem.* **2004,** *116* (17), 2332-2335.

49.   Fujii, H.; Uwatoko, Y.; Motoya, K.; Ito, Y.; Okamoto, T., Neutron Scattering Investigation of Itinerant Electron System Fe_2P. *J. Phys. Soc. Jpn.* **1988,** *57* (6), 2143-2153.

50.   Park, J.; Koo, B.; Yoon, K., Y; Hwang, Y.; Kang, M.; Park, J.-G.; Hyeon, T., Generalized Synthesis of Metal Phosphide Nanorods via Thermal Decomposition of Continuously Delivered Metal-Phosphine Complexes Using a Syringe Pump. *J. Am. Chem. Soc.* **2005,** *127* (23), 8433-8440.

51.   Wang, J.; Johnston-Peck, A., C; Tracy, J., B, Nickel Phosphide Nanoparticles with Hollow, Solid, and Amorphous Structures. *Chem. Mater.* **2009,** *21*, 4462-4467.

52.	Qian, C.; Kim, F.; Ma, L.; Tsui, F.; Yang, P.; Liu, J., Solution-Phase Synthesis of Single-Crystalline Iron Phosphide Nanorods/Nanowires. *J. Am. Chem. Soc.* **2004,** *126*, 1195-1198.

53.	Henkes, A. E.; Schaak, R. E., Trioctylphosphine: A General Phosphorus Source for the Low-Temperature Conversion of Metals into Metal Phosphides. *Chem. Mater.* **2007,** *19* (17), 4234-4232.

54.	Henkes, A. E.; Vasquez, Y.; Schaak, R. E., Converting Metals into Phosphides: A General Strategy for the Synthesis of Metal Phosphide Nanocrystals. *J. Am. Chem. Soc.* **2007,** *129*, 1896-1897.

55.	Chiang, R.-K.; Chiang, R.-T., Formation of Hollow Ni_2P Nanoparticles Based on the Nanoscale Kirkendall Effect. *Inorg. Chem.* **2007,** *46* (2), 369-371.

56.	Yin, Y.; Rioux, R. M.; Erdonmez, C. K.; Hughes, S.; Somorjai, G. A.; Alivisatos, A. P., Formation of Hollow Nanocrystals Through the Nanoscale Kirkendall Effect. *Science* **2004,** *304* (5671), 711-714.

57.	Zheng, X.; Yuan, S.; Tian, Z.; Yin, S.; He, J.; Liu, K.; Liu, L., One-pot Synthesis of Hollow Nickel Phosphdie Nanoparticles with Tunable Void Sizes Using Triphenylphosphine. *Mater. Lett.* **2009,** *63*, 2283-2285.

58.	Senevirathne, K.; Burns, A. W.; Bussel, M. E.; Brock, S. L., Synthesis and Characterization of Discrete Nickel Phosphide Nanoparticles: Effect of Surface Ligation Chemistry on Catalytic Hydrodesulfurization of Thiophene. *Adv. Funct. Mater.* **2007,** *17*, 3933-3939.

59.	Maneeprakorn, W.; Nguyen, C. Q.; Malik, M. A.; O'Brien, P.; Raftery, J., Synthesis of the Nickel Selenophosphinates $[Ni(Se_2PR_2)_2]$ (R = Pr, Bu and Ph) and Their

Use as Single Source Precursors for the Deposition of Nickel Phosphide or Nickel Selenide Nanoparticles. *Dalton Trans.* **2009,** (12), 2103-2108.

60.   Sawhill, S. J.; Phillips, D. C.; Bussell, M. E., Thiophene Hydrodesulfurization Over Supported Nickel Phosphide Catalysts. *J. Catal.* **2003,** *215* (2), 208-219.

61.   Sawhill, S. J.; Layman, K. A.; Van Wyk, D. R.; Engelhard, M. H.; Wang, C.; Bussell, M. E., Thiophene Hydrodesulfurization Over Nickel Phosphide Catalysts: Effect of the Precursor Composition and Support. *J. Catal.* **2005,** *231* (2), 300-313.

62.   Yang, S.; Prins, R., New Synthesis Method for Nickel Phosphide Hydrotreating Catalysts. *Chem. Commun.* **2005,** (33), 4178-4180.

63.   Panneerselvam, A.; Malik, M., A; Afzaal, M.; O'Brien, P.; Helliwell, M., The Chemical Vapor Deposition of Nickel Phosphide or Selenide Thin Films from a Single Precursor. *J. Am. Chem. Soc.* **2008,** *130*, 2420-2421.

64.   Liu, S.; Liu, X.; Xu, L.; Qian, Y.; Ma, X., Controlled Synthesis and Characterization of Nickel Phosphide Nanocrystal. *J. Cryst. Growth* **2007,** *304* (2), 430-434.

65.   Hu, X.; Yu, J. C., High-Yield Synthesis of Nickel and Nickel Phosphide Nanowires via Microwave-Assisted Processes *Chem. Mater.* **2008,** *20*, 6743-6749.

66.   Luo, F.; Su, H.-L.; Song, W.; Wang, Z.-M.; Yan, Z.-G.; Yan, C.-H., Magnetic and Magnetotransport Properties of Fe_2P Nanocrystallites via a Solvothermal Route. *J. Mater. Chem* **2004,** *14*, 111-115.

67.   Kelly, A. T.; Rusakova, I.; Ould-Ely, T.; Hofmann, C.; Luttge, A.; Whitmire, K. H., Iron Phosphide Nanostructures Produced from a Single-Source Organometallic

Precursor: Nanorods, Bundles, Crosses, and Spherulites. *Nano Lett.* **2007,** *7* (9), 2920-2925.

68.   Stamm, K. L.; Garno, J. C.; Liu, G.-y.; Brock, S. L., A General Methodology for the Synthesis of Transition Metal Pnictide Nanoparticles from Pnictate Precursors and Its Application to Iron−Phosphorus Phases. *J. Am. Chem. Soc.* **2003,** *125* (14), 4038-4039.

69.   Sweet, J. D.; Casadonte Jr, D. J., Sonochemical Synthesis of Iron Phosphide. *Ultrason. Sonochem.* **2001,** *8* (2), 97-101.

70.   Boda, G.; et al., Magnetic and Electric Properties of FeP_2 Single Crystals. *Phys. Scr.* **1971,** *4* (3), 132.

71.   Feichter, S.; Tributsch, H.; Evain, M.; Brec, R., γ-FeP_4, A New Photosensitive Semiconductor *Mater. Res. Bull.* **1987,** *22* (4), 543-549.

72.   Chen, J.-H.; Tai, M.-F.; Chi, K.-M., Catalytic Synthesis, Characterization and Magnetic Properties of Iron Phosphide Nanowires. *J. Mater. Chem.* **2004,** *14*, 296-298.

73.   Greenwood, N. N.; Earnshaw, A., Chemistry of Elements. **1997,** *2nd Edition*, 489-492.

74.   Cullity, B. D., Elements of X-Ray Diffraction. *Addison-Wesley Publishing Company, Inc.* **1956**, Chapter 14.

75.   West, A. R., Basic Solid State Chemistry. **August 2000,** *2nd Edition*.

76.   Evans, J. S. O.; Evans, I. R., Beyond Classical Applications of Powder Diffraction. *Chemical Society Reviews* **2004,** *33* (8), 539-547.

77.   Williams, D. B.; Carter, C. B., Transmission Electron Microscopy. *Springer* **2010,** *2nd Volume*.

78.   Fultz, B.; Howe, J., Transmission Electron Microscopy and Diffractometry of Materials. *Springer* **2000**.

79.   Gregg, S. J.; Sing, K. S. W., Adsorption, Surface Area and Porosity. *Academic Press* **1982,** *2nd Edition*.

80.   Webb, P. A.; Orr, C., Analytical Methods in Fine Particle Technology. *Micromeritics Instrument Corporation* **1997**.

81.   Kleiner, R.; Koelle, D.; Ludwig, F.; Clarke, J., Superconducting Quantum Interference Devices: State of the Art and Applications. *Proceedings of the IEEE* **2004,** *92* (10), 1534-1548.

82.   Clarke, J.; Braginski, A. I., The SQUID Handbook Vol. I Fundamentals and Technology of SQUIDs and SQUID systems. *Wiley VCH* **2004**.

83.   Blanchard, P. E. R.; Grosvenor, A. P.; Cavell, R. G.; Mar, A., X-ray Photoelectron and Absorption Spectroscopy of Metal-Rich Phosphides M_2P and M_3P (M = Cr−Ni). *Chem. Mater.* **2008,** *20* (22), 7081-7088.

84.   Grosvenor, A. P.; Cavell, R. G.; Mar, A., Bonding and Electronic Structure of Phosphides, Arsenides and Antimonides by X-ray Photoelectron Spectroscopy. In Structure and Bonding. *Springer: Berlin* **2009**.

85.   Peng, S.; Wang, C.; Xie, J.; Sun, S., Synthesis and Stabilization of Monodisperse Fe Nanoparticles. *J. Am. Chem. Soc.* **2006,** *128*, 10676-10677.

86.   Muthuswamy, E.; Kharel, P. R.; Lawes, G.; Brock, S. L., Control of Phase in Phosphide Nanoparticles Produced by Metal Nanoparticle Transformation: Fe_2P and FeP. *ACS Nano* **2009,** *3* (8), 2383-2393.

87.   Shao, H.; Lee, H.; Huang, Y.; Ko, I.; Kim, C., Control of Iron Nanoparticles Size and Shape by Thermal Decomposition Method. *IEEE Trans. Magn.* **2005,** *41* (10), 3388-3390.

88.   Mukherjee, S.; Rayachaudhuri, P.; Nigam, A. K., Critical Behavior in $La_{0.5}Sr_{0.5}CoO_3$ *Phys. Rev. B* **2000,** *61*, 8651-8653.

89.   Aitken, J. A.; Tsoi, G. M.; Wenger, L. E.; Brock, S. L., Phase Segregation of MnP in Chalcopyrite Dilute Magnetic Semiconductors: A Cautionary Tale. *Chem. Mater.* **2007,** *19*, 5272-5278.

90.   Felcher, G., P; Smith, F., A, Magnetic Structure of Iron Monophosphide. *Phys. Rev. B* **1971,** *3*, 3046-3052.

91.   Ni, Y.; Tao, A.; Hu, G.; Cao, X.; Wei, X.; Yang, Z., Synthesis, Characterization and Properties of Hollow Nickel Phosphide Nanospheres. *Nanotechnology* **2006,** *17*, 5013-5018.

92.   Railsback, J. G.; Johnston-Peck, A. C.; Wang, J.; Tracy, J. B., Size-Dependent Nanoscale Kirkendall Effect During the Oxidation of Nickel Nanoparticles. *ACS Nano* **2010,** *4* (4), 1913-1920.

93.   Carenco, S.; Boissere, C.; Nicole, L.; Sanchez, C.; Le Floch, P.; Mezailles, N., Controlled Design of Size-Tunable Monodisperse Nickel Nanoparticles. *Chem. Mater.* **2010,** *22*, 1340-1349.

94.   Slowing, I.; Trewyn, B.; Giri, S.; Lin, V. Y., Mesoporous Silica Nanoparticles for Drug Delivery and Biosensing Applications. *Adv. Funct. Mater.* **2007,** *17* (8), 1225-1236.

95.   Huh, S.; Wiench, J. W.; Yoo, J.-C.; Pruski, M.; Lin, V. S. Y., Organic Functionalization and Morphology Control of Mesoporous Silicas via a Co-Condensation Synthesis Method. *Chem. Mater.* **2003,** *15* (22), 4247-4256.

96.   Kim, H.; Chae, Y.; Lee, D.; Kim, M.; Huh, J.; Kim, Y.; Kim, S.; Baik, H.; Choi, K.; Kim, J.; Yi, G. R.; Lee, K., Palladium Nanoparticle Catalyzed Conversion of Iron Nanoparticles into Diameter- and Length-Controlled Fe_2P Nanorods. *Angew. Chem. Int. Ed.* **2010,** *49* (33), 5712-5716.

97.   Wang, A.; Qin, M.; Guan, J.; Wang, L.; Guo, H.; Li, X.; Wang, Y.; Prins, R.; Hu, Y., The Synthesis of Metal Phosphides: Reduction of Oxide Precursors in a Hydrogen Plasma. *Angew. Chem. Int. Ed.* **2008,** *47* (32), 6052-6054.

98.   Wu, L.-M.; Sharma, R.; Seo, D.-K., Metathetical Conversion of Nd_2O_3 Nanoparticles into NdS_2 Polysulfide Nanoparticles at Low Temperatures Using Boron Sulfides. *Inorg. Chem.* **2003,** *42* (19), 5798-5800.

99.   Muthuswamy, E.; Brock, S. L., Oxidation Does Not (Always) Kill Reactivity of Transition Metals: Solution-Phase Conversion of Nanoscale Transition Metal Oxides to Phosphides and Sulfides. *J. Am. Chem. Soc.* **2010,** *132* (45), 15849.

100.   Chen, Y.; She, H.; Luo, X.; Yue, G.-H.; Peng, D.-L., Solution-Phase Synthesis of Nickel Phosphide Single-Crystalline Nanowires. *J. Cryst. Growth* **2009,** *311* (4), 1229-1233.

101.   Gopalakrishnan, J.; Pandey, S.; Rangan, K. K., Convenient Route for the Synthesis of Transition-Metal Pnictides by Direct Reduction of Phosphate, Arsenate, and Antimonate Precursors†. *Chem. Mater.* **1997,** *9* (10), 2113-2116.

102. Lieber, C. M., One-Dimensional Nanostructures: Chemistry, Physics & Applications. *Solid State Commun.* **1998,** *107* (11), 607-616.

103. Puntes, V. F.; Krishnan, K. M.; Alivisatos, A. P., Colloidal Nanocrystal Shape and Size Control: The Case of Cobalt. *Science* **2001,** *291* (5511), 2115-2117.

104. Balli, M.; Fruchart, D.; Gignoux, D.; Tobola, J.; Hlil, E. K.; Wolfers, P.; Zach, R., Magnetocaloric Effect in Ternary Metal Phosphides $(Fe_{1-x}Ni_x)_2$P. *J. Magn. Magn. Mater.* **2007,** *316* (2), 358-360.

ABSTRACT

SYNTHETIC LEVERS ENABLING CONTROL OF PHASE, SIZE AND MORPHOLOGY IN TRANSITION METAL PHOSPHIDE NANOPARTICLES (FE, NI)

by

ELAYARAJA MUTHUSWAMY

May 2011

Advisor: Dr. Stephanie L. Brock

Major: Chemistry

Degree: Doctor of Philosophy

This dissertation study focuses on (1) development of a synthetic strategy to control phase in nanoscale iron phosphides; (2) extension of the developed phase control strategy to the nanoscale nickel phosphide system with simultaneous control on size and morphology and (3) illustration of the enhanced reactivity of nanoscale oxide systems.

A synthetic strategy to control phase in nanoscale iron phosphides was developed to prepare phase-pure samples of Fe_2P and FeP. The metal nanoparticle conversion strategy first reported by Schaak and coworkers was selected as a starting point to carry out a detailed study on the effect of various synthetic levers on the phase of the final product. Spherical Fe nanoparticles were prepared by the decomposition of $Fe(CO)_5$ and were subsequently treated with tri-octylphosphine (TOP) at temperatures in the range 350-385 °C to convert the Fe nanoparticles into iron phosphide nanoparticles. Optimized conditions for Fe_2P and FeP were arrived at by evaluating temperature, heating time,

order of addition of reagents and quantity of 'Fe' and 'P' precursors. The intrinsic magnetic properties of the nanoscale phosphides were determined by magnetic susceptibility measurements and attest to the purity of the samples.

The phase control strategy was successfully extended to the nickel phosphide system, resulting in the preparation of phase-pure samples of $Ni_{12}P_5$ and Ni_2P. In addition, a handle on the size and morphology of both $Ni_{12}P_5$ and Ni_2P was achieved by evaluating them as a function of precursor ratios and quantity of oleylamine. Thus, the ability to selectively prepare either $Ni_{12}P_5$ or Ni_2P in a range of sizes from a few nanometers to 10's of nanometers, and as either hollow or dense spheres, was achieved. In addition, transformations of metal-rich phosphides ($Ni_{12}P_5$) to more P-rich phosphides (Ni_2P) were carried out with retention of morphology (hollow and dense) of the starting product, indicating that topotactic transformations are possible in these systems.

The enhanced reactivity of oxide nanoparticle systems in their transformation to phosphides and sulfides was demonstrated by reactions with TOP and elemental sulfur, respectively. Oxide nanoparticles (NiO, Fe_3O_4, CoO and Mn_3O_4) were prepared by the oxidation of salts in a high boiling solvent/surfactant system under a slow and steady air flow. The completely oxidized nanoparticles (<10 nm) were treated with TOP at elevated temperatures (≥ 350 °C) under inert conditions to convert them to phosphide phases. Successful transformation was achieved for NiO, Fe_3O_4 and CoO nanoparticles, generating phase-pure Ni_2P, FeP and CoP, respectively. Intriguingly, the method does not work for Mn_3O_4 nanoparticles, or bulk oxides (size ≥ 50 nm). Transformation of all oxide nanoparticles (including Mn_3O_4) into their corresponding sulfide phases is also demonstrated.

AUTOBIOGRAPHICAL STATEMENT

ELAYARAJA MUTHUSWAMY

Education
- **2005-2010 Ph.D** Inorganic Chemistry, Wayne State University, Detroit, MI
  Dissertation: Synthetic Levers Enabling Control of Phase, Size and Morphology in Transition Metal Phosphides (Fe, Ni);
  Advisor: Prof. Stephanie L. Brock
- **2002-2004 M.Sc** Applied Chemistry, Coimbatore Institute of Technology, Anna University, INDIA.
- **1998-2001 B.Sc** Chemistry, St. Joseph's College, Bharathidasan University, INDIA.

Research and Training Experience
- **08/2005 – 08/2007** Graduate Teaching Assistant, Dept. of Chemistry, Wayne State University, Detroit, MI
- **08/2007 – 11/2010** Graduate Research Assistant, Dept. of Chemistry, Wayne State University, Detroit, MI

Technical Skills
- Glove box and Schlenk line techniques, Powder X-ray Diffraction, Transmission Electron Microscopy, Energy Dispersive Spectroscopy, Thermo Gravimetric Analysis, UV-Visible and Infra-Red Spectroscopy, Dynamic Light Scattering, Porosimetry Analysis.

Affiliations, Awards and Fellowships
- Member – American Chemical Society
- Summer Dissertation Fellowship – 2009
- Best Poster – WSU Chemistry Graduate Symposium – 2008

Publications
Muthuswamy, E.; Ramadevi, S.; Vasan, H. N.; Garcia, C.; Noe, L.; Verelst, M., *J. Nanopart. Res*. **2007,** 9 (4), 561 -567.

Muthuswamy, E.; Kharel, P. R.; Lawes, G.; Brock, S. L., *ACS Nano,* **2009,** *3* (8), 2383-2393.

Muthuswamy, E.; Brock, S. L., *J.Am.Chem.Soc.,* **2010,** 132, 15849-15852.

Bhattarai, S.; Muthuswamy, E.; Wani, A.; Brichacek, M.; Castañeda, A.; Brock, S.; Oupicky, D., *Pharm. Res.,* **2010**. Published online on August 21 2010. *DOI: 10.1007/S11095-010-0245-0*

Muthuswamy, E.; Savithra, L. G. H.; Brock, S. L., Synthetic Levers Enabling Independent Control of Phase, Size, and Morphology in Nanoscale Nickel Phosphides. *Manuscript in preparation.*

Muthuswamy, E.; Brock, S. L., Solid-State Phase Transformations in Solution: Directing Morphology and Phase in Nickel Phosphides. *Manuscript in preparation.*